Neutron Scattering Studies on Layered Ruthenates

Max-Planck-Institut für Festkörperforschung
Universität Stuttgart

Vorgelegt von:
Maximilian Josef Krautloher
aus Heidelberg, Deutschland

Hauptberichter:	Prof. Dr. Bernhard Keimer
Mitberichter:	Prof. Dr. Maria Daghofer
Prüfungsvorsitzender:	Prof. Dr. Peter Michler

Tag der mündlichen Prüfung: 18. Dezember 2018

Von der Fakultät Mathematik und Physik der Universität Stuttgart zur Erlangung der Würde eines Doktors der Naturwissenschaften (Dr. rer. nat.) genehmigte Abhandlung

Stuttgart, 2018

Contents

Acronyms

AFM antiferromagnetic

ALBA ALBA synchrotron light source, Barcelona, Spain

ARCS [**1, 2**] Wide angular-range chopper spectrometer, located at SNS

BOREAS [**3, 4**] Resonant X-ray absorption and scattering spectrometer, located at the ALBA

CF crystal field

E6 [**5**] Focusing Powder Diffractometer [5], located at HZB

EIGER [**6, 7**] Thermal neutron triple-axis-spectrometer, located at the PSI

FM ferromagnetic

HZB Helmholtz Zentrum Berlin, Germany

ILL Institute Laue-Langevin, Grenoble, France

IN20 [**8, 9**] Thermal neutron three-axis spectrometer with polarization analysis, located at ILL

IN8 [**10, 11**] Thermal neutron three-axis spectrometer [10, 11] with the option to perform experiments with a single detector or the Flatcone multidetector [12], located at ILL

INS inelastic neutron scattering

ISIS Rutherford Appleton Laboratories, ISIS, STFC

MERLIN [**13, 14**] high count rate, medium energy resolution, direct geometry chopper spectrometer, located at ISIS

MIT metal-to-insulator transition

MLZ Meier-Leibniz Zentrum, Garching, Germany

OFZ optical floating zone

PSI Paul-Scherrer-Instiut, Villigen, Switzerland

PUMA [**15, 16**] Thermal three axes spectrometer, located at MLZ

RP Ruddlesden-Popper

SC superconductivity

SNS Spallation Neutron Source

SOC spin-orbit coupling

SPODI [**17, 18**] High resolution neutron powder diffractometer, located at MLZ

TM transition metal

TMO transition metal oxide

Neutronenspektroskopische Untersuchungen an Ruthenat-Schichtsystemen

Oxide von Übergangsmetallen weisen eine Vielzahl magnetischer, elektronischer und struktureller Phasen auf und sind zentraler Forschungsgegenstand der Festkörperphysik. Der enge Wettbewerb zwischen verschiedenen Wechselwirkungen und Ordnungsphänomenen, die für solche Systeme typisch sind, führt zu Phasendiagrammen, die durch eine Vielzahl von Übergängen gekennzeichnet sind. Diese hängen häufig von externen Konditionen ab, wie etwa von der Temperatur, angelegte magnetische oder elektrische Felder, Druck und chemische Dotierung. Frühe Forschungsarbeiten konzentrierten sich auf Oxide von Übergangsmetallen mit flachen elektronischen Bändern und stark korrelierten Elektronensystemen. Prominente Beispiele sind die Familien von Kupferoxiden, die *Hochtemperatursupraleitung* zeigen, und Manganite, die *kolossalen Magnetwiderstand* zeigen. Lange Zeit wurde nicht erwartet, dass Oxide schwerer Übergangsmetalle besonders interessante Phänomene zeigen: Mit zunehmender Atommasse nehmen die ionischen Radien zu und die Coulomb-Abstoßung ab. Dadurch nimmt auch die Ausdehnung der d Orbitale zu, was zu gößerem Überlapp der Orbitale führt und die elektronische Bandbreite $\mathfrak{W}$ zunehmen lässt. Es wurde daher erwartet, dass Oxide, die auf schweren Übergangsmetallen basieren, metallisch sind und nicht den komplizierten Wettbewerb zwischen verschiedenen Ordnungsphänomenen zeigen, wie er in Oxiden von leichten Übergangmetallen zu finden ist. Vor kurzem wurde jedoch erkannt,

dass die Spin-Bahn Kopplung das Phasenverhalten von $4d$ und $5d$ Elektronen-Materialien grundlegend verändern kann. Die Stärke von der Spin-Bahn Kopplung skaliert mit der Ordnungzahl Z in der vierten Potenz, was sie zu einer treibenden Kraft in Oxiden schwerer Übergangsmetalle macht. Da das Zusammenspiel zwischen Spin-Bahn Kopplung und elektronischen Korrelationen zu neuartigen Quantengrundzuständen führt, haben diese Systeme im letzten Jahrzehnt zunehmendes Interesse gefunden. Eines dieser Systeme ist Sr_2IrO_4, indem durch dieses Zusammenspiel ein isolierender Mott-Zustand mit dem Gesamtdrehimpuls $J_{\mathrm{eff}} = 1/2$ erzeugt wird. $4d$-Elektronverbindungen, die durch moderate Spin-Bahn Kopplung gekennzeichnet sind, wurden bis vor kurzem ähnlich wie Oxide von $3d$ Elektronensystemen modelliert indem die Spin-Bahn Kopplung nur als geringfügige Störung behandelt wurde. Da aber auch moderate Spin-Bahn Kopplung sich ausreichend erwiesen hat um exotische Phänomene zu realisieren, erfassen solchen Ansätze nicht alle Aspekte solcher Systeme. Daher wurde die Rolle der Spin-Bahn Kopplung in $4d$ Übergangsmetallen unterschätzt, was eine Neubewertung der zugrunde liegenden Physik erforderlich macht um die Vielzahl konkurrierender struktureller und magnetischer Phasen korrekt beschreiben zu können.

In dieser Arbeit konzentrieren wir uns auf den antiferromagnetischen Mott-Isolator Ca_2RuO_4, bei dem die Wechselwirkung auf die zweidimensionalen Schichten von RuO_6-Oktaedern beschränkt ist. Die low-Spin $4d^4$ Konfiguration von Ru^{4+} führt zu eine $S = 1$ Spinquantenzahl, während die Gittersymmetrie zu einem effektiven Bahnmoment von $L_{\mathrm{eff}} = 1$ führt. Frühere Studien haben gezeigt, dass Ca_2RuO_4 beim Erhitzen einen Metall-Isolator-Übergang durchläuft und bei isovalenter Substitution mit Sr eine Reihe von Phasenübergängen aufzeigt. Die große Vielfalt der Phasen macht Ca_2RuO_4 zu einem idealen Material, um die Rolle moderater Spin-Bahn Kopplung im Magnetismus zu untersuchen. Wir konzentrieren uns auf das magnetische Anregungsspektrum, das den kombinierten Einfluss der Austauschwechselwirkungen zwischen den Ru-Ionen und der intra-ionischen Spin-Bahn Kopplung widerspiegelt.

Der erste Teil dieses Promotionsprojekts widmet sich dem Wachstum hochwertiger Kristalle von Ca_2RuO_4 und verwandten Rutheniumoxiden. Zu diesem Zweck haben wir die optische

Fließzonentechnik verwendet. Um Untersuchungen mit Neutronenstreuung durchzuführen wurden mehrere hundert Kristallfragmente gegeneinander ausgerichtet und so die benötigte Masse für inelastische Messungen bereitgestellt. Durch unsere Experimente konnten wir das inelastische Streuspektrum innerhalb der ersten magnetischen Brillouin-Zone beobachten und alle transversalen Magnonmoden (*Goldstone*-Moden) sowie eine longitudinale Amplitudenmode (*Higgs*-Mode) identifizieren. Die Ergebnisse können in einem *exitonic magnetism* Modell konsistent interpretiert werden, das auf einem dominanten Einfluss der Spin-Bahn Kopplung basiert. In weiteren Untersuchungen griffen wir wieder auf inelastische Neutronenstreumethoden zurück, um die magnetischen Anregungen eines Sr-substituierten Ca_2RuO_4 Kristalls zu untersuchen, und konnten modifizierte Austauschwechselwirkungen feststellen. Wir haben auch das eng verwandte $Ca_3Ru_2O_7$ System untersucht. Hier werden Doppelschichten aus RuO_6-Oktaedern durch eine CaO Sperrschicht verschachtelt. Wir beobachten, dass dieses Doppelschichtsystem eine metallische Phase aufweist, in der der Einfluss der Spin-Bahn Wechselwirkung weniger ausgeprägt ist. Überraschenderweise führt eine chemische Substitution von 1% $4d^4$ Ru^{4+} Ionen mit magnetisch inaktiven $3d^0$ Ti^{4+} Ionen das System in einen isolierend Zustand über. In dieser Phase ähneln die magnetischen Anregungen des Systems denen von Ca_2RuO_4, was auf denselben *excitonic magnetism* schließen lässt.

Unsere Studien belegen die entscheidende Rolle der Spin-Bahn Kopplung für die magnetischen Eigenschaften von Rutheniumoxiden und fordern eine allgemeine Neubewertung der Auswirkungen von Spin-Bahn Wechselwirkungen auf den Grundzustand und die Anregungen von $4d$ Elektronensystemen.

Neutron Spectroscopic Studies on Layered Ruthenates

Transition metal oxides (TMOs) exhibit a large variety of magnetic, electronic, and structural phases and have received much attention from the community. The tight competition between different interactions and ordering phenomena typical for such systems result in phase diagrams which are characterized by a multitude of transitions. These often depend on external variables, including temperature, magnetic or electric fields, pressure, and chemical doping. Early research focused on oxides of light transition metals exhibiting flat electronic bands and strongly correlated systems. Prominent examples include the families of copper oxides (cuprates) that exhibit *high-temperature superconductivity*, and manganites that show *colossal magnetoresistance*. For a long time, oxides of heavier transition metals were not expected to exhibit particular exciting phenomena: with increasing atomic mass and ionic radii, the Coulomb repulsion decreases while the extension of the d orbitals enlarges, consequently increasing the orbital overlap and the electronic bandwidth $\mathfrak{W}$. Such heavy-metal based systems were therefore expected to be metallic, without the intricate competition between different ordering phenomena seen in their lighter analogues. Recently, however, it was recognized that the spin-orbit coupling (SOC) can profoundly change the phase behavior of 4d- and 5d-electron materials. The strength of SOC scales with the atomic number Z as $\propto Z^4$, which—in contrast to systems including 3d TMOs—renders SOC a driving force in

9

oxides of heavy transition metals. As the interplay between SOC and electronic correlations brings about novel quantum ground states, these systems have received increasing interest during the last decade. One such systems is Sr_2IrO_4, where this interplay generates a Mott-insulating state with total angular momentum $J_{eff} = {}^1/2$. $4d$-electron compounds, which are characterized by moderate SOC, have until recently been modeled akin to oxides of $3d$-electron systems, treating the SOC as a minor perturbation only. However, even moderate SOC proved to be enough to realize exotic phenomena that are not captured by such approaches, and can lead to a variety of competing structural and magnetic phases. Consequently, the role of SOC in $4d$ TMOs has been underestimated, calling for re-evaluation of the underlying physics.

In this work we focus on the antiferromagnetic Mott insulator Ca_2RuO_4, in which the interaction is limited to the two-dimensional layers of RuO_6 octahedra. The low-spin $4d^4$ configuration of Ru^{4+} leads to a $S = 1$ spin, while the lattice symmetry results in an effective orbital momentum of $L_{eff} = 1$. Previous studies have shown that Ca_2RuO_4 undergoes an insulator-metal transition upon heating and exhibits a series of phase transitions upon isovalent substitution with Sr. The wide variety of phases makes Ca_2RuO_4 a prime material platform to investigate the role of moderate SOC in magnetism. We concentrate on the magnetic excitation spectrum, which reflects the combined influence of the exchange interactions between the Ru ions and the inter-ionic SOC.

The first part of this PhD project is dedicated to the growth of high-quality crystals of Ca_2RuO_4 and related ruthenium oxides. To this end, we used the optical floating zone technique. The several hundred crystal shards were then co-aligned to be used in inelastic neutron scattering experiments. With a map of the magnetic scattering intensity in the full magnetic Brillouin zone, we observe and distinguish all transverse magnon (Goldstone) modes as well as a longitudinal amplitude (Higgs) mode. The results can be consistently interpreted in an *excitonic magnetism* model with a dominant influence of the SOC. We then used inelastic neutron scattering to investigate the magnetic excitations of the Sr-substituted Ca_2RuO_4 crystals and found a modified set

of exchange interactions. We also investigated the closely related $Ca_3Ru_2O_7$ system; here, a double-layers of RuO_6 octahedra are interleaved by a CaO barrier layer. We find that this bilayer system exhibits a metallic phase where the impact of the SOC is less pronounced. Surprisingly, a chemical substitution of the $4d^4$ Ru^{4+} ions with magnetically inactive $3d^0$ Ti^{4+} ions renders the system insulating even for Ti concentrations less than 1%. In this phase that the system's magnetic excitations are similar to Ca_2RuO_4 suggesting the same excitonic magnetism.

Our studies demonstrate the crucial role of SOC for the magnetic properties of ruthenium oxides, and call for a general re-evaluation of the impact of SOC on the ground state and excitations of $4d$-electron systems.

Chapter 1

Introduction

1.1 Transition metal oxides

TRANSITION METALS contain the elements of the d-block in the periodic table of elements. The behavior of the outer transition metals are characterized by their partially filled d-orbitals. The energetic competition of electronic, magnetic, or

Figure 1.1: Periodic table of the elements. The shaded block corresponds to the (outer) transition metals (d-block). Occasionally, the lanthanides and actinides of the f-block are referred to as inner transition metals.

structural phases arises from strong electron correlations alone or in interaction with spin-orbit coupling, and is the origin of a vast host of intriguing physical phenomena. It is these physical phenomena or their susceptibility to external forces that make these materials interesting for industrial applications. A short and non-exhaustive list of phases includes *Mott metal-insulator transitions* known from cuprates, vanadates [19, 20] or ruthenates [21, 22] depending on chemical substitution, temperature, and electric fields; *high-temperature superconductivity* that is observed in cuprates and iron pnictides and chalcogenides; *giant* or *colossal magneto resistance* effects that are relevant for data storage devices and are found in Fe/Cr superlattices [23] and manganites [24, 25], respectively; the *large thermopower* of rhodates and osmates; or quantum critical behavior [26].

The most prominent example is the class of copper oxides (cuprates) which is known for its unconventional *high-temperature superconductivity*, that arises upon electron or hole doping a Mott insulating antiferromagnetic groundstate. The parent com-
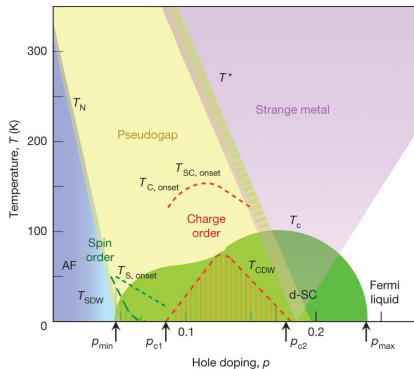
Figure 1.2: The phase diagram of the hole doped cuprates shows a wealth of phases. (figure adapted from [28])

pound showing this behavior—$La_{2-x}Ba_xCuO_4$—was discovered in 1986 [27] and set a record transition temperature T_c well above the limit expected for conventional superconductors. This sparked large research interest into this new class of materials as the pairing mechanism of the superconducting Cooper-pairs can not

be explained by phonon-electron interaction (Bardeen-Cooper-Schrieffer theory). The complex phase diagram of the cuprates shows several phases in the pseudogap above T_c [28] that may underlie or compete with the superconducting state. The microscopic origin leading to such a variety of phases is still being debated in the community.

In order to find different avenues to investigate unconventional superconductivity, many iso-structural systems have been investigated. The first copper-free system in which unconventional superconductivity was found is Sr_2RuO_4 [29], which has since received great interest. In figure 1.3 we compare its structure to
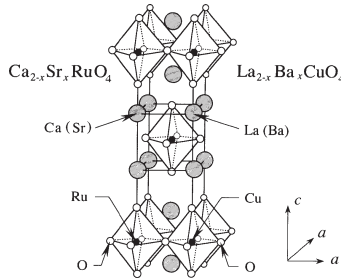
Figure 1.3: Structure of $Ca_{2-x}Sr_xRuO_4$ compared to $La_{2-x}Ba_xCuO_4$, the first high-T_c superconductor found by J. Bednorz and K. Müller [27] (Nobel prize, 1987). (figure adapted from [29], modified).

the cuprate parent compound. In both materials the correlations between the layers are weak, rendering the physics quasi two-dimensional. There are several differences to the cuprates: While the superconductivity of cuprates arises from a *bad metal* close to a Mott-insulating state, Sr_2RuO_4 is a metal with well defined fermionic quasiparticles; the pairing mechanism is necessarily different as the superconductive state has a different (triplet) symmetry for Sr_2RuO_4; the energy hierarchy may be different due to unquenched orbital momentum as spin-orbit coupling (SOC) is not negligible in the $4d^4$ ruthenium compound; furthermore, the critical temperature of Sr_2RuO_4 is very low $T_c = 1.5\,\mathrm{K}$. Thus, understanding the origin of superconductivity in Sr_2RuO_4 and comparing to the cuprate system may allow insights into the general requirements for superconductivity in layered transition

15

metal oxides (TMOs).

1.2 Energy scales in TMOs

In TMOs a number of different forces are at work, some of which scale with the atomic number Z or depend on the size of the involved transition metal (TM) ion. The electron correlations result from the Coulomb repulsion U and the hopping probability t of unpaired electrons. As the orbital size increases with the period of the element, U is reduced while t—depending on the orbital overlap—increases.

For oxides of light *TMs of the third period*, a basic description of the system is provided by the strong electron correlations within the framework of the *Mott-Hubbard* model [30]. It allows competition between the two energy scales and leads to various interesting scenarios. For a dominant on-site Coulomb repulsion $U \gg t$ the cost of transferring an electron to an already occupied site is too large to be overcome by its hopping probability t, which results in an insulating state where electrons are localized. Experimental realizations of such *Mott insulators* may cross over between the insulating state ($U > t$) and a conducting state ($U < t$) upon variation of the temperature, electric or magnetic fields, or other external perturbation. Such metal-to-insulator transitions (MITs) are often associated with magnetic order, which are captured by Heisenberg model that introduces an exchange energy $\mathfrak{J} = 2t^2/U$.

For oxides of *TMs of the fifth or sixth period* this model becomes inadequate as the energy hierarchies shift: SOC ζ becomes a major player as it rapidly increases with the atomic number $\zeta \propto Z^4$ (see comparison in figure 1.4). Thus, SOC can no longer be treated as a perturbation to the system. Instead, it is of the order of the crystal field generated by the oxygen ligands and can thus determine the energy levels of the system by coupling spin and unquenched orbital angular moments. A prominent example for such behavior is found in iridates with Ir^{4+} ions (such as Sr_2IrO_4) in which strong SOC couples spin and orbital moments to $J_{eff} = 1/2$, and $3/2$ levels. The $J_{eff} = L_{eff} + S = 1/2$ state is further split by Coulomb repulsion into a lower Hubbard band below
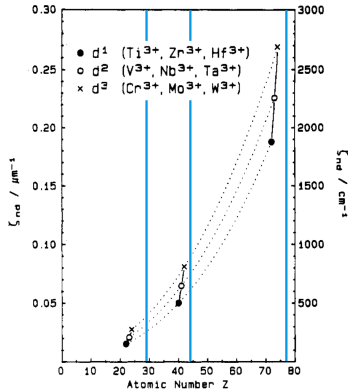
Figure 1.4: spin-orbit coupling parameters ζ_{nd} for gaseous TM ions. The blue highlights help to estimate and comparing the coupling strength of ^{29}Cu, ^{44}Ru, and ^{77}Ir. (figure taken from [31], highlights added)

and an empty upper Hubbard band above the Fermi energy and thus brings about a Mott insulating state [32], effectively induced by SOC.

Interestingly, theoretical models describing 4d *TMOs* traditionally have assumed a spin-only system where SOC acts as a (relatively strong) perturbation. Elliott and Thorpe make a point that systems in which orbital effects are present 'are not of the Heisenberg type' ([33]). Instead, they argue, a different scenario is more appropriate: While crystal fields are still the dominant energy scale, sufficiently strong SOC can couple spin and partially quenched orbital moments to an effective total angular momentum J_{eff}.

Experimental results for such 4d systems [34–36] indicate that the energy scales of *lattice distortions*, *exchange interaction*, and *SOC* are all of the same scale, which enables competition or cooperation between many forces. While this is a valid scenario, it has found only little consideration until the recent past. In light of the new ground states driven by SOC that have been found in the 5d-electron systems, its role in 4d-electron systems should be re-evaluated.
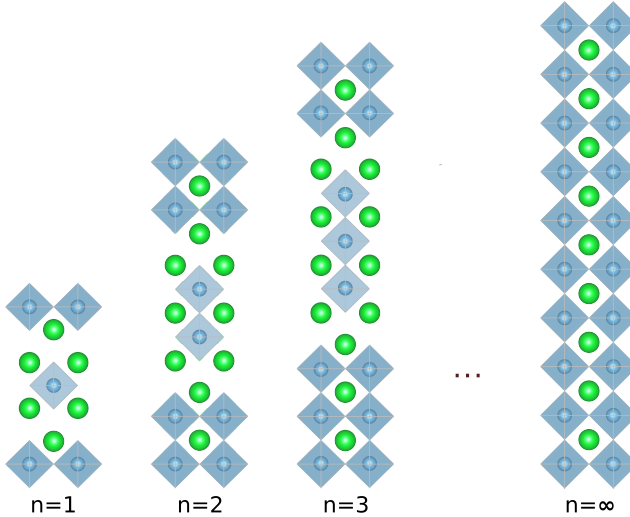
17

Layered transition metal oxides

Figure 1.5: Members of the Ruddlesden-Popper series with $n = 1$ (single layer), $n = 2$ (bilayer), $n = 3$ and $n = \infty$ (bulk) adjacent BO_6 planes. (structures based on crystallographic data for strontium titanite by [37–39])

Solid state research has a rich history in the investigation of layered materials, as they offer to investigate quasi two-dimensional correlation effects. In 1958 Ruddlesden and Popper reported on the compound $Sr_3Ru_2O_7$ and categorized its structure as an 'intermediate between those of Sr_2TiO_4 (K_2NiF_4 type) [...] and $SrTiO_3$ (perovskite).' ([37]) Generalized to compounds of the form $A_{n+1}B_nO_{3n+1}$[1], the class of Ruddlesden-Popper (RP) structures makes it possible to control the stacking size n. Here, n is number of adjacent sheets of corner (edge) sharing BO_6 octahedra that are interleaved by layers of AO in a rock salt formation (figure 2.1). Thus, the RP series provides a path to control out-of-plane interaction between neighboring B-sites, with the extremes being

---

[1]equivalent to the chemical formula $AO(ABO_3)_n$, which emphasizes the layered structures of the compounds.

Figure 1.6: Splitting of the d orbitals in a local cubic crystal field into t_{2g} and e_g levels by 10 Dq.

the quasi 2-dimensional A_2BO_4 ($n = 1$) and the 3-dimensional, bulk-like ABO_3 ($n = \infty$) configurations.

Optimized crystal growth processes allow the targeted synthesis of particular members of the RP series (usually $n =1$, 2 and 3 and the *bulk* ABO_3 phase). Implicitly, an increase in the number of adjacent layers goes hand in hand with a more 3D like behavior as out-of-plane bonds between layers foster coupling along the stacking directions. Thus, RP materials provide a possibility of tuning the dimensionality of their valence-electron systems.

Symmetry imposed by crystal fields

In TMs, the symmetry of the crystal field (CF) determines the level structure of the TM ions. The CF results mostly from the ions in the coordination sphere of the TM ions, a role that is usually played by a regular network of oxygen anions. The network's symmetry replaces the spherical symmetry of the central TM ion in free space and the associated five-fold degeneracy of the d-level orbitals (d_{xy}, d_{yz}, d_{zx}, $d_{x^2-y^2}$, and $d_{3r^2-z^2}$). Two prominent examples are tetrahedral BO_4 and cubic BO_6 configurations, generated by four or six oxygen ions regularly coordinated around the central TM B cation forming the corners of a tetrahedron or octahedron, respectively. In each configuration, orbitals oriented parallel the TM−O bonds are less favorable than those that do not co-align due to Coulomb interactions; in the case of cubic fields the d_{xy}, d_{yz}, and d_{zx} orbitals forming the t_{2g} sub-shell are preferred while the e_g sub-shell ($d_{x^2-y^2}$, and $d_{3r^2-z^2}$) are elevated in energy, as illustrated in figure 1.6. We note that the orbital angular momentum L is completely quenched in the e_g state, and partially quenched in the t_{2g} state ($L_{\text{eff}} = 1$) [40]. Thus, spin-orbit coupling SOC is only active in the t_{2g} state, which can

result in hybridization of these levels.

1.3 Ruthenate systems

The close structural relation between the parent compound $La_{2-x}Ba_xCuO_4$ of the cuprate superconductors and the odd-parity superconductor Sr_2RuO_4 sparked intense research into ruthenate systems. While details of the pairing mechanism in Sr_2RuO_4 are still debated, it has become clear that SOC plays a major role. The system is susceptible to external forces such as lattice distortions, chemical impurities, and magnetic fields. By substituting Sr with isovalent Ca, the system changes its characteristics profoundly: Upon continuous *chemical substitution* many intriguing phases are encountered and the phase diagram of $Ca_{2-x}Sr_xRuO_4$ (see figure 2.2) exhibits phases such as antiferromagnetic (AFM) insulating and metallic states, a broad domain of strong ferromagnetic (FM) fluctuations embedded in a metallic phase, and the triplet-superconductivity of Sr_2RuO_4.

While the importance of SOC in $4d$ electron systems is widely acknowledged, it is still often treated as a minor perturbation to a spin-only system. A particularly well suited phase to investigate the role of SOC in magnetism is the antiferromagnetic (AFM) insulating phase of Ca_2RuO_4, as the magnetic excitations encode the energy hierarchy of the system and can directly be investigated with neutron spectroscopic techniques. Until recently however, there were no reports of such inelastic neutron scattering studies [41, 42]. While several experiments report active and strong SOC in the system [43, 44], the literature reports divided opinions whether spin and orbital momentum states are coupled [42, 45] or if a spin-only Hamiltonian, that considers SOC a minor perturbation, is sufficient to describe the magnetic properties of the system [41, 46, 47].

Furthermore, by increasing the number of adjacent layers of RuO_6 octahedra sheets the *dimensionality* of the system can be influenced [49]. The different members are characterized by their coupling within their layers (in the a, b plane) as well as their inter-layer coupling (between adjacent layers), which crucially depends on the overlap of Ru $4d$ and O $2p$ orbitals and thus
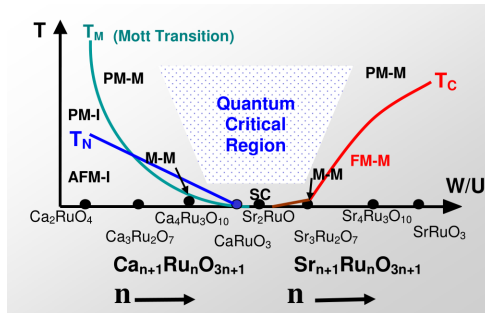
Figure 1.7: Magnetic phase diagram of the $(Ca_{1-x}Sr_x)_{n+1}Ru_nO_{3n+1}$ depending on the effective $U/\mathfrak{W}$ ratio. (figure adapted from [48].)

are directly influenced by lattice distortions. Changes to the interionic coupling strength will directly influence the magnetism of the system, so we can expect a change in the static and dynamic properties. From the magnetic properties of the different $(Sr,Ca)_{n+1}Ru_nO_{3n+1}$ systems Cao and Schlottmann have compiled a phase diagram grouping the single compounds by their $\mathfrak{W}/U$ ratio (where U is the on-site Coulomb repulsion and $\mathfrak{W}$ is the electronic bandwidth), reproduced in figure 1.7.

Another AFM Mott insulating [50] system is the $n = 2$ member or the $Ca_{n+1}Ru_nO_{3n+1}$ RP series, which shows a wealth of different magnetic phases, including *colossal magnetoresistance* [51], a *bulk spin-valve* behavior [52], *quantum oscillations* in a non-metallic state and *magnetoresistance oscillations* [53–55]. The susceptibility of $Ca_3Ru_2O_7$ to external influences such as temperature, magnetic fields [56, 57], pressure [58, 59], or chemical substitution [60–67] demonstrates the precarious balance between competing energy scales.

1.4 Thesis overview

This work concentrates on the insulating AFM phases of calcium ruthenates and investigates their static and dynamic magnetic properties using neutron spectroscopic techniques. We first review the literature on the systems under study in chapter 2 and

discuss possible mechanism that can lead to magnetism in calcium ruthenates. As a large part in the studies we devoted to the growth of single crystals, their characterization, and sample preparation, we discuss these aspects in chapter 3. We introduce the neutron scattering methods in chapter 4 as well as the instruments used in this work.

The experimental part concentrates on the role of SOC in ruthenate systems. In chapter 5 the results from unpolarized inelastic neutron spectroscopy experiments are presented, which highlight the importance of SOC in the system. Ruling out spin-only models we turn to the soft-moment magnetism model pioneered by Khaliullin [68]. In this model, the nominal non-magnetic singlet groundstate hybridizes with a magnetically active excited state, establishing a finite condensate occupation that renders the system magnetic. Oscillations of the condensate density modulates the moment size and thus introduces an intense amplitude (Higgs) mode in addition to the transverse (Goldstone) modes. Upon observing three distinct magnetic excitations—including the Higgs mode—in a polarized inelastic neutron scattering (INS) study we find experimental evidence for the proposed soft-moment magnetism. In particular, the model accurately describes the decay of the Higgs mode into transverse magnons in some regions of the Brillouin zone. To further explore the properties of calcium ruthenates, we investigated the system by chemical substitution. In chapter chapter 6 we detail our investigation into the system's response to Sr doping and follow the evolution of the Higgs mode.

By going to $Ca_3Ru_2O_7$ the quasi two-dimensional physics becomes more three-dimensional as coupling between bilayers of RuO_6 octahedra is introduced. However, in contrast to Ca_2RuO_4, $Ca_3Ru_2O_7$ exhibits a very different behavior, as each bilayer orders ferromagnetically. Consequently, only little can be learned about the influence of dimensionality onto the antiferromagnetic state from the pristine $Ca_3Ru_2O_7$ compound. We used inelastic neutron scattering experiments with and without applied magnetic fields to investigate the compound in chapter 7 and find that it can be described by a spin-only Hamiltonian. Surprisingly, the G-type antiferromagnetic insulating behavior of single layer Ca_2RuO_4 can be recovered in $Ca_3Ru_2O_7$ upon marginal Ru substitution with Ti. We provide extensive experimental evid-

ence obtained from neutron diffraction and inelastic scattering experiments (chapter 8) that indicates the close analogy of the magnetism found in $Ca_3Ru_{2-x}Ti_xO_7$ with the one found in single-layer Ca_2RuO_4.

The present work gives comprehensive insights into the importance of SOC for the magnetism of Ca_2RuO_4, as the excitonic magnetism model used to describe the experimental data establishes SOC as one of the driving forces that realize a magnetic ground state in Ca_2RuO_4 and $Ca_3Ru_2O_7$. We investigate the effects of chemical substitution as well as effects introduced by going to more 3D-like exchange interactions and establish ruthenates as a system to investigate the Higgs mode decay mechanism in a solid state material platform.

Chapter 2

Layered ruthenium oxides
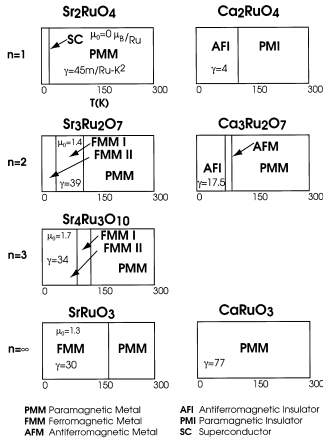
Figure 2.1: Trend of the magnetic phases of the $(Ca_{1-x}Sr_x)_{n+1}Ru_nO_{3n+1}$ system. (figure adapted from [49], modified)

L AYERED RUTHENIUM OXIDES have received a lot of interest in the solid state community as they are associated with phase diagrams that display an extraordinary wealth of magnetic, electronic, and structural phases. In this chapter we review the body of work both for the single layer as well as for the bilayer ruthenium oxides, and provide some fundamental considerations to understand the magnetic phenomena of the system.

(a) Ca_2RuO_4 (b) *Phase diagram*   (c) Sr_2RuO_4

Figure 2.2: Magnetic phase diagram of Ca_2RuO_4 as a function of Sr content x and temperature. The different magnetic phenomena are introduced by structural distortions due to the difference in the ionic radii of Ca and Sr, which are readil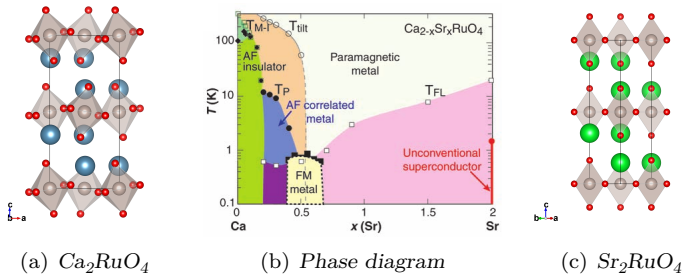y visible from the structure plots. (Figure (center) from [69]. Reprinted with permission from AAAS. Structural data from [70, 71])

2.1 Single layer ruthenates

In the $Ca_{2-x}Sr_xRuO_4$ series the Ca and the Sr cations are isovalent but of different ionic radii, resulting in structural differences between the endpoints Ca_2RuO_4 and Sr_2RuO_4. These structural distortions controlled through the Ca content lead to many phases, including superconductivity in Sr_2RuO_4, Mott-insulating behavior in Ca_2RuO_4, and a metallic phase with short-range ferromagnetic (FM) fluctuations for $Ca_{0.5}Sr_{1.5}RuO_4$.

Strontium ruthenate

The research into perovskite structures was sparked by the discovery of high-T_c superconductivity (SC) in cuprates in 1986 [27]. In these materials the copper-oxygen planes result in quasi-two-dimensional electronic states, which have been identified as one of the necessary ingredients for the unconventional SC. Consequently, similar perovskite-like structure were tested for SC. After eight years, Maeno et al. found SC in Sr_2RuO_4 with a T_c of 1.5 K. The new ruthenate system is iso-structural to the cuprate mother compound $La_{2-x}Ba_xCuO_4$ but has a different electron con-

figuration ($3d^9$ in cuprates, $4d^4$ in ruthenates) and consequently an integer spin quantum number of $S = 1$, contrasting the half-integer spin of $S = 1/2$ of the cuprates. A further difference is the symmetry of the wave-function of the SC state: Experimental evidence indicates a spin-triplet symmetry [72] of the Cooper pairs in the ruthenate system whereas those in the cuprates exhibit spin-single symmetry; however, the discussion on the pairing mechanism in Sr_2RuO_4 is still ongoing as experimental evidence is inconclusive [73], but it is agreed that spin-orbit coupling (SOC) plays an important role [74, 75] as its interaction strength λ is estimated to be $50\,meV$ to $100\,meV$ [76–78]. Above T_c the system is metallic with highly anisotropic Fermi liquid behavior that can be inferred from measurements of the Shubnikov-de Haas effect [79, 80] and the de Haas–van Alphen oscillations [79, 81–84].

Substitution series $Ca_{2-x}Sr_xRuO_4$

Usually, chemical substitution levels of several percent are needed to drive the system into a new phase. The insulator $LaTiO_3$, for example, shows metallic behavior for $5\,\%$ Sr substitution ($Sr_{0.05}La_{0.95}TiO_3$) [85]. Experiments on ruthenates however have shown that the these materials can be extremely susceptible to chemical impurities. Mackenzie et al. investigated the dependence of SC on impurity density in Sr_2RuO_4 and found that the SC state is quickly destroyed upon minute impurity implantation on B and A sites [86]. In order to investigate the effects of lattice distortions, Ca substitution provides an easily accessible approach. The smaller Ca anion causes gradual lattice distortions, which are expressed by a reduced c lattice parameter, and increasing rotations and tilts of the RuO_6 octahedra. The structures from high resolution powder diffraction measurements [70, 71] in figure 2.2 illustrate these changes. At the same time both elements are *alkaline earth metals* and thus iso-valent, but the electronic properties changes as the $Ru-O-Ru$ bonds buckle under the RuO_6 distortions. As a result the $4d$ band width considerably narrows [70, 87–90], leading to a several phases.

For dilute levels of Ca, $Ca_{2-x}Sr_xRuO_4$ remains in a non-magnetic 2D Fermi liquid phase. As the Sr content is further reduced, ferromagnetic (FM) fluctuations are observed and finally result in

a FM metal regime ($x \approx 0.5$). With higher Ca levels between ($0.2 < x < 0.5$) an antiferromagnetically correlated metal is realized. Magnetization measurements show Curie-Weis behavior in this phase that indicates a spin $S = \frac{1}{2}$ moment [91]. At $x = 0.2$ the system undergoes a metal-to-insulator transition (MIT) into a Mott-insulating state [92], concurrent with the onset of antiferromagnetic (AFM) spin order and structural changes.

We note that $Sr_{2-x}Ba_xRuO_4$ ($x < 0.4$) realizes the opposite effect: While Ba is larger than Sr it does not rotate or tilt the RuO_6 octahedra but maintains the system's symmetry. The properties of $Sr_{2-x}Ba_xRuO_4$ are similar to those of Sr_2RuO_4, but the superconducting phase as well as the FM spin fluctuations are absent [93].

The phases of Ca_2RuO_4

Ca_2RuO_4 undergoes several thoroughly interesting structural and magnetic phase transitions over a large temperature scale from $0\,K$ to $650\,K$. At high temperature, it forms a rather undistorted tetragonal crystal lattice and exhibits the transport properties of a bad metal. There are reports of two different configurations of Ca_2RuO_4 in polycrystalline powders [70], which differ in their lattice distortions and their oxygen content. Stoichiometry Ca_2RuO_4 (S-phase) is associated with a short c lattice parameters at room temperature and contrasts the L-phase, which is characterized by oxygen excess and a large c lattice parameter indicative of the more regular lattice of the metallic $Ca_{2-x}Sr_xRuO_4$ phase. While powder samples can be prepared in both L- and S-phase configurations, single crystals grown using the optical floating zone method have only been observed in the S-phase.

Temperature dependent phases With decreasing temperature, the S-phase remains paramagnetic but transitions to a Mott-insulating state at $T_{MIT} = 357\,K$ that is associated with dramatic changes to the crystal structure [88]. The structure of this phase (*Pbca*) is characterized by rotation of the octahedra about the c axis and tilts about an axis in the a, b plane [70] that change with temperature (see figure 2.3a). Alexander et al.
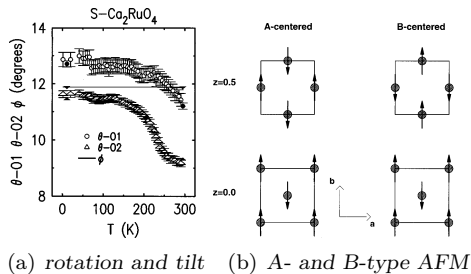
(a) *rotation and tilt*   (b) *A- and B-type AFM*

Figure 2.3: Temperature dependence of rotation and tilt angles of Ca_2RuO_4, figures 2.3a and 2.3b. (figures adapted from [70])

argue that the structural distortions of Ca_2RuO_4 at low temperatures [70, 94, 95] minimize the elastic energy $E_{elastic}$, while at high temperature thermally induced vibrations stabilize a more regular structure. The associated MIT thus depends on the buckling of the $Ru-O-Ru$ bonds and the in-plane electronic bandwidth $\mathfrak{W}$. Such a MIT decoupled from spin degrees of freedom makes Ca_2RuO_4 an exceptional model system for Mott transitions. The insulating paramagnetic phase orders antiferromagnetically below the Néel temperature of $T_N = 113\,K$ [88, 96] with an A-type stacking pattern shown in figure 2.3b. The moment direction is parallel to the b crystallographic axis, with a canting into the a direction of less than 5°. The size of the magnetic moment established in experiments is $\mu = 1.3\mu_B$ [70], which deviates from the naive expectation of $\mu_{exp} = 2\mu_B$ for this spin $S = 1$ system.

The closely related L-phase of Ca_2RuO_4 shows generally a much less distorted structure and remains in a pseudo-tetragonal structure ($P2_1/c$) and transitions to the distorted *Pbca* phase below 150 K. However, even at low temperatures the deformations of the lattice are not as severe as the ones found for the S-phase [70]. Similar to the L-phase, the system becomes insulating and develops an antiferromagnetic (AFM) spin order of the B-type stacking order pictured in figure 2.3b.

Phases introduced by pressure A further approach to exert structural control using external pressure or epitaxial strain

provides another path to modify the structure. The approach using pressure or strain does not introduce chemical impurities, and thus can offer a *cleaner* approach to control lattice deformations. The sample environment or the low mass in thin film samples however impose restrictions on the experimental methods. The group of Prof Maeno has performed several isotropic [97, 98] pressure studies that show that for pressures higher than $0.5\,\mathrm{GPa}$ Ca_2RuO_4 transitions into the L-phase, which also has a smaller volume per unit cell compared to the S-phase. In this configuration, a transition to a ferromagnetic metallic phase is observed, which is accompanied by a first order structural transition from the S to the L-phase [99]. Uniaxial pressure studies [100, 101] show that the system undergoes a MITs at slightly higher pressures ($1.5\,\mathrm{GPa}$) for in-plane pressure. Recent experiments on epitaxial films of Ca_2RuO_4 with compressive strain stabilize a very similar low temperature ferromagnetic phase [102] which is characterized by a large c lattice parameter indicative of the L-phase in bulk Ca_2RuO_4.
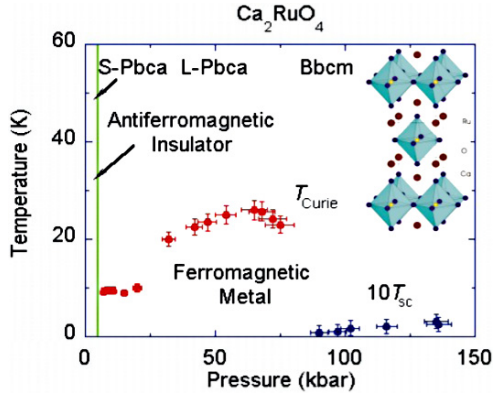

Figure 2.4: Pressure-temperature phase diagram of Ca_2RuO_4 showing the onset of the proposed superconductive state at $90\,\mathrm{GPa}$. (figure adapted from [103])

At high temperatures ($> 600\,\mathrm{K}$ at ambient pressure) or high pressures ($5.5\,\mathrm{GPa}$ at room temperature) the tilting of the octahedra is suppressed and the lattice is described by the *Bbcm*

space group. Only recently, pressure experiments [103] below 1 K were able reach this phase at pressures exceeding 9 GPa where the ferromagnetic fluctuations vanish. At the same time, a phase bearing the signatures of superconductivity is observed below $T_{sc} = 0.4$ K.

Further chemical substitution studies Interestingly, Riccò et al. combined strain and chemical substitution to tune the system across the MIT [104]. They substitute Ca for trivalent Pr, which does not introduce itinerant carriers. From our discussion on the effect on A-site substitution on the lattice energy $E_{elastic}$ (section 6.1) we find that Pr substitution should have similar effects to Sr substitution, as the ionic radii are very similar ($r_{Pr^{3+}} = 1.18$ Å) and $r_{Sr^{2+}} = 1.1$ Å). And indeed, the phase diagram of $Ca_{2-x}Pr_xRuO_4$ [104]) is almost identical. The group observes a Mott MIT driven by the competition between the formation of a Fermi liquid and gain in elastic energy by lattice distortions. The similarities extend to the system's behavior under pressure or strain, as the group shows by investigating the Fermi surface using ARPES while straining the system.

Non-equilibrium phases Recent studies show that the Mott-insulating state can be suppressed by applying a small electric field of about 40 V cm^{-1}. At the same time, the system undergoes a bulk structural transition into a phase similar to the L-phase [97]. Bertinshaw et al. investigated the structural properties of this non-equilibrium phase with neutron diffraction measurements and were able to establish the existence of three distinct phases; namely the equilibrium S-phase, and a modified S*-phase and L*-phase. While the lattice parameters of the non-equilibrium phases are similar to those of the respective equilibrium phases the observed lattice distortions, namely flattening, tilt and rotation of the RuO_6 octahedra, are reduced [105]. Density functional theory $(DFT + U)$ calculations show that the applied current stabilizes electron pockets near the Fermi level indicating semi-metallic behavior, which is accompanied by a strong diamagnetic signal [106].
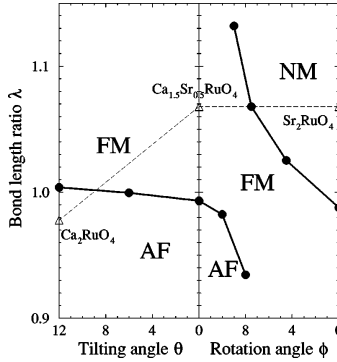
31

Figure 2.5: Phase diagram detailing the magnetic phases Ca_2RuO_4 depending on the tilt and rotation angles as well as the c lattice parameter. (figure adapted from [94])

Recurring structural characteristics From these observations obtained in Sr-substitution and pressure studies, references [91, 97] conclude that the different combination of lattice distortions favor specific electronic and magnetic states: In order to compensate for the ionic size mismatch when replacing the Sr-site with Ca, or in response to externally applied pressure, the system undergoes a number of distortions of the RuO_6 octahedra. The AFM insulating S-phase expresses flattened RuO_6 octahedra and larger tilt angles. On the other side, the L-phase systems tend towards less flattening. If the octahedra in this phase are *rotated and tilted*, an AFM correlated metal is realized (as observed for $Ca_{2-x}Sr_xRuO_4$ with $0.2 < x < 0.4$). For rotated, but otherwise undistorted octahedra a state characterized by ferromagnetic fluctuations is favored (maximum at x 0.5 in $Ca_{2-x}Sr_xRuO_4$) and the resistivity normal to the RuO_2 plane is suppressed. These findings are depicted in the phase diagram in figure 2.5 [94].

Search for the origin of magnetism in Ca_2RuO_4

The symmetry of the system is dictated by the regular coordination of O^{2-} ions around the central Ru^{4+} ion, that replaces the atomic spherical symmetry with a cubic one. In this setting,

Hund's coupling forces all four valence d electrons of Ru^{4+} to share the three t_{2g} orbitals in a low spin configuration. From that we expect a spin $S = 1$ system with a reduced angular momentum $L_{\mathrm{eff}} = 1$.

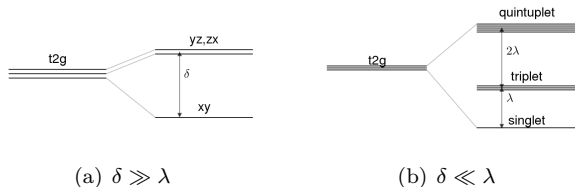(a) $\delta \gg \lambda$ (b) $\delta \ll \lambda$

Figure 2.6: Two possible energy hierarchies in $4d$ TMOs. *left*: distortions split the t_{2g} levels, and strong Hund's coupling enforces a low-spin configuration. *right*: strong SOC couples the low-spin $S = 1$ moment and the $L_{\mathrm{eff}} = 1$ angular moment of the t_{2g} subshell to J_{eff} levels.

Up until recently, magnetism in ruthenates has been exclusively modeled using a spin-only Heisenberg model. This approach mirrors the physics of $3d$ TMO systems, where SOC is often fully quenched or can be handled as a rather small perturbation. For ruthenates however, SOC plays an important role. This circumstance is reflected by large single ion anisotropy terms that are required when modeling the experimentally observed magnon dispersion. Elliott and Thorpe explicitly note that in a system with active orbital angular moments the system may not be described with a Heisenberg model [33]. Instead, S is no longer a good quantum number and the influence of SOC is taken into account by a description using pseudo-spin $J_{\mathrm{eff}} = L_{\mathrm{eff}} + S$ states that arise from the coupling of spin and orbital angular moments.

Considering coupled spin and orbital angular momentum states for the Ca_2RuO_4 system ($S = 1$, and $L_{\mathrm{eff}} = 1$), the ground state is expected to be a non-magnetic $J_{\mathrm{eff}} = 0$ singlet state. Naively, the conflict between this singlet ground state and the apparent magnetic order may explain why this scenario has been dismissed in the past. Recently, Khaliullin proposed partial condensation of electronic excitations in the first excited $J_{\mathrm{eff}} = 1$ states that carry a magnetic moment driven by exchange interactions between the Ru ions. This way, a soft moment magnetism with a staggered

magnetic moment can be realized in $4d^4$ systems [68], which would reconcile the singlet ground state of the SOC Hamiltonian with a magnetically ordered phase. A hallmark feature of such an *excitonic magnetism* is an intense amplitude mode, where fluctuations of the population of the excited state translate into oscillations of the moment size. Akbari and Khaliullin calculated the magnon dispersion of Ca_2RuO_4 and predicted a rather unusual spectrum for an AFM system [107], that includes an amplitude mode that should be observable in neutron spectroscopic studies.

2.2 Bilayer calcium ruthenium oxides

The influence of inter-layer coupling can be gradually increased by going to higher members of the Ruddlesden-Popper (RP) series. As indicated in figure 2.1 certain trends can be observed: in $Sr_{n+1}Ru_nO_{3n+1}$ the FM fluctuations present in a wide range in $Ca_{2-x}Sr_xRuO_4$ are stabilized for higher n and the magnetic ordering temperature T_n drops for calcium ruthenates when going to higher RP members. On the Ca side however, the trend is not so straightforward; as magnetic phases correlate strongly with the distortions of the lattice, the single members are extremely susceptible to external forces which can have a dramatic impact upon the ground state.

$Ca_3Ru_2O_7$ is one of the most versatile systems in this regard, encompassing many of the correlated phases expressed by TMOs. At high temperature $Ca_3Ru_2O_7$ is a paramagnetic metal (PM-M), a common property of $Ca_{n+1}Ru_nO_{3n+1}$ compounds. Upon cooling it remains conducting even after it orders and transitions into an AFM state at $T_N = 56$ K. In this state, the Ru^{4+} spins are aligned ferromagnetically within each bilayer but the net moment cancels due to the AFM stacking of the bilayers. At $T_{MIT} = 48$ K the system goes through a metal to non-metal transition that is associated with a small change in lattice parameters and a change in the magnetic anisotropy as the spins keep their relative alignment but the easy axis changes from a to b. Previous studies labeled these AFM phases *AFM-a* and *AFM-b*, respectively. Upon further cooling, the system shows highly anisotropic transport properties with a low carrier density, where conductivity is
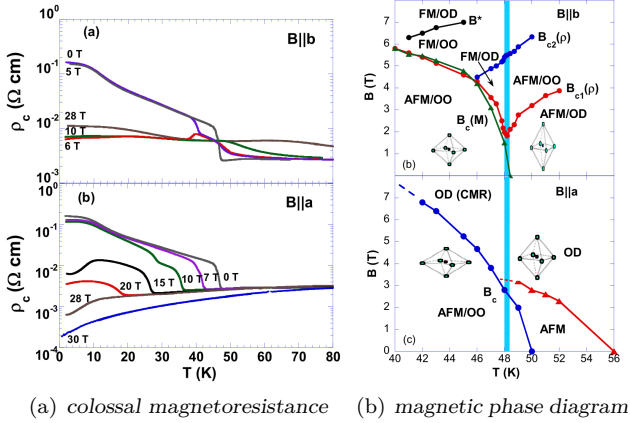
confined to the Ru layer.

(a) *colossal magnetoresistance*   (b) *magnetic phase diagram*

Figure 2.7: *left*: Colossal magnetoresistance of the out-of-plane resistivity ρ_c for magnetic fields parallel to the b axis in the AFM-b phase. (figures adapted from [48])

Under applied magnetic field the system shows a range of peculiar behaviors [48]: notably *colossal magnetoresistance* (CMR) that occurs upon suppression of the spin-polarized FM state [51, 53–56, 58, 108–110], which can be achieved by applying a magnetic field perpendicular to the easy magnetization axis. This mechanism is different from the one observed in pseudocubic manganites, which show CMR as the polarized state is approached. Further more, it shows a *bulk spin-valve* behavior [52, 65]. Spin-valve effects are usually only observed in thin film systems, in which FM layers alternate with non-magnetic buffer layers—a natural property of the layered $Ca_3Ru_2O_7$ system. In the non-metallic magnetic phase there have even been observations of quantum oscillations [51, 53–55, 108] indicating the presence of small electron pockets in the Fermi surface, which were subsequently found by ARPES measurements [111].

Recently several groups have reported on dramatic changes of the physical behavior of $Ca_3Ru_2O_7$ upon minute Ti-substitution levels as low as 0.3%[67]: The quasi two-dimensional metallic phase of pure $Ca_3Ru_2O_7$ transitions into an insulating phase con-

comitant with structural changes, a change in spin structure [112], and strong magnetoresistive coupling [113]. In the Mott insulating state with $3\,\%$ Ti substitution the system is also susceptible to pressure, which introduces localized electronic states and recovers the AFM-b spin order of the parent compound for isotropic pressures of $\approx 1\,\text{GPa}$ [114] - which is in fact similar to the pressure studies in the single layer compound discussed earlier.

Chapter 3

Growth of calcium ruthenate single crystals

H IGH QUALITY CRYSTAL GROWTH and sample preparation are the foundation for any spectroscopic studies. In the context of this thesis single crystals of single and bilayer ruthenates were grown by the optical floating zone (OFZ) technique using mirror furnaces. Since the process does not rely on crucibles, it is possible to grow materials contact-free and without the possibility of external contamination, and thus obtain large, stoichiometrically *clean* single crystals. After characterization of their structure and magnetic and resistive properties we carefully prepared sample arrays suitable for neutron scattering and diffraction experiments.

3.1 The optical floating zone technique

In an optical mirror furnace photons emitted by infrared halogen lamps are focused in a small volume to generate high power densities of $\approx 12\,kW/ccm$. Sample material placed in the focal point and absorbing the energy is heated to several thousand °C and melts the material in the process.

Mirror furnaces employ elliptical mirrors that focus the radially emitted light from the filament in the one focal point onto the second focal point, in which the sample material is placed.

Typically, a setup has two or four mirrors coordinated in the horizontal plane around a vertical reactor volume. In order to meet growth conditions of high temperatures (about 1400 °C) and pressure levels of up to 10 atmospheres, the sample volume is a sealed environment with transparent reactor walls made from quartz glass.
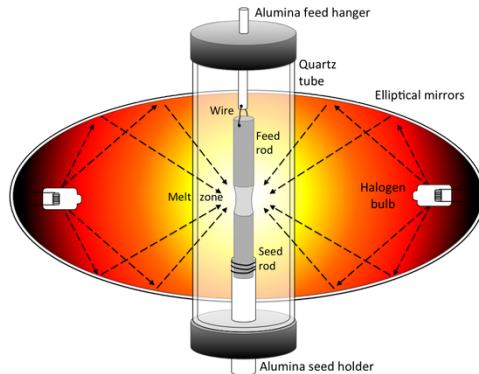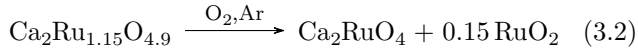

Figure 3.1: Diagram of a mirror furnace used for growing crystals using the *optical floating zone* technique, reproduced from [115] with permission.

For the growth procedure, amorphous precursor material is pressed into a cylinder (*feed rod*), which is suspended in the sample volume just above the focal point, as depicted in figure 3.1. By lowering the lower feed rod tip into the focal point only a small portion of the precursor material is heated above melting temperature. In order to grow high quality crystals, a seed crystal is lifted into the precursor melt from below, providing an initial crystalline seed from which the final crystal is grown. After the seed and the precursor have been connected in this initial step, the hot zone is swept through the precursor material by moving the mirrors relative to the feed rod. Sample material moving into the hot zone melts and crystallizes as it cools upon leaving it.

$$1.15\,RuO_2 + 2\,CaCO_3 \xrightarrow{\text{air}} Ca_2Ru_{1.15}O_{4.9} + 2\,CO_2 \qquad (3.1)$$

$$Ca_2Ru_{1.15}O_{4.9} \xrightarrow{O_2,Ar} Ca_2RuO_4 + 0.15\,RuO_2 \quad (3.2)$$

Table 3.1: Exemplary calcification reaction for Ca_2RuO_4.

Ruthenate sample growth using the OFZ method

To obtain the sample used in this project, we used a four-mirror optical floating zone furnace made by *Crystal Systems Corp.* (Japan) equipped with 1.5 kW lamps and a total power output of 6 kW. To reach the melting temperatures of ruthenates of about 1500 °C the machine was typically operated at 90 % power (≈ 5.5 kW).

Precursor material and feed rod

The precursor material is obtained from a solid state reaction of an off-stoichiometric mixture of RuO_2 and $CaCO_3$ (each 99.9 % or better). To this end, the fine powders are carefully weighted and mixed in an agate mortar until a homogeneous powder is obtained. The mixture is calcined in a box furnace to 1000 °C for a total time of 20 h under air atmosphere. In case of chemical substitution with TiO_2 or $SrCO_3$ this process might be interrupted for additional grinding in an agate mortar after 10 h which increases the homogeneity of the mixture.

The finished precursor powder is then filled in uncolored latex balloons[1] and pressed in a hydrostatic press into dense cylindrical rods. The dimensions of the rod can be controlled through the diameter of a press mold used to create a symmetric cylinder. During preparation, it is important that the powder in the balloon is distributed uniformly, since any density variations translate into a crooked rod or rods with varying cross section. Similarly, the balloon should be stretched uniformly to avoid buckling.

After an application of 60 kbar in an isostatic pressure cell a dense cylinder of the precursor material is obtained. These

---

[1]Qualatex No. 350

are usually robust enough be handled without further sintering. Using a 1 mm drill bit a small hole is made near the top to allow suspending the feed rod from a Pt wire.

Crystal growth

Before starting the actual growth process, the furnace is pressurized and heated to the growth temperature and kept idle for a short time to allow the furnace to thermalize. Only then stable operating parameters can be achieved.

The initial steps are to melt the tips of the feed rod and the seed crystal. Upon joining the two molten ends surface tension creates a floating liquid zone between the amorphous feed rod and the crystalline seed. To ensure homogeneity of the melt, the precursor rod and the seed are rotated in opposite direction as the hot zone moves through the material.

The available parameter space for growth conditions is vast, and the growth procedure is optimized for each compound. Some main growth characteristics depend on a combination of parameters: The *diameter of precursor rod* affects the powder density, which, together with the *density of the precursor material*, determines the required lamp power to melt the crystals. The *atmosphere* provides oxygen during the growth process and as volatile RuO_2 sublimates at elevated temperature partial pressures change with the total *pressure* in the reactor volume and the temperature of the melt. The *relation between growth speed and power density* determines the speed of crystallization and is the main optimization parameter responsible for single- or multi-domain crystallization. The shape of the molten zone is influenced by its surface tension and its *viscosity*, which, again, depends on the *melt temperature*. The solid-liquid interfaces are influenced by the *temperature gradients* as well as the *speed of rotation* of the precursor and the seed rod.

Challenges during growth of ruthenium oxides

While most crystals are grown with a few $mm\,h^{-1}$ ruthenates require growth speeds of about $20\,mm\,h^{-1}$ to $40\,mm\,h^{-1}$ [116], reducing the growth time to a few hours. In general, it can be

expected that growth parameters change over time as an equilibrium of the RuO_2 partial pressure sets in, the IR filaments and the elliptical mirrors reach operating temperature, and the temperature gradient within the material is steady. This leaves only little time to adjust growth conditions during growth.

The main difficulty is to obtain a stoichiometric composition of the final crystal. Pure RuO_2 has a sublimation temperature of $800\,°C$ well below the melting temperature of the system, which results in high partial pressure of RuO_2 in the pressure sealed growth chamber. To compensate the loss of Ru in the melt, the precursor contains excess Ru compared to the stoichiometry of the desired compound. In case of the $Ca_{2-x}Sr_xRuO_4$ ($Ca_3Ru_{2-x}Ti_xO_7$) system, a surplus of $15\,\%$ ($27.5\,\%$) Ru was used. An ancillary effect is the clouding of the quartz walls of the reactor chamber as RuO_6 re-sublimates. The clouding effect leads to a decreased infrared transmission. It can be mitigated by allowing a constant gas exchange with the feed at the bottom and the exhaust located at the top of the reactor chamber. However, this washing process requires a stable RuO_6 partial pressure.

Further complications arise in preparing systems with dilute dopants. Here, the quality of the precursor material is an even more important issue, since only a fraction of the whole feed rod is fused at any given time. As a result, any inhomogeneous distributions of the dopant within the precursor directly translates to the single crystals. To avoid inhomogeneities, the precursor powder was mixed using mortar and pestle for extended time before, during, and after the two-step sintering process.

3.2   Sample characterization

Each batch of crystals is first judged visually - small, inter-grown crystallites indicate inhomogeneous growth conditions which might result in a mixture of phases, inclusions, growth or stacking faults and in general in a bad mosaicity of the crystals. Similarly, if the crystals shatters not only into shards but amorphous powder is produced as well, the batch has a poor crystallinity.

Phase determination

Promising batches are subsequently characterized by powder X-Ray diffraction, which is sensitive to different phases such as different configuration or the single layer or double layer perovskites. Especially in Ca_2RuO_4, two phases with distinct structures and magnetic behavior have been observed, labeled *S* and *L*-phases in reference to their short / long *c* lattice parameter.

Chemical composition

To determine the stoichiometric composition, we performed *energy dispersive X-ray spectroscopy* (EDX) and *inductively coupled plasma atomic emission spectroscopy* (ICP-AES). While EDX only gives returns a relative atomic composition, ICP-AES is an absolute measurement. Since both techniques perform very poorly when determining the O content of the sample, is has a larger impact on results of the EDX method. To obtain a meaningful result, we normalized the results to the nominal Ca content. While content of substituted elements correspond to the expected values, EDX usually underestimates the Ru content.

To assess the O content of the sample, the chemical synthesis service group performed pyrolysis of the compounds in graphite crucibles. Heating those with the material under study oxidizes the C to gaseous CO_2. From the mass difference, we found essentially stoichiometric Oxygen content in all samples under study (see table 3.2).

3.3   Sample preparation for neutron experiments

Since large sample volumes are needed for inelastic neutron scattering studies we were required to co-align crystals. Especially in case of the Ca_2RuO_4 system only small crystals can be obtained, which requires co-alignment into a larger array of sufficient mass.
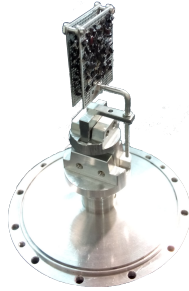
Figure 3.2: Sample used in the ARCS [1, 2] TOF INS measurements: about 200 co-aligned crystals totaling 3 g.

Neutron array

In order to reach a sample mass of approximately 1.5 g to 3 g needed for inelastic neutron scattering (INS) experiments we typically co-aligned about 100 to 200 crystals. The support was provided by either Al or Si plates. While the first option is almost transparent for thermal neutrons due to aluminum's small total scattering cross section σ_{abs}, the second option is the *de facto* standard in the neutron community. Si can be grown as single crystals of exceptionally high quality, making its Bragg peaks extremely sharp, so that they interfere with the signal from the sample only at isolated, easily identifiable points. Since no magnetic scattering occurs, it provides an ideal material for INS experiments that are restricted to the first couple of Brillouin zones.

Typical arrays were made up by 150 to 250 crystals for the single-layer ruthenate samples, or 30 to 75 crystals for the bilayer ruthenate samples. The mosaicity of such an array was usually better than 4°.

measurement	performed by	performed on	results
powder XRD	Christine	all crystalline samples	
EDX	Busch	condensed material during OFZ-growth	
EDX	Busch	Ca_2RuO_4: precursor (*mjk-0068*)	$Ru : O_2 = 1.13 : 1$, $Ca_2Ru_{1.45}O_{4.94}$
EDX	Predel	$Ca_3Ru_2O_7$ (*mjk-0051*)	$Ca_{3.0(2)}Ru_{2.3(2)}Ti_{0.0(1)}O_{6.2(5)}$
EDX	Predel	$Ca_3Ru_2O_7$ (*mjk-0051*)	$Ca_{3.0(2)}Ru_{2.3(2)}Ti_{0.0(1)}O_{6.3(5)}$
EDX	Predel	$Ca_3Ru_2O_7$ (*mjk-0052*)	$Ca_{3.0(2)}Ru_{2.4(2)}Ti_{0.0(1)}O_{6.9(5)}$
EDX	Predel	$Ca_3Ru_{1.98}Ti_{0.02}O_7$ (*mjk-0053*)	$Ca_{3.0(3)}Ru_{2.3(2)}Ti_{0.02(9)}O_{6.8(7)}$
EDX	Predel	$Ca_3Ru_{1.98}Ti_{0.02}O_7$ (*mjk-0053*)	$Ca_{3.0(3)}Ru_{2.2(2)}Ti_{0.02(9)}O_{6.7(7)}$
EDX	Predel	$Ca_3Ru_{1.98}Ti_{0.02}O_7$ (*mjk-0054*)	$Ca_{3.0(3)}Ru_{2.3(2)}Ti_{0.03(9)}O_{6.3(7)}$
EDX	Predel	$Ca_3Ru_{1.98}Ti_{0.02}O_7$ (*mjk-0054*)	$Ca_{3.0(3)}Ru_{2.3(2)}Ti_{0.02(9)}O_{6.2(7)}$
EDX	Predel	$Ca_3Ru_{1.94}Ti_{0.06}O_7$ (*mjk-0055*)	$Ca_{3.0(3)}Ru_{2.2(2)}Ti_{0.07(9)}O_{6.4(7)}$
EDX	Predel	$Ca_3Ru_{1.94}Ti_{0.06}O_7$ (*mjk-0055*)	$Ca_{3.0(3)}Ru_{2.2(2)}Ti_{0.06(9)}O_{6.5(7)}$

Table 3.2: Measurements performed by in-house service groups. EDX measurements give results in percent only and have been scaled to match the stoichiometric content of Ca.

Chapter 4

Experimental techniques

PROBING MATTER with photons or particles in diffraction or scattering experiments reveals its static and dynamic properties. Investigating elastic processes yields information on periodic structures and can be used to investigate atomic positions or spin orientation in a material. Inelastic neutron scattering experiments allow to directly observe excitations in solid state matter and have been an elemental tool for solid state research since their development in 1956 by Brockhouse.

In this work we have used a wide array of different techniques to investigate Ca_2RuO_4 and related compounds, with a focus on inelastic neutron scattering techniques. In this chapter we will briefly present important topics of the theory describing neutron scattering events, differentiate between elastic an inelastic experimental techniques, and introduce the instruments used in the context of this project. We will also touch on important aspects of data analysis.

4.1 Basic theory of neutron scattering methods

Neutrons have rather small probability to interact with matter, making a nuclear reactor or neutron spallation source generally required to generate enough neutrons for scattering experiments and achieve statistically relevant data sets in a reasonable time span.

Nuclear reactors rely on the fission processes to split Uranium atoms into daughter nuclides and free neutrons, similar to commercial nuclear power plants. Spallation sources bombard a target material with relativistic particles resulting in the spallation of involved nuclei and subsequent showers of the fragments. Both processes generate neutrons of a broad energy bandwidth, which can be controlled in fission sources using appropriate neutron moderation. The neutrons are then guided to the instrument, where the *white* neutron beam is prepared such that only neutrons with a defined initial state enter the spectrometer. Then the probe is directed onto a sample, where the individual neutrons interact with the present nuclei and magnetic moments. Due to these scattering events the initial state of the neutrons changes, which can be observed with the right instrumentation. For a schematic of the scattering process see figure 4.1.
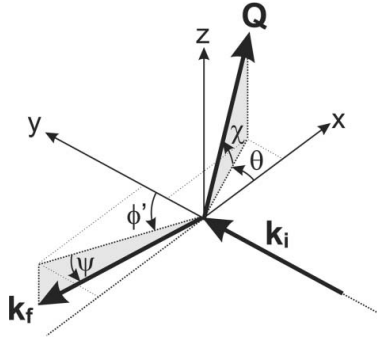
Figure 4.1: In all neutron scattering experiments neutrons with a known initial state (momentum $\boldsymbol{k}_i$) are directed onto a sample volume, from which they are scattered into their respective final states, characterized by the final momentum vector $\boldsymbol{k}_f$ and the scattering angles θ and χ that determine the transferred momentum $\boldsymbol{Q}$. Reproduced with permission of the International Union of Crystallography from [117].

By preparing the initial state of the incident neutrons and comparing it to the final state we can draw conclusions to the nature of the interaction by comparing to theoretical models. The scattering rate $\Gamma_{i \to f}$ is generally described through *Fermi's Golden Rule*. For an event in which a prepared initial state $|i\rangle$

transforms into an observed final state $\langle f|$ due to an interaction potential H it takes the following form:

$$\Gamma_{i \to f} = \frac{2\pi}{\hbar} \left| \langle f|H|i \rangle \right|^2 \delta(E_i - E_f - \hbar\omega) \qquad (4.1)$$

where the delta-function asserts energy conservation.

Applied to neutron scattering, the interaction potential is that of the sample constituents. The differential cross section of a scattering event at lattice cite $\boldsymbol{R}$ with a certain energy transfer $\hbar\omega = E_f - E_i$ and momentum transfer $\boldsymbol{Q} = \boldsymbol{k}_f - \boldsymbol{k}_i$ takes the following form:

$$\begin{aligned}
\frac{d^2\sigma}{d\Omega d\mathrm{E}_f} = & \left(\frac{m_n}{2\pi\hbar^2} \right)^2 \frac{k_f}{k_i} \\
& \times \sum_{\lambda_i, \sigma_i} p_{\lambda_i} p_{\sigma_i} \sum_{\lambda_f, \sigma_f} \left| \langle \boldsymbol{k}_f, \sigma_f, \lambda_f \left| \boldsymbol{U}(\boldsymbol{R}) \right| \boldsymbol{k}_i, \sigma_i, \lambda_i \rangle \right|^2 \\
& \times \delta \left(\mathrm{E}_i - \mathrm{E}_f + \hbar\omega \right)
\end{aligned} \qquad (4.2)$$

where m_n is the neutron mass; $\boldsymbol{k}_{i,f}$, $\sigma_{i,f}$, $\lambda_{i,f}$ represent the initial and final state of the the neutron momentum, neutron polarization, and sample state, respectively; $p_{\lambda,\sigma}$ is the probability of occupation in the initial state, and $\boldsymbol{U}(\boldsymbol{R})$ is the interaction potential at site $\boldsymbol{R}$. From this equation we can distinguish two cases of scattering events: (1) elastic scattering events with $\hbar\omega = 0$ which leave the neutron's energy unchanged, and (2) inelastic scattering events with $\hbar\omega \neq 0$ in which energy is transferred between the neutrons and the sample. We will visit both scenarios briefly, but will first make some remarks on the difference between nuclear and magnetic scattering events.

Nuclear neutron scattering

In a nuclear scattering event we consider neutrons interacting with the nuclei of the sample material by the strong-force interaction. The interaction potential (labeled $\boldsymbol{U}(\boldsymbol{R})$ in equation (4.2)) is approximated by the hard core Fermi potential

$$U_F(\boldsymbol{R}) = \frac{2\pi\hbar^2}{m_n} b \cdot \delta(\boldsymbol{R}), \qquad (4.3)$$

47

which is essentially determined by the element specific *scattering length b*, and the delta function which accounts for the short range character of the interaction. Closely related to the scattering length is the scattering cross section $\sigma[\text{barn}] = b^2[\text{fm}] \cdot {}^{4\pi}/_{100}$, which is usually given in the units of $[\text{barn}] = \exp^{-10}[\text{m}]$.

For simplicity, we rewrite 4.2 for nuclear scattering under the assumption of a single element species. Summing over the interaction potentials of all atoms in a sample is expressed in the follow form:

$$\left(\frac{d^2\sigma}{d\Omega dE_f} \right)_{\text{nuc}} = \frac{k_f}{k_i} \cdot 1 \cdot b^2 \cdot S_{\text{nuc}}(\boldsymbol{Q}, \omega) \qquad (4.4)$$

where the scattering function $S_{\text{nuc}}(\boldsymbol{Q}, \omega)$ is a scalar and the nuclear scattering length is isotropic.

Magnetic neutron scattering

The neutron has a magnetic moment of $\mu_n = -1.042 \cdot 10^{-3} \mu_B$ [118] interacts with magnetic fields.

$$U_B(\boldsymbol{R}) = -\boldsymbol{\mu}_n \cdot \boldsymbol{B}(\boldsymbol{R}) \qquad (4.5)$$

In matter, magnetic interactions with the neutron's magnetic moment μ_N can arise from the spin magnetic moment $\boldsymbol{S}$ or from the orbital moment $\boldsymbol{L}$ of unpaired electrons. The magnetic field reads

$$\boldsymbol{B}(\boldsymbol{R}) = \frac{\mu_B}{4\pi} \left(\frac{\nabla \times \boldsymbol{\mu}_n \times \boldsymbol{R}}{R^3} - e\frac{\boldsymbol{v}_e \times \boldsymbol{R}}{R^3} \right) \qquad (4.6)$$

Considering scattering form a spin-only system, a magnetic scattering length p can be defined in analogy to the nuclear scattering length b_{coh}:

$$p = -\gamma_n r_0 \frac{g}{2} \boldsymbol{\sigma} \cdot \hat{\boldsymbol{Q}} \times (\boldsymbol{S} \times \hat{\boldsymbol{Q}}) \qquad (4.7)$$

In equation (4.6) the first (second) term corresponds to the interaction with spin (angular) moments of the sample. Summing over all spins in the system, the double differential cross section for magnetic neutron scattering can be rewriting in the following

form:

$$\frac{d^2\sigma}{d\Omega dE_f} = \frac{k_f}{k_i} \cdot F^2(\boldsymbol{Q}) \cdot (\gamma_n r_o)^2 \cdot \sum_{\alpha,\beta} (\delta_{\alpha,\beta} - \hat{\boldsymbol{Q}}_\alpha \hat{\boldsymbol{Q}}_\beta) S_{\mathrm{mag}}^{\alpha\beta}(\boldsymbol{Q},\omega)$$

(4.8)

While the form of the magnetic double differential cross section is similar to its analogous equation for nuclear scattering equation (4.4), we note two distinct differences. First, the *magnetic form factor* $F(\boldsymbol{Q})$ is the Fourier transform of the normalized unpaired electron density. In contrast to the point-like nucleus, electrons are located in spatially extended orbitals, and thus $F(\boldsymbol{Q})$ varies with the momentum transfer. It decays rather fast with increasing $\boldsymbol{Q}$ and thus limits magnetic scattering to the first few Brillouin zones. Secondly, the *polarization factor*

$$P(\boldsymbol{Q}_\alpha \boldsymbol{Q}_\beta) = (\delta_{\alpha,\beta} - \hat{\boldsymbol{Q}}_\alpha \hat{\boldsymbol{Q}}_\beta) \qquad (4.9)$$

indicates that neutrons only scatter from the component of the magnetic moment that is perpendicular to $\boldsymbol{Q}$.

4.2 Neutron scattering techniques

In order to obtain the experimental data in the present thesis we used several instruments, each optimized for a specific investigation. We give a short overview on the different instrument types.

Neutron diffractometers

Neutron diffractometry is a common technique used to determine the magnetic spin structure of a system. The incoming neutron beam is monochromated to a single wavelength λ_i using high quality single crystals in Bragg scattering configuration and subsequent beam-shaping by an aperture. Higher order contamination due to high energy neutrons with $\lambda = n \cdot \lambda_i$ are eliminated with filter elements. These are made of Be or graphite, both of which are transparent for neutrons with λ_i only. For high-resolution measurements the beam divergence can be controlled by beam focusing elements (array of monochromator crystals) or

beam cutting Soller slits (array of blades that absorb divergent neutrons [119]). After the scattering event the neutrons are recorded by a movable single detector or an array of detectors covering a range of different scattering angles.

We have performed experiments using the high resolution diffractometer SPODI [17, 18] (schematics are reproduced in 4.2) and the high flux diffractometer E6 [5].
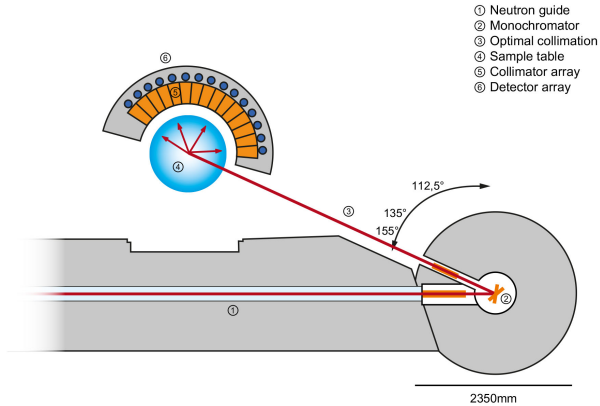

① Neutron guide
② Monochromator
③ Optimal collimation
④ Sample table
⑤ Collimator array
⑥ Detector array

112,5°
135°
155°

2350mm

Figure 4.2: SPODI [17, 18] instrument layout. (figure adapted from [18])

Neutron spectrometers

We have performed extensive studies on direct and indirect spectrometers. While indirect spectrometers detect scattered neutrons of specific fixed wave vector k_f direct spectrometers start with a fixed initial neutron wave vector k_i. As a consequence, there are distinct design consideration for each instrument configuration which ultimately influence the data obtained from each method.

Direct spectrometers

Direct spectrometers work with a fixed initial neutron wavelength and thus need detectors that are energy sensitive. The most com-
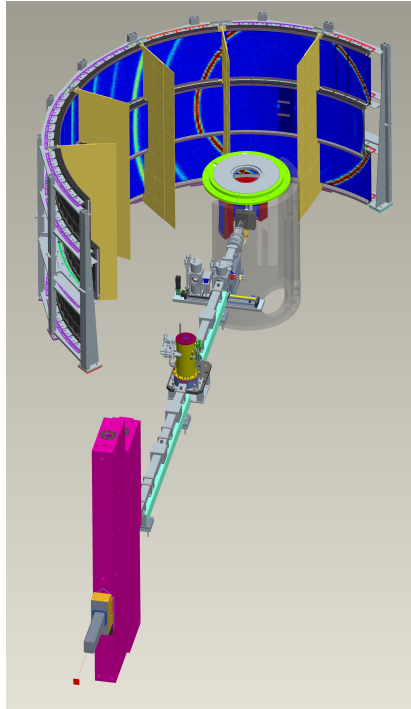
Figure 4.3: ARCS [1, 2] instrument layout. (image credit: ORNL Spallation Neutron Source)

mon design are time-of-flight (TOF) spectrometers that exploit the pulsed nature of the neutron beam of spallation sources. Using a series of *choppers* (spinning disks with cut-outs) the incoming neutron beam can be monochromated by choosing the window opening, spinning speed, and relative phase of each disk. Thus, the time t_0 of the scattering events can be chosen, and by measuring the time delay between t_0 and detection on the detector, the energy transfer between sample and neutron can be determined. Large area sensitive detectors allow for a large coverage of reciprocal space, and by rotating the sample a continuous data set along four dimensions $(\boldsymbol{Q}, E)$ can be obtained.

A different design for direct spectrometers utilizes the (reson-

ant) spin echo technique [120–124]. By controlling the number of spin rotations in a controlled environment it encodes the elastic energy transfer in the time domain with unprecedented energy resolution.

Indirect neutron spectrometers

The standard indirect setup is known as a triple axis spectrometer (TAS), the first of which was commissioned at the Chalk River Laboratories (Canada) by Brockhouse in 1956, who shared the Nobel prize with Shull in 1994. TAS usually work with a fixed final neutron wavelength that is optimized for the use of low pass filters in front of a single detector. Since suitable materials are limited the choice of k_f is usually limited to a few select wavelengths.

The initial neutron energy selection upstream of the sample is made by using monochromator crystals in a Bragg scattering configuration (first rotation axis). The sample orientation as well as the secondary instrument arm define the momentum transfer $\boldsymbol{Q}$ (secondary axis). In the third rotation axis a second crystal in Bragg scattering configuration is used to select the final momentum k_f of the neutrons. A drawing of a typical TAS is given in 4.4.

Comparison direct and indirect spectrometers

Due to the difference in the instrument layouts, direct and indirect spectrometers each have individual advantages and disadvantages. TAS make use of a continuous neutron beam these are with fission neutron sources, while TOF spectrometers are depended on the periodic to the neutron beam pulses generated by spallation sources.

The intensity for a single data point with momentum transfer $\boldsymbol{Q} = (h \; k \; l)$ and energy transfer ΔE is much smaller for TOF spectrometers. This circumstance is compensated by the simultaneous detection of events in a large volume in reciprocal space and a wide range in momentum transfer. For two-dimensional systems this fact is of great advantage: Without magnetic correlations along the c-axis the inelastic signal is not modulated along l
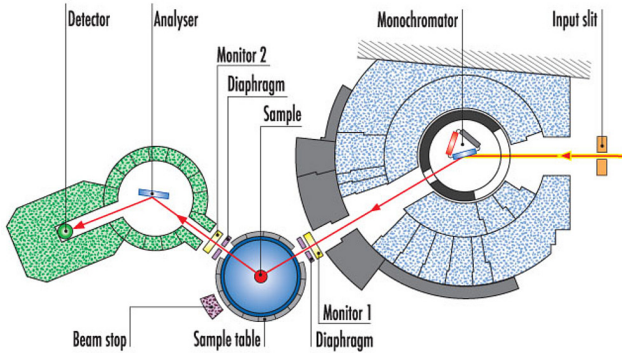
Figure 4.4: IN8 [10, 11] instrument layout. (figure taken from website [10])

but only decays with the magnetic form factor. This allows integration along the l-axis for higher statistics. For quasi-tetragonal systems with small orthorhombicity the symmetry of the lattice can be capitalized on by folding equivalent points in reciprocal space onto each other ($\bar{Q}_i \rightarrow Q_i$, for all components h, k, and l), which can improve the statistics significantly.

On TAS the beam needs to be filtered to reduce higher order contaminants passing the analyzer by placing materials into the neutron beam path, that is transparent for neutrons of a certain energy, only. For thermal TAS blocks of polycrystalline graphite (PG) are used, while cold TAS instruments usually use beryllium filters. As TOF instruments discriminate energy transfer in the time domain they do not require filter components.

Comparing the intensity of elastic and inelastic scattering events, the difference can be several orders of magnitude. In triple axis setups highly sensitive detectors can be protected by placing absorbing sheets of acrylic glass into the beam path when investigating intense elastic scattering channels. This allows operation in a suitable intensity range that does not saturate the detector or

its electronics. Since time-of-flight spectrometers record the full spectrum for each neutron pulse, switching moderation for elastic and inelastic signal is not feasible. This can lead to saturation of the detector or detector electronics, which results in measurement artifacts in the form of intensity carried over from the elastic into inelastic channels.

Polarized neutron scattering

Polarized inelastic neutron scattering makes it possible to separate magnetic from nuclear or background scattering, exploiting the fact that only magnetic scattering events involve a neutron spin-flip. By preparing the initial spin state of the neutron beam and comparing it to the final spin state spin flips can be detected. This requires the use of a polarizer and analyzer element before and after the sample position. Both, polarizer and analyzer, are designed to only allow neutrons with a defined spin direction to pass. They are typically based on a FM single crystal (Heusler alloy), or an engineered multilayer super-mirror. The spin state between polarizer and analyzer is carefully controlled by guide fields to prevent de-polarization by stray fields or the Earth magnetic field.

Experiments involving polarized neutrons are usually carried out at indirect spectrometers that provide the needed neutron flux and allow incorporation of analyzers into their instrumental layout[1]. Analyzers or polarizers never achieve 100 % efficiency. To take this into account, the efficiency is quantified by the flipping ratio of the number of spin-*up* versus spin-*down* neutrons.

The *xyz difference* method for polarized neutron scattering

Neutrons only interact with magnetic moments or spin fluctuations perpendicular to the scattering vector, which is described by the polarization factor $P(\boldsymbol{Q}_\alpha \boldsymbol{Q}_\beta)$ introduced in equation (4.9).

---

[1]There are efforts to develop area analyzers underway (IN20 [8, 9], ILL) that use polarized ^{3}He atoms to absorb neutrons with anti-parallel spin. However, ^{3}He loses its polarization during operation making handling of such devices difficult.

By manipulating the direction of the neutron's spin at the sample location, single scattering channels can be explored. In contrast to magnetic scattering, neutrons scattered in a nuclear scattering event will preserve their spin-state and are only observed in the *non-spin-flip* (nsf) channels.

The calculations for the double cross sections of the single channels is given in [125, 126]. Here, we present an adaptation that captures the all effects needed to describe our experiment.

As experimental reference frame, we orient ourselves by the scattering vector; the axis parallel to it we denote as x, the perpendicular one that lies in the scattering plane as y, and the vertical axis as z.

The magnetic double differential cross section is defined as [125]:

$$\left(\frac{\partial^2 \sigma}{\partial \Omega \partial E_f}\right)^j_{s_i s_f} = \left(\frac{m_n}{2\pi\hbar^2}\right)^2 \frac{k_f}{k_i} (\gamma_n \mu_n)^2 \Gamma^j_{s_i s_f}(\boldsymbol{R}, \omega) \qquad (4.10)$$

Here, i denotes the x, y, or z scattering channel, while s and s' denote if the spin state. The initial and final moment of the neutron is given by k_i and k_f, respectively, and $\gamma_n \mu_n$ is the product of the gyromagnetic moment of the neutron with its magnetic moment. The symbol $\Gamma^j_{s_i s_f}(\boldsymbol{R}, \omega)$ stands for the scattering intensities associated with the matrix elements $M_{jj}(\boldsymbol{R}, \omega)$, that contribute for the respective channel. Magnetic scattering is characterized by the spin-flip $s_f = \bar{s}_i$ channels (sf channels):

$$\begin{pmatrix} \Gamma^x_{sf}(\boldsymbol{R}, \omega) \\ \Gamma^y_{sf}(\boldsymbol{R}, \omega) \\ \Gamma^z_{sf}(\boldsymbol{R}, \omega) \end{pmatrix} = \begin{pmatrix} 0 & 1 & 1 \\ 0 & 0 & 1 \\ 0 & 1 & 0 \end{pmatrix} \begin{pmatrix} |M_{xx}(\boldsymbol{R}, \omega)|^2 \\ |M_{yy}(\boldsymbol{R}, \omega)|^2 \\ |M_{zz}(\boldsymbol{R}, \omega)|^2 \end{pmatrix} \qquad (4.11)$$

.

Of course, the actual measured intensities are offset by non-magnetic background. By taking a combination of differences the background can be eliminated altogether:

$$\begin{pmatrix} |M_\perp(\boldsymbol{R}, \omega)|^2 \\ |M_{yy}(\boldsymbol{R}, \omega)|^2 \\ |M_{zz}(\boldsymbol{R}, \omega)|^2 \end{pmatrix} = \begin{pmatrix} 2 & -1 & -1 \\ 1 & 0 & -1 \\ 1 & -1 & 0 \end{pmatrix} \begin{pmatrix} \Gamma^x_{sf}(\boldsymbol{R}, \omega) \\ \Gamma^y_{sf}(\boldsymbol{R}, \omega) \\ \Gamma^z_{sf}(\boldsymbol{R}, \omega) \end{pmatrix} \qquad (4.12)$$

Note that we concentrate on the quantity $|M_\perp|^2 = |M_{yy} + M_{zz}|^2$ instead of M_{xx} since the orientation factor suppresses any scattering on magnetic excitations parallel to $\boldsymbol{Q}$.

To extract information about the system in terms of the crystallographic frame, these quantities need to be transformed. For a system oriented in the (H0L) scattering geometry, the magnetic moments along the a, b, and c axis of the crystal contribute as follows:

$$\begin{pmatrix} |M_\perp|^2 \\ |M_{yy}|^2 \\ |M_{zz}|^2 \end{pmatrix} = \begin{pmatrix} \sin(\alpha) & 1 & \cos(\alpha) \\ \sin(\alpha) & 0 & \cos(\alpha) \\ 0 & 1 & 0 \end{pmatrix}_{(H0L)} \begin{pmatrix} |M_a|^2 \\ |M_b|^2 \\ |M_c|^2 \end{pmatrix} \quad (4.13)$$

where α is the angle between $\boldsymbol{Q}$ vector and the c axis of the crystals. Since $M_{a,b,c}$ are the physically meaningful parameters, above formula needs to be inverted to obtain them.

4.3 Data processing and analysis

Each technique requires a different procedure and thus different tooling. Generally, data processing and analysis is a complex issue, as it usually consists of a multi-stage process involving combining of single scans to improve statistics, re-binning of the measurement grid, exclusion of spurious signal or measurement artifacts, and separation of signal and noise. With the raw signal in hand, the next step is to compare or fit a theoretical model to the data set.

The data obtained from diffraction and scattering experiments has been analyzed by a mix of open software packages as well as self-written code. In general, time-of-flight data was prepared using a *MantidPlot* [127, 128] pipeline adapted for each instrument. The resulting **.nxspe* files were then inspected using *Mslice* from the *DAVE software suite* [129] or analyzed with the *Horace software suite* [130]. We used *spinW* [131] to create and compare linear spin-wave simulations of calcium ruthenate systems with time-of-flight data. In order to refine diffraction patterns for neutron (X-Ray) powder diffraction experiments we used the FullProf [132] (TOPAS [133]) software package. Details on data analysis including the UB matrix formalism used to transform

coordinates between crystal and laboratory frame, xyz polarization analysis, background subtraction, and advanced detector setups are discussed in appendix B.

Rietveld refinement of diffractograms

In order to analyze a diffractogram obtained through elastic neutron scattering, the Q-dependent intensity is compared to a theoretical prediction based on an assumed crystal structure of the sample. Any discrepancies are minimized in an iterative way by changing the lattice parameters and atomic coordinates in a technique called *Rietveld refinement* [134]. Taking into account instrument configuration the technique is able to make statements on lattice parameters, occupation and position of sites, and nuclear as well as magnetic phases. For neutron powder diffraction we used the software *FullProf Suite* [132, 135, 136] which provides tools to perform Rietveld refinements on structural and magnetic phases [137] .

Chapter 5

Spectroscopic signature of excitonic magnetism

CALCIUM RUTHENATE systems host a surprising variety of different and peculiar phenomena which have been under ongoing investigations for several decades by various research groups. Despite this, many details of the magnetic ground state remain unresolved. In order to develop a full description of the magnetic ground state of Ca_2RuO_4, we investigate the dispersion of magnetic excitations in this system as they express the underlying physics.

To this end we have performed extensive INS studies mapping out the reciprocal space relevant for observing magnetic excitations. Measurements on time-of-flight spectrometers give insight into the strength of SOC in the system, and identify that SOC plays a vital role in the magnetic ground state. In order to reconcile the non-trivial nature of SOC and the observed AFM ground state, we introduce an exotic *soft-moment* magnetism. This ground state is formed via condensation of $J_{eff} = 1$ excitations into an antiferromagnetically ordered state. To verify our model we proceeded by confirming the magnetic nature of the previously found excitations with polarized INS, with which we also determined the polarization of each mode. Finally, we concluded our measurements with powder INS measurements for high energy transfer, in which we were able to identify a set of

excitations that agree with our expectations from microscopic theoretical considerations.

5.1   Magnon dispersion of Ca_2RuO_4

In order to investigate magnon spectrum of Ca_2RuO_4, we have performed time-of-flight INS studies. The in-plane transverse magnon was predicted to have a peculiar dispersion with a maximum at the origin (Γ) of the Brillouin zone (BZ) and the global minimum at the magnetic ordering vector[68, 107]. The spectrum is expected to include excitation energies of up to 70 meV, an energy range better suited for TOF spectrometers than TAS.

Time-of-flight INS on Ca_2RuO_4

In order to acquire experimental data in this region, we turned to time-of-flight INS measurements. The time-of-flight experiments were performed on ≈ 150 coaligned single crystals with a mass totaling 1.5 g (see section 3.3). Using the time-of-flight spectrometer ARCS [1, 2] we obtained the full dispersion of the magnetic excitations. Comparing the intensity ratios between different Brillouin zones while taking the polarization factor into account, we can distinguish two magnon modes and are able to determine their polarization. The main feature is a strong spinwave, and we expect its polarization to be along the a axis, as only transverse spinwaves are expected to show such strong intensity. It disperses from a spin-gap of 15 meV at $(1, 0, l)$ to its maximum at $(0, 0, l)$ (45 meV). Furthermore, we can distinguish the out-of-plane c polarized transverse mode in figure 5.2 that is expected in structurally distorted systems and note that it is considerably less intense.

Phenomenological Model

With the knowledge of the shape of the dispersion we can discuss phenomenological models for candidates describing the *quasi two-dimensional* magnetism of the system. We compare the dispersion to predictions from an isotropic Heisenberg model, that is characterized by its nearest neighbor exchange coupling $\mathfrak{J} \approx W/2z$
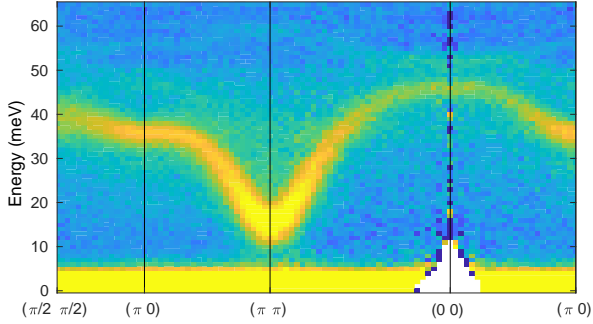
(a) *symmetrized ARCS [1, 2] data*
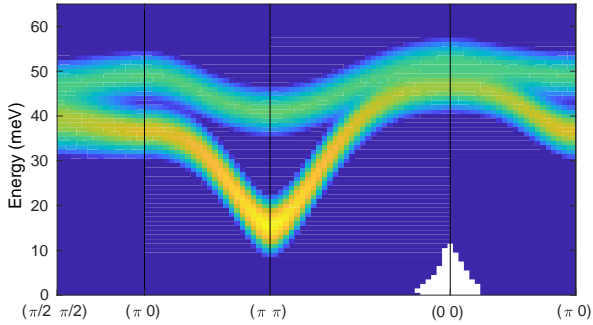
(b) *fitted T and L mode after equation* (5.8)

Figure 5.1: Comparison between experimental data (*left*) taken at ARCS [1, 2] and calculated dispersion with the following optimized parameters: $\mathfrak{J} = 5.80$ meV, $\alpha = 0.150$, $E = 22.75$ meV, $\epsilon = 4.50$ meV, and $A = 1.25$ meV.

which in turn is determined by the magnon bandwidth W and the coordination number z (here $z = 4$):

$$H_{\mathrm{H}} = \mathfrak{J} \sum_{\langle i,j \rangle} \widetilde{\boldsymbol{S}}_i \widetilde{\boldsymbol{S}}_j \tag{5.1}$$

(a) 15 meV   (b) 20 meV   (c) 25 meV   (d) 30 meV

(e) 35 meV   (f) 40 meV   (g) 45 meV   (h) 50 meV
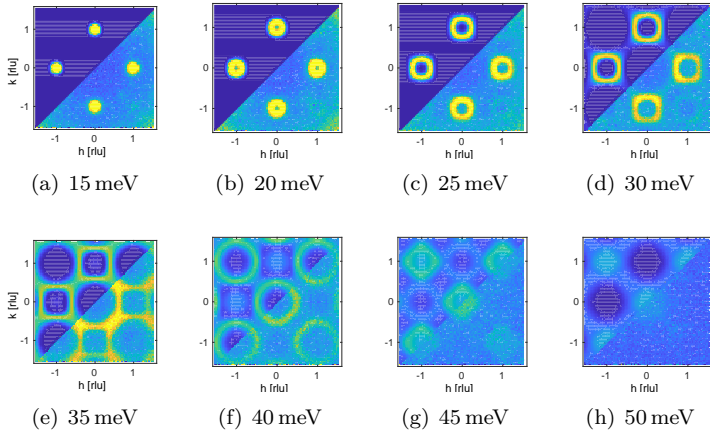
Figure 5.2: *upper left triangles*: calculation of mixing L and T modes. *lower right triangles*; symmetrized experimental data obtained with ARCS [1, 2]. The main T mode is the most prominent feature. At low energies (*upper row*) the T' mode is visible at $(1\ -1)$ (or equivalent), although it is suppressed at $(0\ 0)$ where $\boldsymbol{Q}$ is parallel to the polarization direction.

The isotropic Heisenberg model predicts a spinwave that has a minimum both at the magnetic zone center and the origin $(0\ 0)$ and is unable to explain the observed dispersion. Another simple model is the XY model, in which the exchange interaction acts only on the in-plane components of the spin:

$$H_{\mathrm{XY}} = \mathfrak{J} \sum_{\langle i,j \rangle} \widetilde{\boldsymbol{S}}_i \widetilde{\boldsymbol{S}}_j - \widetilde{S}_i^z \widetilde{S}_j^z \qquad (5.2)$$

In this scenario two spinwaves are expected: an intense magnon mode with a minimum at the magnetic zone center and a maximum at the origin, which indeed replicate the experimental data; and an intense folded mode due to the lattice distortions. While such a second mode is observed, the intensity of the experimental data is so weak that a pure XY-like model is unlikely. Here, we take into account the mode's c-polarization and the neutron polarization factor, that suppresses the excitation near the Γ point

around (0 0 L).

We turn to a rather general form of the Hamiltonian, which permits to continuously tune its character via the parameter α from Heisenberg-like ($\alpha = 0$) to XY-like ($\alpha = 1$). We supplement it by single ion anisotropy terms that can account for tetragonal and orthorhombic distortions of the cubic symmetry of the system, expressed by the parameters E and ϵ, respectively.

$$H = \mathfrak{J} \sum_{\langle i,j \rangle} \left(\widetilde{\boldsymbol{S}}_i \widetilde{\boldsymbol{S}}_j - \alpha \widetilde{S}_i^z \widetilde{S}_j^z \right) + E \sum_i \widetilde{S}_i^{z\,2} + \epsilon \sum_i \widetilde{S}_i^{x\,2} \qquad (5.3)$$
$$\mp A \sum_{\langle i,j \rangle} \left(\widetilde{S}_i^x \widetilde{S}_j^y + \widetilde{S}_i^y \widetilde{S}_j^x \right)$$

A further term, the pseudo-dipolar exchange interaction A affects the dispersion at the magnetic zone boundary and is included to allow a better fit of the experimental data. With this phenomenological (pseudo-)spin Hamiltonian we are able to qualitatively reproduce the experimental magnon dispersion, which we show in figures 5.1b and 5.2. We find however, that the maximum of the dispersion at the Γ point is only achieved for very large values for E of $\approx 25\,\mathrm{meV}$, dominating all other energy scales by far. This is a signature of active and strong SOC in the system, which consequently can not be described by a spin Heisenberg model [33].

5.2 Excitonic soft-moment magnetism

To take the strong SOC into account, we consider a system in which spin states S couple with the orbital momentum states L_{eff}. Recently, such a model has been proposed by Khaliullin. We briefly introduce and discuss this so-called excitonic magnetism, and refer the reader for a detailed theoretical discussion to [42, 68, 107].

First, the splitting of the t_{2g} levels caused by the SOC is considered. Under the assumption that strong SOC renders S and L_{eff} bad quantum numbers, the system is best described by the effective total angular momentum $J_{\mathrm{eff}} = L_{\mathrm{eff}} + S$. In the case of Ca_2RuO_4 ($S = 1$ and $L_{\mathrm{eff}} = 1$), we find possible values of 0,

1 and 2 for J_{eff}. The groundstate is the $J_{\text{eff}} = 0$ singlet, which is non-magnetic. The next higher excited state is the $J_{\text{eff}} = 1$ triplet, separated from the singlet by an excitation energy E that is equal to the SOC parameter λ, which has been estimated to be in the range of $\lambda \approx 50\,\text{meV}$ to $100\,\text{meV}$. This leads to *singlet-triplet* physics and is formally similar to description of dimerized quantum magnets; in the present case, however, the phenomenon is realized on a single ionic site.

The tetragonal compression δ of the cubic CF further splits the degenerate triplet state into a singlet T_z and a doublet T_x & T_y as it reduces the energy cost E needed to create an excitation. The situation is made clear in figure 5.3 where the energy needed to excite the T_x boson from the singlet state is plotted as a function of the tetragonal compression. When δ becomes so large
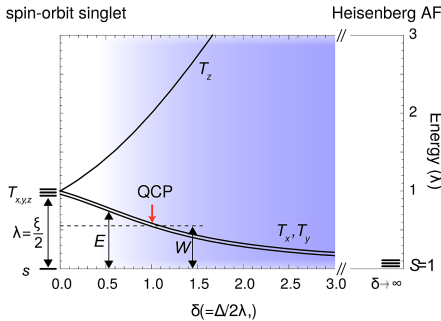
Figure 5.3: Influence of the tetragonal compression of the RuO$_6$ octahedra on the $J_{\text{eff}} = 1$ levels. Figure is taken from [42].

that E equals the bandwidth $W = 2z\mathfrak{J}$ a quantum phase transition occurs where inter-ionic superexchange interaction allows condensation into the lowest triplet state. As a consequence, the system's net magnetization is non-zero and takes the form [68, 107].

$$M = 2\sqrt{6\rho(1-\rho)}\mu_B \qquad (5.4)$$

where $\rho = 1/2 - 1/2\tau$ is the condensate density, $\tau = \mathfrak{J}/\mathfrak{J}_c$ a measure of the vicinity of the system to the quantum critical point (QCP).

Magnetic excitations

The fluctuations of the condensate density result in the existence of a soft amplitude (Higgs) mode that remains intense even deep in the magnetic phase far from the magnetic ordering temperature T_N, setting this soft-moment mode apart from conventional longitudinal modulations. Since the Higgs mode is a result of the transitions between the singlet and triplet states, the linear spin-wave approach needs to be extended to include such transitions [68, 138, 139]. For a rigorous treatment of the microscopic Hamiltonian and application to the Ca_2RuO_4 system in order to calculate its spin-wave spectrum we refer to [68, 107]. We reproduce the dispersion relations obtained in reference [42] and will optimize the relevant parameters in order to reproduce our experimental data:

$$\omega_{L\boldsymbol{Q}} = W\sqrt{1 + \frac{\gamma_{\boldsymbol{Q}}}{\tau^2}} \tag{5.5}$$

$$\omega_{T\boldsymbol{Q}} = \sqrt{a_{\boldsymbol{Q}}b_{\boldsymbol{Q}}} \tag{5.6}$$

$$\omega_{T'\boldsymbol{Q}} = \omega_{T\tilde{\boldsymbol{Q}}}, \quad \text{with } \tilde{\boldsymbol{Q}} = \boldsymbol{Q} + (\pi, \pi) \tag{5.7}$$

$$\omega_{1,2\boldsymbol{Q}}^2 = \frac{\omega_{L\boldsymbol{Q}}^2 + \omega_{T\boldsymbol{Q}}^2}{2} \pm \sqrt{\left(\frac{\omega_{L\boldsymbol{Q}}^2 + \omega_{T\boldsymbol{Q}}^2}{2}\right)^2 + c_{\boldsymbol{Q}}^2} \tag{5.8}$$

where we used the condensate density $\tau = 8\Im/E$, $\gamma_{\boldsymbol{Q}} = 1/2(\cos q_x + \cos q_y)$, and the auxiliary quantities $a_{\boldsymbol{Q}}$, $b_{\boldsymbol{Q}}$, and $c_{\boldsymbol{Q}}$:

$$a_{\boldsymbol{Q}} = \frac{1}{2}W(1 + \tau^{-1})(1 + \gamma_{\boldsymbol{Q}}) + \epsilon \tag{5.9}$$

$$b_{\boldsymbol{Q}} = \frac{1}{2}W(1 + \tau^{-1})\left(1 - \frac{\tau - 1}{\tau + 1}(1 - \alpha)\gamma_{\boldsymbol{Q}}\right) + \epsilon \tag{5.10}$$

$$c_{\boldsymbol{Q}} = W^3 b_{\boldsymbol{Q}} \left(A/2J\tau\right)^2 (\cos q_x - \cos q_y)^2 \tag{5.11}$$

These dispersion relations depend on the parameters introduced by equation (5.3) only and makes mapping between the models possible. In particular, the tetragonal single ion anisotropy E correlates to the effective level splitting between the singlet and the lowest triplet state and is determined by the tetragonal

compression δ of the system:

$$E = \zeta/2 \left(\frac{\sqrt{2}}{\beta + \sqrt{1 + \beta^2}} - \frac{1}{\delta + \sqrt{1 + \delta^2}} \right) \qquad (5.12)$$

where $\beta = 1/\sqrt{2}(\delta - 1/2)$.

Transverse magnon excitations

With the dispersion relations in hand we optimize the T mode parameters to reflect the experimental data, and then calculate the spectrum of all three magnon modes T, T', and L. For an easy comparison between experiment and these theoretical calculations we placed the symmetrized data and the optimized model side by side (figures 5.1 and 5.2). From these figures we

Sr-content	J	α	E	ϵ	A
$x = 0.00$	$5.80\,\text{meV}$	0.15	$22.75\,\text{meV}$	$4.50\,\text{meV}$	$1.25\,\text{meV}$

Table 5.1: Final optimized parameters for simulated spinwave spectrum of Ca$_2$RuO$_4$.

find an excellent agreement between theory and experiment for the T and T' modes. In order to verify the magnetic nature as well as the polarization of the L mode, we turn to polarized INS that can separate nuclear from magnetic scattering channels.

Longitudinal magnon excitations

As seen in the previous section, the model of excitonic magnetism predicts a longitudinal mode L in addition to the two transverse magnon modes T and T' that are expected from the standard spin–wave approach. This amplitude mode arises from condensate fluctuations, and is thus a hallmark feature of the soft-magnetism systems. Investigating the experimental TOF dispersion spectrum in more detail, we observe hints of an additional, third magnon mode on the edges of the magnetic zone center (figure 5.1) that gradually turns into a continuum of intensity at the magnetic ordering vector (figure 5.4).
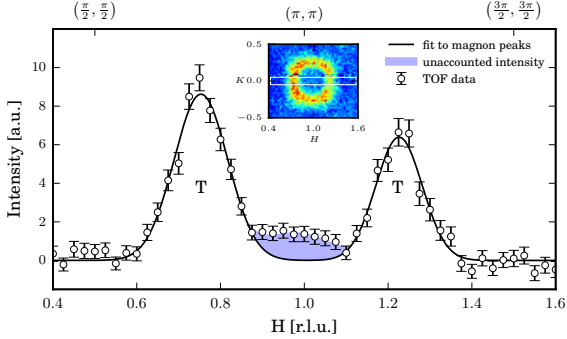
Figure 5.4: Time-of-flight neutron scattering data obtained with ARCS [1, 2]; constant energy cut along the H direction (compare white rectangle in the $HK - map$ of the inset figure. A quadratic background has been subtracted. Interation intervals: $L < 12$ rlu, $25 \, \text{meV} < E < 31 \, \text{meV}$).

Polarized INS on Ca_2RuO_4

Experiments using polarized INS allows distinction between magnetic and nuclear scattering events; the former involve a spin-flip while the latter preserve the spin polarization direction. Combined with manipulation of the neutron spin direction at the sample position xyz-polarization analysis can be performed in order to establish the polarization of magnetic excitations. In this chapter we present the final results of the xyz-polarization analysis; details on the technique have been discussed in section 5.2 and steps to reproduce the final results have been included in appendix C.1.

In order to identify all three magnon modes we focused mainly on only two positions in reciprocal space: The Γ point $(0\ 0\ l)$ and the magnetic ordering vector $(1\ 0\ l)$. In order to optimize the results and confirm the Ru magnetic form factor, we also investigated equivalent positions.
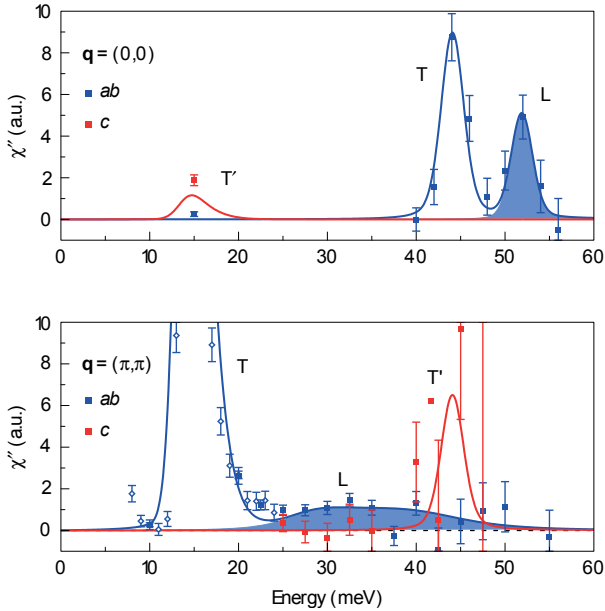
Figure 5.5: Experimental polarized neutron scattering data obtained at the IN20 [8, 9] spectrometer. In all scans L was kept as small as possible while satisfying kinematic restrictions and avoiding contamination from the direct beam. The data has been corrected for the Ru^{1+} magnetic form factor and the crystal orientation has been taken into account. (figure adapted from [42])

Polarization analysis at $(1\ 0\ L)$

At the magnetic zone center a gap of $15\,\text{meV}$ opens. The main inelastic magnetic feature is a transverse mode with moments fluctuating along the hard axis (a), to which we will refer to as T. We observe two more modes, which are clearly separated in energy (Figure 5.5, plot on the left). The polarization analysis of the high energetic feature around $48\,\text{meV}$ indicates a transverse out-of-plane polarization along the c axis T'. With the two transverse modes accounted for the remaining mode is expected to be of longitudinal character, which is supported by the polarization analysis (L).

Polarization analysis at $(0\ 0\ L)$

At the Γ-point two magnetic modes are observed. They are well separated in energy with the more intense mode corresponding to the in-plane transverse mode T centered around 44 meV. As predicted in [107] we observe a second mode compatible with a longitudinal magnetic excitation L at 53 meV.

Since the in-plane component of $\boldsymbol{Q}$ is negligible, the T' mode is suppressed at $(0\ 0\ L)$. In order to observe the T' mode, we investigate $\boldsymbol{Q} = (2\ 0\ 0.4)$ where a large in-plane component allows detection of fluctuations along the c-axis. Indeed, we observe a magnetic peak at $E = 15$ meV with corresponding polarization direction.

Vicinity to the quantum critical point

Since Ca_2RuO_4 is clearly in an AFM state with a magnetic moment of $M = 1.3\mu_B$, the system is positioned on the right side of the QCP shown in 5.3. In this regime the energy of the T_z level is comparable to the $J_{\text{eff}} = 2$ states and thus negligible.
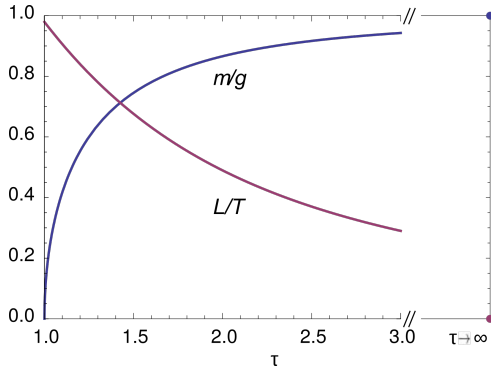
Figure 5.6: The intensity of the intensity ratio of transverse and longitudinal modes that is minimized as the system moves further from the QCP and deeper into the magnetic phase. At the same time, the staggered magnetic moment saturates. (figure adapted from [42])

The vicinity of to the QCP is given by $\tau = \mathfrak{J}/\mathfrak{J}_{\text{cr}} = {}^{8\mathfrak{W}}/_{2zE}$ and thus depends on the bandwidth $\mathfrak{W}$ and on the tetragonal

compression δ that is encoded in E. From our fitted spin-wave dispersion we can extract $\tau \approx 2.2$. A different way to determine τ is to compare the intensity of the L versus the T mode (figure 5.6). Here, the intensity of the transverse T mode gets stronger as the staggered magnetic moment saturates, while the amplitude fluctuations are strongest in the vicinity of the QCP. While this determination is associated with rather large errors as the intensity ratio of 0.55 ± 0.11 can only be approximated from the polarized INS data, we find similar value of $\tau \approx 1.8$.

Decay of the Higgs Mode

Since the number of triplons is not conserved, the Higgs mode itself is not protected and may decay. Our INS measurements show that the amplitude mode L is well-defined around the Γ point only, where it is kinematically restricted from decay into two Goldstone modes. Near the magnetic zone center $\boldsymbol{Q} = (\pi, \pi)$ it can decay into two Goldstone modes, represented by transverse T magnons. In our polarized neutron scattering studies this is observed as a broad intensity continuum of magnetic signal in the range 20 meV to 50 meV, which is the result of the mixing between the T and L modes. Our calculations [42] of the corresponding matrix elements result in a model curve that corresponds very well with the observed continuum intensity (figure 5.5).

The response of an amplitude mode depends on the symmetry of the probe used to investigate as well as on the dimensionality of the system [140]. Considering a two-dimensional system, the intensity of the scalar susceptibility increases with the characteristic ω^3, whereas neutrons, which probe the longitudinal susceptibility, will detect an intensity proportional to ω^{-1}. The latter leads to the *infrared singularity*, where the signal of the amplitude (Higgs) mode is indiscernible from the transverse (Goldstone) modes. In this context Ca_2RuO_4 constitutes a unique system, as all its orthorhombic crystal distortions render all magnon modes gapped and well separated. As a result, we observe a *pile up* of intensity at twice the Goldstone mode's gap energy around 30 meV.

5.3 Discussion

In order to investigate the role of SOC in $4d$ transition metal oxides, we performed neutron spectroscopy studies to observe and map all magnon modes in Ca_2RuO_4. In our initial TOF measurements we were able to gather comprehensive data covering the complete first magnetic Brillouin zone. The technique proved to work exceedingly well suitable for this compound: due to the two-dimensional nature of the magnetic coupling the spin-waves are non-dispersive along the reciprocal l axis, allowing integration of the data set to increase the signal-to-noise ratio considerably. With this spectrum in hand, we are able to unambiguously identify two transverse modes: an a-polarized magnon is clearly visible, a c-polarized folded mode is only visible in higher Brillouin zones due to the polarization factor. From their dispersion we can immediately deduce strong magnetic anisotropies introduced by lattice distortions: All of the magnetic spinwaves are massive; the gap at the magnetic ordering vector is mainly determined by the orthorhombicity of the system, while the maximum at $(0\ 0\ l)$ is indicative of the tetragonal compression dominating all other terms in the phenomenological Hamiltonian. Here, single ion anisotropies express implicitly the coupling between orbital and spin degrees of freedom. From the inelastic magnetic excitations observed in this study we conclude that the SOC is active and rather strong, in accordance to previous XAS experiments [43]. This renders a spin-only model inadequate, as SOC can not be treated perturbatively in such a situation [33]. Consequently, we consider coupled spin and orbital angular moments. The $4d^4$ electron configuration is confined to the t_{2g} sub-shell, resulting in a low-spin $S = 1$ state with an effective orbital momentum of $L_{eff} = 1$. These moments couple to effective total orbital momentum states $J_{eff} = S + L_{eff}$, where $J_{eff} = 0$ is the singlet groundstate of the system in the absence of exchange interactions.

Since this proposed model accounts for the key parameters of Ca_2RuO_4, we follow up to identify further experimental evidence for the system. The hallmark feature of the *excitonic magnetism*, is a soft-moment amplitude mode. In contrast to more conventional amplitude modes that are intense in the vicinity of the ordering temperature only, the soft-moment amplitude is observ-

able across the whole temperature range of the magnetic phase.

Using polarized inelastic neutron scattering we were able to determine the polarization of all modes including an intense longitudinal mode that carries the amplitude oscillation of the magnetic moment. i.e. the so-called *Higgs* mode. Close to the zone boundary a sharp peak attributable to this mode is observed, which evolves into a broad continuum in the vicinity of the magnetic zone center indicative of a coupling between the longitudinal mode and the transverse modes. We attribute this aspect to the decay of the Higgs amplitude mode into two Goldstone magnons, a process expected for solid state systems. Usually however, Goldstone modes are not gapped and the decay process as well as the amplitude mode is obscured by the large intensity of the Goldstone modes. The strong orthorhombic lattice distortions in Ca_2RuO_4 lead to massive Goldstone modes, causing a pile-up of longitudinal intensity at an energy transfer that correspond to twice the gap energy. The resulting protection from the infrared singularity allows us to investigate the longitudinal susceptibility using INS and polarized INS experiments near the magnetic zone center. Furthermore, the process is suppressed near the magnetic zone boundary, as the decay process respects momentum conservation which can not be satisfied far from (π, π).

Having established the amplitude mode, we explore further implications of the model of excitonic magnetism for Ca_2RuO_4. From the strength of the longitudinal mode we can infer the vicinity to the QCP: near the QCP the condensate density is very low which allows very large fluctuations of the magnetic moment, whereas for large condensate densities the magnetic moment is close to saturation. Comparing the ratio of intensities of the transverse T and the longitudinal L modes, we find that the system is rather close to the QCP (compare figure 5.6 with the system's specific value $\tau = 1.8$).

This investigation shows the *importance of unquenched SOC* present in Ca_2RuO_4 and that any theoretical treatment needs to consider the effective total orbital momentum J_{eff}, especially in the regime between negligible weak and strong SOC. The resulting singlet-triplet model leads to novel physics, that is similarly found in a number of investigations, such as the dimerized quantum magnet system $TlCuCl_3$ [141–143]. While the physical

origin is quite different for all these systems, they all share a similar level structure with a singlet groundstate and strong enough exchange interaction that allows condensation into a magnetic state. This in turn allows quantum fluctuations and oscillations of the moment size leading to an intense amplitude mode.

An interesting aspect is that the *criticality* of these systems may be tuned with an external parameter. In the case of the dimerized quantum magnet system, magnetic fields drive the Zeeman splitting while the exchange interaction is unchanged, which affects the condensate density. In our Ca_2RuO_4 system, the spin-orbit level splitting is sensitive to lattice distortions; in particular, tetragonal compression splits the $J_{\text{eff}} = 1$ triplet into a doublet favored and a singlet penalized by the distortion. There are many ways which influence the tetragonal compression of a system, including external pressure in the form of isotropic or uniaxial pressure, or chemical pressure exerted by chemical substitution of the Ca cations by for larger Sr cations. In order to change the criticality of the system we have pursued the latter approach and report on our findings in the next chapter.

Chapter 6

$Ca_{2-x}Sr_xRuO_4$: Tuning the condensate density

$\mathbf{L}$ ATTICE DISTORTIONS play a major role in the energy hierarchy of perovskite-like ruthenates. Especially the insulating AFM phase is sensitive to tetragonal compression, which influences the spin-orbit interaction strength, and mis-orientation of the RuO_6 octahedra, that reduce the bandwidth $\mathfrak{W}$. By controlling $U/\mathfrak{W}$ through tetragonal compression [68, 107] via chemical doping [88], the system's the energy hierarchy can be influenced. In order to tune criticality we performed chemical substitution of the Ca^{2+} ions with isovalent, albeit larger Sr^{2+} ions. There exists an extensive host of literature for the whole $Ca_{2-x}Sr_xRuO_4$ phase diagram [87, 91, 92, 94, 95, 144–151], but only little is known about the magnetic excitations in the AFM regime for doping levels of $x < 0.2$ in $Ca_{2-x}Sr_xRuO_4$. To investigate the evolution of the excitonic magnetism in this regime, we have grown high quality crystals and performed several INS studies.

6.1 Dilute chemical substitution

Chemical substitution in a solid state material is a difficult subject, especially if only dilute doping levels of substitution are desired. One obstacle is the need to achieve homogeneous doping. Furthermore, only limited control can be exercised on the crystal-

lographic sites into which the dopant will be incorporated. While dopants usually replace ions of similar size, they might substitute different elements or sites.

Atomistic simulations are able to determine the energetics for various dopants in Ca_2RuO_4 [152]. In figure 6.1 we reproduce a graph summarizing the effects of divalent dopants into the A sites of A_2RuO_4 with Ca and Sr. It details that from all tested bivalent transition metal (TM) ions the $Ca_{2-x}Sr_xRuO_4$ series is the most stable one. While it is possible to create a charge defect by placing bivalent ions at the Ru^{4+} site, the associated energy cost is at least $\times 20$ higher [152]. Therefore, it is safe to assume Sr ions are incorporated into the A sites only, which we confirm by powder XRD measurements during characterization of the crystals.
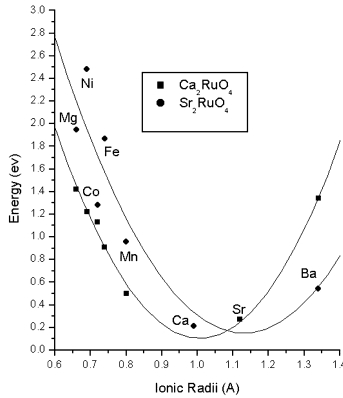
Figure 6.1: Effect of dopants with various ionic radii on the lattice energy. (figure adapted from [152])

Sample properties

The crystals were grown following the same procedure as Ca_2RuO_4. However, the pristine compound's Mott MIT transition temperature is rapidly suppressed from $357\,K$ to cryogenic temperatures and is completely suppressed for $Ca_{1.8}Sr_{0.2}RuO_4$ ($x = 0.2$ or higher) [95, 144, 153]. The MIT is associated with severe struc-

tural changes in the *c*-axis lattice parameter and the crystals usually shatter upon cooling through the transition into small shards. For the sample used in this work T_{MIT} is below room temperature, posing a technical difficulty for experiments conducted at cryogenic temperatures. We were able to mitigate sample degradation to a certain degree by enveloping the crystals in a hard shell that was deposited via Al-evaporation. While this hard shell did not prevent the shattering of the crystals themselves, it fixates the individual shards in space. As a result, we were able to maintain $15\,\%$ to $40\,\%$ of the original crystal mass, with the trade-off of a slightly increased mosaicity and a small additional background from Al-scattering events.

Sample characterization

To investigate the structure and assert phase purity we performed powder X-ray diffraction. At room temperature we are able to observe a change in lattice parameters over the substitution range $x = 0$ to 0.3. The results (visualized in figure 6.2) show the unit cell volume increases with Sr substitution, which indicates that pressure studies might be able to tune the system.
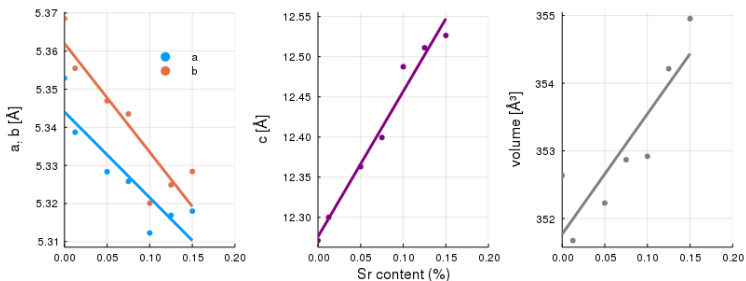
Figure 6.2: Evolution of the lattice parameters with increasing Sr content.The best indication of the relaxation of the crystal structure is the volume of the unit cell, that increases due to the larger ionic radius of Sr.

The reduction of these distortions leads to a more regular structure in which the RuO_6 octahedra are less tilted and rotated. As a result, a change in the intersite superexchange interactions

strength can be expected as the wavefunciton overlap between Ru and in-plane O changes. In order to judge the influence of dilute Sr substitution on the superexchange we need to investigate the tilt and rotations of the RuO_6 octahedra. However, this requires exact knowledge of the atomic positions. The in-house X-ray diffractometers provide only approximate atomic positions for oxygen, and to reach the required temperatures of the ordered phase a cryostat would be needed, further reducing the quality of the measurement. Thus, we rely on the data available from [95], which we reproduce in figure 6.3 for reference. We note that starting with $x = 0.2$ the octahedra start rotating about their c axis, which coincides with a structural phase transition concurrent with a MIT and onset of antiferromagnetism.
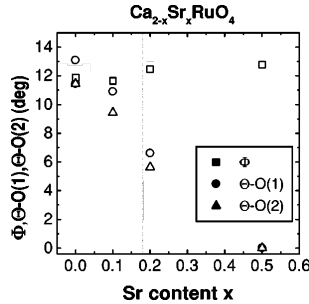
Figure 6.3: Evolution of the tilt and rotation angles of the RuO_6 octahedra. Here, Θ-O(1) and Θ-O(2) correspond to tilt angles, and Φ to the rotation about the c axis at 10 K. (figure adapted from [95])

Further characterization was performed by magnetometry on pulverized single crystals. The transition is not as sharp as in the parent compound, indicating a potentially inhomogeneous distribution of Sr within the sample. However, that the bulk of the sample transitions at the same temperature. For inelastic measurements the batches with the sharpest transitions were selected.

6.2 Inelastic neutron scattering

In order to investigate the evolution of the spinwaves present in the system we first investigated the full dispersion using the ARCS [1, 2] time-of-flight spectrometer. The sample had an original mass of approximately 1.5 g, but degraded considerably during cooling to an effective sample mass of about 350 mg, and we had to compensate the missing sample mass with longer counting times. However, the remaining crystals were held in place and only a small increase of mosaicity compared to other samples was observed. By projecting all equivalent points into a single octant in the h, k-plane we increased the statistics of the data set and were thus able to extract the spinwave dispersion and the relevant parameters to model the experimental data. We performed INS experiments on $Ca_{2-x}Sr_xRuO_4$ with $x = 0.1$ and $x = 0.15$ and focus here on the $Ca_{1.9}Sr_{0.1}RuO_4$ compound, which is located well in the AFM phase.

$Ca_{1.9}Sr_{0.1}RuO_4$

Qualitatively, the dispersion of the main transverse magnon mode is similar to that of the pristine compound Ca_2RuO_4 (figure 5.1), which can be readily seen in figure 6.4. The size of the anisotropy gap as well as the bandwidth slightly shift and we observe changes near the border of the Brillouin zone. From these observations we conclude that the structural distortions influence both superexchange interaction parameters and spin orbit coupling resulting in variations of the single ion anisotropies.

For quantitative statements we consider the phenomenological Hamiltonian introduced in section 5.1 which takes both parameters into account. The expected spinwave dispersion is then compared to the experimental data, which allows determination of each parameter via a least square optimization. Additional TAS measurements were conducted to focus upon certain features of the spinwave dispersion to improve the quality of the model.

Fitting the experimental data with the dispersion relation is challenging because of the rather limited statistics of the data set. We attribute the flat band below 40 meV to sample powder, similar to what we have seen in early TOF measurements on
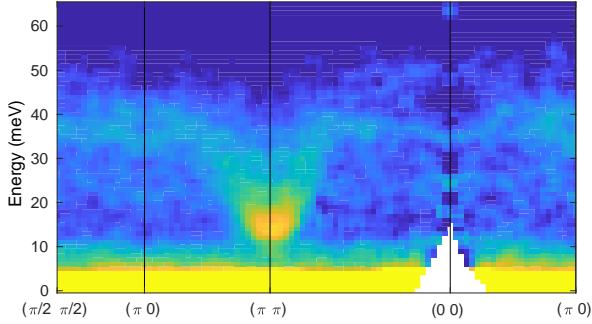
(a) $Ca_{1.9}Sr_{0.1}RuO_4$
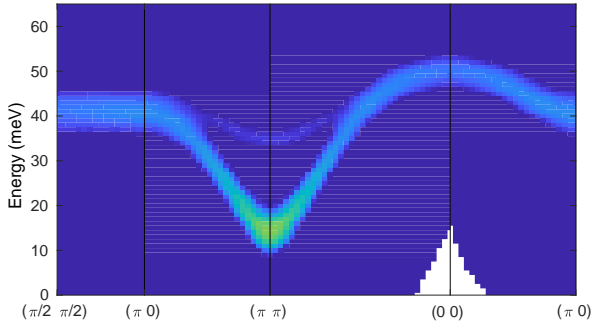
(b) *spinW calculation*

Figure 6.4: Experimental and calculated dispersion, obtained using the ARCS [1, 2] spectrometer. The low quality of the data is a result of the degradation of the single crystals, resulting in an *oriented powder* sample. Misalignment in the $hk0$ plane explain the continuous powder band at 40 meV. The optimized parameters are listed in table 6.1.

Ca_2RuO_4 crystals of lesser quality. Enforcing sensible restrictions we were able to find satisfactory agreement between data and simulation. We observe that the anisotropies and exchange interaction undergo a minor change as the lattice relaxes, but the errors associated with the fitting results do not allow us to make

Sr-content	J	α	E	ϵ	A
$x = 0.00$	5.80 meV	0.15	22.75 meV	4.50 meV	1.25 meV
$x = 0.10$	5.5 meV	0.15	27.00 meV	4.0 meV	–

Table 6.1: TOF data and simulation for x =0.00 and 0.10 and final fitting parameters for simulated spinwave.

solid claims regarding the criticality of the system.

(a) 15 meV   (b) 20 meV   (c) 25 meV   (d) 30 meV

(e) 35 meV   (f) 40 meV   (g) 45 meV   (h) 50 meV
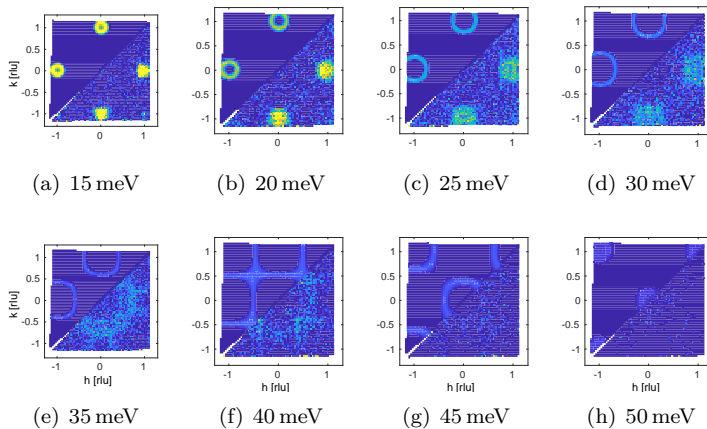
Figure 6.5: TOF data obtained with ARCS [1, 2] and simulation for $Ca_{1.9}Sr_{0.1}RuO_4$. Constant energy maps allow to follow the dispersion in energy, and can give a good impression on the behavior far from the magnetic zone center. The circular feature in panel (e) is due to powder due to the crystal degradation.

6.3 Discussion

By substitution of small Ca ions ($r_{Sr^{2+}} = 1.18\,\text{Å}$[1]) with larger Sr ions ($r_{Ca^{2+}} = 1.00\,\text{Å}$[1]) the strong distortions of Ca_2RuO_4 are lifted; i.e. the tetragonal compression and orthorhombicity of

---

[1]ionic radii for 6-fold coordination after [154]

the crystal lattice is reduced. While the magnetic anisotropies do not necessarily follow the crystallographic distortions, we can certainly expect associated behavior. In order to judge the impact of lattice distortions, we consider the expected consequences of Sr substitution onto the parameters determining the spinwave dispersion.

As the rotations and tilts are reduced, the overlap of the in-plane orbitals is directly influenced. Straightening the in-plane Ru−O−Ru bond angle increases the hybridization between the d_{xy} states of Ru and the $2p$ states of the in-plane oxygen ions (O(1) site). Consequently, we expect an increased electronic bandwidth $\mathfrak{W}$ and increased inter-site hopping rate t [94]. The compression δ of the RuO_6 octahedra is coupled to the size of the unit cell along the c axis and affects the magnetic anisotropy E. As the paramount tuning parameter in the picture of excitonic magnetism, changes in E can lead to profound differences in the dynamical magnetic properties. Indeed, the authors of [107] discuss a second magnetic phase for the regime of small compression δ in which the magnetic moment coaligns with the c axis of the crystal lattice. However, such a phase has been ruled out by early neutron diffraction experiments on $Ca_{1.9}Sr_{0.1}RuO_4$ [95]. The ratio of in-plane Ru−O distances is responsible for the in-plane anisotropy ϵ which gets reduced as the system becomes more regular.

Fitting the dispersion for the transverse in-plane mode to the INS obtained from our Sr substituted samples we are unable to quantify the changes relative to the parent Ca_2RuO_4 due to the low statistics of the data set. With errors of the order of 10 %, we are not able to make definite statements regarding the criticality of the system, but from our fits it seems that the system moves further away from the QCP. From table 6.1 we find differences from the pure to the doped system, albeit the level of dopant concentration does not seem to be of great importance when comparing experimental data for $x = 0.1$ and $x = 0.15$ (not shown). Regrettably, the degradation of the (originally) high-quality crystals due to the structural transition at cryogenic temperatures makes this an extremely challenging system for inelastic neutron scattering studies.

Chapter 7

$Ca_3Ru_2O_7$: Bilayer calcium ruthenate

EXTENDING THE DIMENSIONALITY of Ca_2RuO_4 ($n = 1$) from a purely 2D to a 3D system the properties of the system change profoundly, especially in the magnetically ordered regime.

7.1   INS on $Ca_3Ru_2O_7$

In order to investigate how SOC evolves upon increasing the dimensionality of the system, we performed inelastic neutron scattering on pristine $Ca_3Ru_2O_7$ using the IN8 [10, 11] TAS in the flatcone multi-detector configuration. The flatcone detector allows rapid collection of constant energy maps, which we use to investigate the dispersion in the h,k-scattering plane, expanding on the previous INS study by [155] that studied the dispersion along the h direction only. Following the dispersion to high energy transfers proved to be difficult due to the diminishing signal of the excitations, similarly to what has previously been reported by [155] in $Ca_3Ru_2O_7$ or for the metallic phase of $La_{1.2}Sr_{1.8}Mn_2O_7$[156]. The additional structural correlation between adjacent planes of RuO_4 ions is seen in scattering experiments as a modulation of the signal strength along the l reciprocal axis, expressed by the bilayer structure factor $\cos^2(l/d_L)$. In combination with the magnetic form factor, the bilayer structure factor restricts available

positions in reciprocal space effectively to $l = -5, 0, 5$. Nevertheless, we were able to obtain data up to $22\,\mathrm{meV}$ with a reasonable signal-to-noise ratio. The data was obtained at the IN8 [10, 11] spectrometer with the flatcone multi-detector, which was used to record constant-energy maps in the (h k 0) scattering plane (figure 7.1).
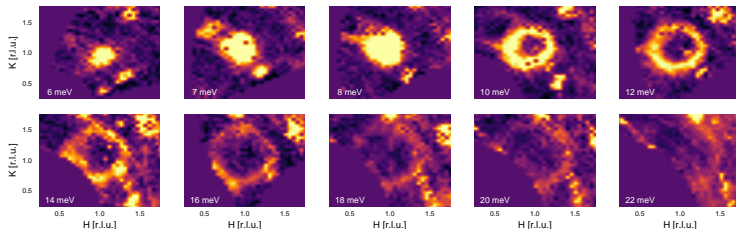
Figure 7.1: Constant energy maps centered at the magnetic zone center (1 1 0) (first row: $6\,\mathrm{meV}$ to $12\,\mathrm{meV}$, second row: $14\,\mathrm{meV}$ to $22\,\mathrm{meV}$), obtained at the IN20 [8, 9] spectrometer using the Flatcone multidetector. Powder background was removed in all data-sets, and the color maps use the same intensity limits.

In order to extract the dispersion, we plot the scattering intensity against the the distance to the magnetic zone center in momentum space. However, an increasing background, the decreasing signal strength, and numerous spurious features make isolation of the magnetic signal difficult.

While the dispersion for energies lower than $14\,\mathrm{meV}$ shows a circular shape in the $(h\ k\ 0)$ scattering plane (*i.e.* the first row of figure 7.1), we find that higher energies might show some anisotropic features expressed by the rectangular shape of the magnon dispersion. Upon closer inspection we find artifacts from strong elastic signals, that were not filtered by the Si analyzers of the flatcone detector. With increasing energy transfer, we observe the artifacts wandering, and obscuring the signal. Upon careful analysis we conclude that the signal itself does not show anisotropies, and thus consider the exchange interaction parameters isotropic.

Since the intensity of the magnon mode at high energies was below the detection threshold for the IN8 [10, 11] setup in the flatcone configuration, we repeated the measurement at PUMA [15,

16] in its standard single detector configuration. We are able to use the bilayer structure factor to our advantage by contrasting scans at q positions corresponding to the maximum ($q_l = 0\,\mathrm{r\,l\,u}$) and the minimum ($q_l = 2.5\,\mathrm{r\,l\,u}$). We also take a reduction by
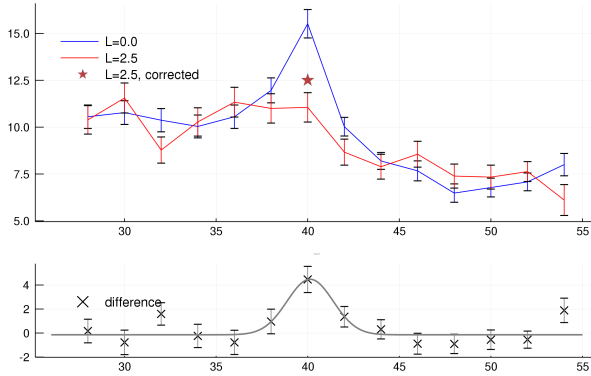
Figure 7.2: INS of Ca$_3$Ru$_2$O$_7$, measured at PUMA [15, 16]

the magnetic structure factor into account: At $q_{3\ 0\ 0} = 3.49\,\text{\AA}^{-1}$ ($q_{3\ 0\ 2.5} = 3.58\,\text{\AA}^{-1}$) the nominal intensity of a magnetic excitation has decayed by 72.9 % (74.5 %), respectively. The gray star symbol in figure 7.2 indicates the relative adjustment of the data with $L = 2.5\,\mathrm{rlu}$, which is negligible. Thus, comparing the intensity at (3 0 0) and (3 0 2.5) allows us to extract an energy of (39.2 meV) for the peak of the magnon.

The above measurement can be combined to extract the dispersion, as has been done in figure 7.3. Here, we present the first scattering study that experimentally determines the bandwidth of the magnon dispersion. The value of 33 meV is in accordance in previous estimates from INS data ([155]).

7.2 INS on Ca$_3$Ru$_2$O$_7$ with applied magnetic field

As the full spin-wave dispersion is difficult to access in Ca$_3$Ru$_2$O$_7$, we further studied the competition between electronic correlations
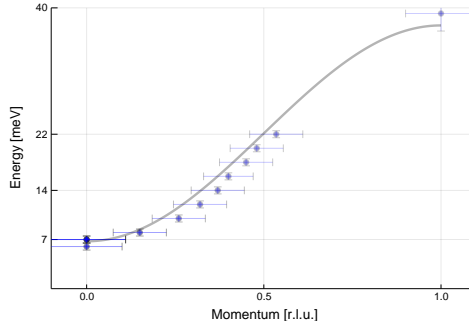
Figure 7.3: The figure combines the data from the INS experiments performed PUMA [15, 16] and IN8 [10, 11]. With the gap and the maximum of the magnon dispersion determined, we are able to extract the bandwidth of 33 meV.

and SOC energies by investigating the evolution of the AFM-a, and AFM-b phases under field, as well as the CMR and FM phases (phase diagram is shown in figure 2.7b). Here, we follow [59] and present the observation of the Zeeman splitting of the doubly degenerate magnon gap excitation under magnetic field in the AFM-b phase. Our twinned sample (ratio roughly 1 : 1) is mounted in the $(h\ 0\ l)/(0\ h\ l)$ scattering orientation. Consequently, the effects of both $B \parallel a$ and $B \parallel b$ will be observed by the bulk INS measurements. In the second situation we expect a split of the magnon doublet, whereas in the first no change is expected. Indeed, upon application of magnetic field we observe a broadening of the gap as well as a strong decrease in intensity. We fit the intensity profile with three Gaussian peaks (see figure 7.4), which were restricted to same volume of the satellite peaks with a constant peak width. Tracking the position of the satellites, we observe a linear shift with increasing magnetic field (see figure inset).

By performing constant energy scans we were able to follow the dispersion up to 12 meV. While the signal remains clearly visible, the distance in reciprocal space between the arms of the three dispersion cones reduces with increasing energy and makes them indistinguishable. In figure 7.5 we compare the dynamic
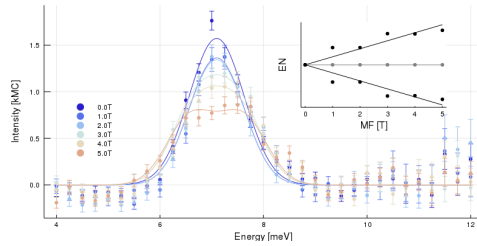
Figure 7.4: Constant-Q scans measured at EIGER [6, 7]. With increasing magnetic field the gap excitation in the $(0\ h\ l)$ domain splits, while the $(h\ 0\ l)$ remains twofold degenerate. *Inset:* the level splitting becomes clearly visible if it peak positions are plotted against the applied magnetic field (black: $(0\ h\ l)$ domain, gray: $(h\ 0\ l)$ domain).

response at ambient field and at 5 T.
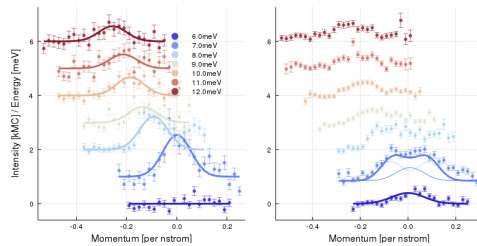
Figure 7.5: Constant-energy scans measured at EIGER [6, 7]. With increasing magnetic field the magnon excitation in the (0HL) domain splits, while the (H0L) remains twofold degenerate. Here the dispersion of the mode under applied field of 0 T and 5 T is compared.

7.3 Discussion

$Ca_3Ru_2O_7$ effectively renders the two-dimensional magnetism more 3D-like by extending the interaction by an out-of-plane coupling between the individual RuO_6 sheets of the bilayer. Comparing the members of the $Ca_{n+1}Ru_nO_{3n+1}$ RP series, a trend towards a metallic phase is observed, where bulk-like $CaRuO_3$ is in a paramagnetic metallic state for all temperatures. We

observe that in the metallic phase SOC is suppressed, and our experimental data supports the description by a spin-only Heisenberg model [155]. Further INS measurements under applied magnetic field show the Zeeman splitting of the twofold degenerate spin-wave. This stands in stark contrast to the pseudospin characteristics of the single layer system, and the FM characters of the in-plane coupling does not allow to follow the evolution of the insulating AFM spin-wave of Ca_2RuO_4 with increasing dimensionality.

Chapter 8

$Ca_3Ru_{2-x}Ti_xO_7$: Tuning Dimensionality

Investigating the $Ca_3Ru_2O_7$ system we found spin-only behavior of the magnetic excitations, which stands in stark contrast to the magnetism found in the single layer Ca_2RuO_4. Our INS experiments support the reasoning that the two-dimensional metallic state of the bilayer compound allows direct exchange interactions and favors ferromagnetism, while it also suppresses the SOC. The discovery of an highly insulating state in $Ca_3Ru_2O_7$ upon minute Ti doping associated with antiferromagnetic spin order [67, 112, 113, 157, 158] is thus exciting news, as it may allow us to follow the evolution of the soft-moment magnetism of Ca_2RuO_4 upon additional out-of-plane coupling. Consequently, we performed INS experiments on self-grown $Ca_3Ru_{2-x}Ti_xO_7$ samples in order to reveal the spin-wave dispersion spectrum of the system.

To investigate the interplay between structure and magnetism across the phase transition at $T_N = T_{MIT} \approx 50\,K$ we grew high quality crystals on which we performed neutron diffraction as well as inelastic neutron scattering experiments.

8.1 Basic Sample characterization

The growth and characterization of our samples is covered in chapter 3. In order to highlight the magnetic behavior we present
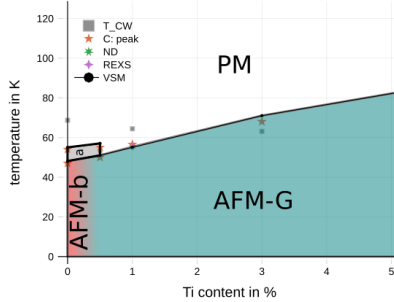
Figure 8.1: Phase Diagram of $Ca_3Ru_{2-x}Ti_xO_7$, where the AFM-a and AFM-b states are 2D metallic and the AFM-G phase is insulating. We have included data from [159] (red brackets).

here a few results from the characterization of the samples as well as the resulting phase diagram (figure 8.1). All samples show a high homogeneity, indicated by the abrupt response of the heat capacity or susceptibility measurements during the phase transitions. We find that the magnetic and electronic transitions occur at very low substitution levels, comparable to the reports of [67], which leads to an updated phase diagram shown in figure 8.1. In particular, we do not observe intermediate transition phase between AFM-b and g-type AFM phases, which might be the results of distribution inhomogeneities of the chemical dopants in the bulk crystals. We attribute those differences to inhomogeneities of the Ti distribution, which may defer uniform phase transitions and introduce intermediate phases.

Sample Growth and Basic Characterization

We have prepared several compounds of $Ca_3Ru_{2-x}Ti_xO_7$ with varying Ti substitution levels, including samples with $x =$ 0.1, 0.2 and 0.6. We asserted phase purity with powder X-ray diffraction at room temperature, the results of which are displayed along with the neutron diffraction data in the next section. The ionic radii of the ions are quite similar ($r_{Ru^{4+}} = 0.620$ Å and $r_{Ti^{4+}} = 0.605$ Å [154]), and at room temperature dilute substitution has a very subtle effect on the lattice parameters. In contrast to the
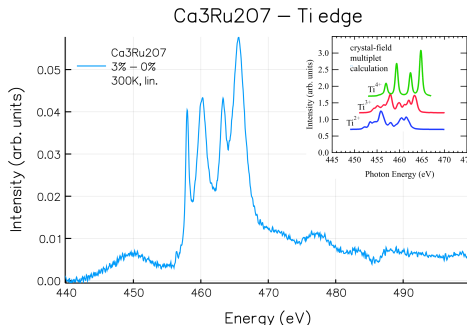
Figure 8.2: X-ray absorption spectroscopy (*total electron yield* mode) performed at the beamline BOREAS [3, 4]. We show the difference between spectra of two samples with $x = 0.02$ and $x = 0$, necessary due to dilute Ti content and the vicinity of the Ru L edge. *Inset*: reference spectra of bi-, tri- and tetravalent Ti (taken from [160]).

Sr^{2+} substitution, the Ti^{4+} ion might be incorporated into the A^{2+} or B^{4+} site, or enter the B-site with a valency different from B^{4+}.

The valency of the Ti cations can be determined by comparing the X-Ray Absorption Spectra of $Ca_3Ru_{2-x}Ti_xO_7$ with calculations for bi-, tri- or tetravalent Ti. From figure 8.2 we conclude that only tetravalent Ti^{4+} ions are present in the compound.

In our heat capacity data we are able to observe two phase transitions in pure $Ca_3Ru_2O_7$ (black curve in figure 8.3a) which correspond to the *AFM-a* and *AFM-b* phases. At the very low doping level of 5 ‰ we still observe two phases, but both shift to slightly higher temperatures. For Ti levels of higher than that we can not resolve the two phases. Instead, the system undergoes the metal-insulator transition at the same temperature it orders magnetically, which becomes obvious if the heat capacity data is compared with the magnetometry data (figure 8.3b).

Surprisingly, the magnetometry reveals a positive *Curie-Weiss* temperature of roughly the same order as the magnetic ordering temperature, indicated by gray squares in figure 8.1. Despite this indication of ferromagnetic behavior, the system orders in an AFM state below the transition temperature T_N.
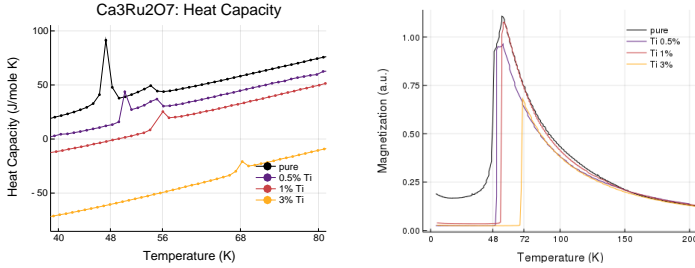
(a) $Ca_3Ru_{2-x}Ti_xO_7$: heat capacity measurements

(b) magnetometry measurements of $Ca_3Ru_{2-x}Ti_xO_7$

8.2 Neutron Powder Diffraction

In all layered ruthenate systems the local environment of the Ru^{4+} ion is determining the details of the magnetic properties. Thus we have performed neutron powder diffraction which allows us to refine the crystal structure and the deformation of the RuO_6 octahedra.

The samples have been obtained by selecting high-quality single crystals of $Ca_3Ru_2O_7$ batches and carefully grinding them to a homogeneous powder using a agate ball mill mortar. Since minute variations of Ti content already introduce large structural changes we can observe a mixture of phases with slightly varying Ti concentrations. As a result, the individual peaks are broadened, and we might observe broadened phase transition due to the bulk-sensitivity of the method. Using these criteria we find that our sample with 1 % Ti seems extraordinarily phase-pure. Thus, we will concentrate our reasoning in later sections on the 1 % compound as it captures all salient features of higher substitution levels.

The neutron diffraction experiments were carried out using several diffractometers: We used SPODI [17, 18] (MLZ, Garching) for high resolution measurements, and E6 [5] (HZB, Berlin) for temperature-dependence measurements. With the high-resolution data we were able to refine the lattice and magnetic structure. With these refined parameters in hand, we then analyzed the temperature dependence of the lattice parameters across

the MIT.

Refinement strategy

To analyze the data sets we used the software *FullProf Suite*[135], which performs a Rietveld refinement [134].

We started with the structural refinement of $Ca_3Ru_{1.98}Ti_{0.02}O_7$ for the minimum and maximum temperature of 5 K and 200 K, respectively. After an initial structural refinement with $\lambda =$1.548 Å we refined the magnetic structure on a data set that was taken with a wavelength of $\lambda =$2.535 Å which allowed a more detailed view on low-*q* features such as the Bragg peaks of the magnetic phase. From symmetry analysis of the lattice space group *Bb21m* using FullProf's BasiReps program we found four possible magnetic structures, of which the *layered AFM-G type* was used for best fitting results. Now, equipped with the refined structural and magnetic phases we iterate the refinement. With the two structural (5 K and 295 K) and the magnetic phase (5 K) we now are able to turn to the high resolution data sets taken at temperatures of 50 K, 60 K and 70 K (SPODI, $\lambda = 1.5481$ Å) and the high intensity data set covering the gaps between 5 K and 50 K. All other neutron diffraction data sets were subsequently fitted using the 1 % phases as a starting point. Corresponding tables summarizing the magnetic phase, the Rietveld refinements, and the obtained parameters are listed in the appendix A.2.

Temperature dependence and Trends

In order to be able to compare to existing literature we have extracted the structure parameters of Ca_2RuO_4, $Ca_3Ru_2O_7$, and $Ca_3Ru_{1.98}Ti_{0.02}O_7$ from the publications [70], [162], and [159][1], respectively. We first turn to the structural aspects that are introduced by substituting Ru for Ti, and note surprising similarities of the substituted compound to the single layered compound Ca_2RuO_4.

While the *a* and *b* lattice parameters of the parent $Ca_3Ru_2O_7$ do change at the phase transitions, the overall change is rather

---

[1]original measurement by Price in an unpublished Diploma thesis [163]
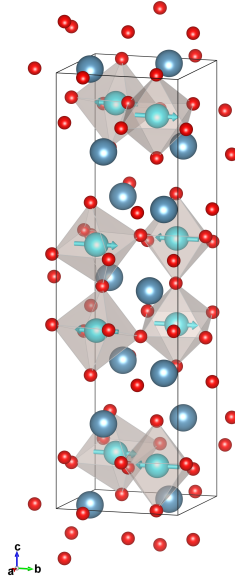
Figure 8.3: Schematic display of the spin orientation in $Ca_3Ru_{2-x}Ti_xO_7$. Created with [161]

small (see figure 8.4). Ti substituted $Ca_3Ru_2O_7$ however shows a distinct change in the b and c lattice parameters, which directly affects the orthorhombicity and the distortions present in the system. The altered crystal structure translates into changes of the crystal field, and while the system maintains its symmetries the local environment of the magnetic cations undergoes modification. These can lead to changes in the energy hierarchy of the system, especially if different forces are competing in the system. The local environment of the Ru^{4+} cation is determined by the 6 coordinated oxygen anions. Here we compare the distortions of the Ti-substituted $Ca_3Ru_{2-x}Ti_xO_7$ with its parent compound ($Ca_3Ru_2O_7$) and the closely related Ca_2RuO_4 to judge the anisotropy changes.
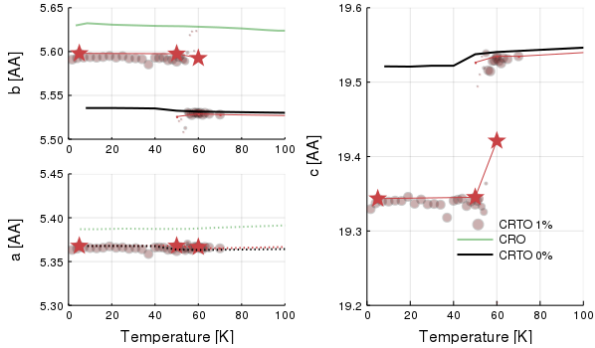
Figure 8.4: *top:* lattice parameters of Ca$_3$Ru$_{1.98}$Ti$_{0.02}$O$_7$.
bottom: orthorhombicity and volume. The marker size corresponds to the relative volume fraction of the hot or cold temperature phase (cutoff: 5 %), high-resulition data (stars) taken at SPODI [17, 18], other data points taken at E6 [5].
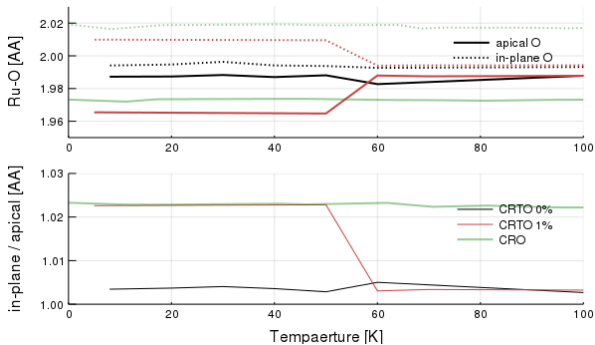
Figure 8.5: We compare the atomic distances between Ru and the apical / in-plane O as well as the resulting tetragonal distortions.

8.3 Magnetic Excitations in Ca$_3$Ru$_{2-x}$Ti$_x$O$_7$

Our diffraction studies show a rather drastic change in the crystal structure of Ca$_3$Ru$_{2-x}$Ti$_x$O$_7$ compared to the parent compound Ca$_3$Ru$_2$O$_7$ and a close relation to the crystal distortions
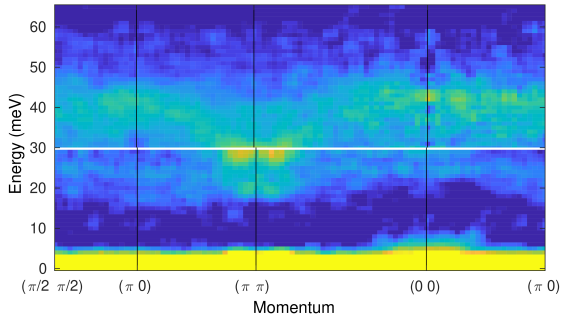
Figure 8.6: INS of $Ca_3Ru_{1.98}Ti_{0.02}O_7$, measured at MERLIN [13, 14].

of Ca_2RuO_4. Combined with the drastic change of the magnetic ordering, we expect an INS spectrum that is distinct from the one of the pure $Ca_3Ru_2O_7$.

Time-of-Flight Measurements

We have performed time-of-flight INS measurements on samples of $Ca_3Ru_{2-x}Ti_xO_7$ with various levels of Ti substitution. In preliminary measurements on the MERLIN [13, 14] spectrometer, we were able to get a picture of magnetic excitation and their dispersion (see figure 8.6). Surprisingly, the observed excitations are very similar to the single-layered Ca_2RuO_4 and—in contrast to its parent compound $Ca_3Ru_2O_7$—do not show any characteristics of ferromagnetism, most notably by the change of the magnetic ordering vector. In addition to the pronounced in-plane transverse magnon a strong, localized signal at the magnetic ordering vector is observed at an energy transfer of 20 meV.

TAS measurements

To investigate the excitations more closely, we additionally performed TAS INS measurements on the 1 % and 3 % $Ca_3Ru_{2-x}Ti_xO_7$ samples (on IN8 [10, 11] and PUMA [15, 16], respectively). Here we focused on the shape of the dispersion of the main magnon mode as well as on the feature at 20 meV

Transverse magnon modes By performing constant energy h-scans we are able to identify the dispersion branches of the main magnon. To verify the magnetic nature of the signal, we subtract the phononic signal taken at 60 K from the signal taken at 5 K and are left with the magnetic signal only. While this approach works reasonably well for energies up to ≈ 55 meV, the distinct structural phases above and below T_N influence the phonon energies. As a consequence, we observe artifacts stemming from the fact that the high-temperature phonon signal is in fact not a good background reference in the magnetic phase.
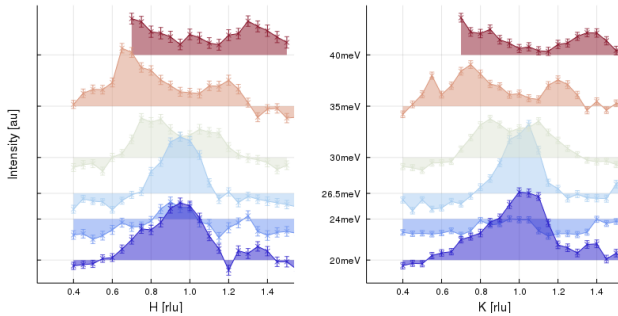
Figure 8.7: Dispersion of the T magnon both in the $(h\ 0\ l)$ (*left*) and in the $(0\ k\ l)$ (*right*) scattering plane observed by temperature difference curves taken at IN8 [10, 11]. Here h-scans at increasing energies are plotted from the bottom to the top with a non-dispersing localized peak at 20 meV and the dispersion T magnon at the spin gap at 26.5 meV, which disperses to high energies.

For higher energies we performed energy scans at various $\boldsymbol{Q}$ points and were able to establish the bandwidth of the system of $W \approx 18.5$ meV.

Twinning Ratio and Polarization analysis For the IN8 [10, 11] beamtime we prepared an array of co-aligned crystals with an improved twinning ratio $h0l : 0kl = 3 : 1$. This sample allowed polarization analysis of the magnon modes. To this end we remounted the sample mid-experiment from the $h0l$ to the $0kl$ scattering plane, and compared the intensities taking the polarization factor into account. Since several crystals detached
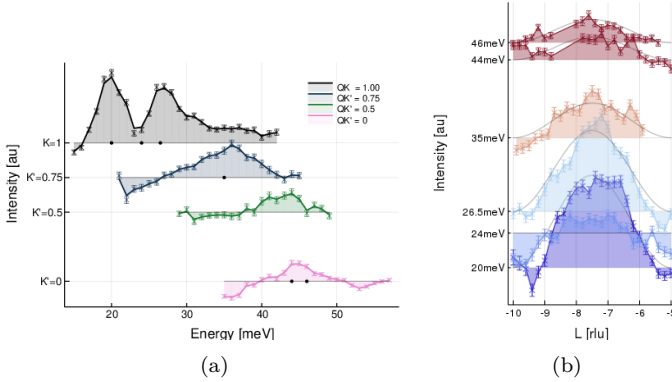
Figure 8.8: *left*: Localized feature at 20 meV for $K = 1$ as well as the dispersion magnon T mode visible in temperature difference curves. In order to distinguish signal form artifacts, we performed *l*-scans at energies indicated by the black dots. *right*: the L-scans show the bilayer modulation with a period of $\Delta l = 5\,\mathrm{r\,l\,u}$. Experimental data obtained at the IN8 [10, 11] spectrometer.

during the remounting of the array, we normalized the intensities by multiplying the *h0l* data set with a factor of $\times 1.535$ (see figure 8.10).

In figure 8.9 we compare the intensities of the energy scans taken at the magnetic zone center but in different Brillouin zones, and for both array orientations. From the scans it is clear the dispersing mode with an energy gap of 26.5 meV is a transverse mode polarized in the *a* direction (*T* mode). For convenience we plot the polarization factor for *a*- and *c*-polarized excitations as an overlay curve in figure 8.9, while respecting the domain ratio and the magnetic form factor.

In the first set of scans (*0kl* scattering plane) we compare energy scans between different Brillouin zones. We expect a suppressed *c* polarized mode for scans with large *l* component while the *a* polarized mode is unaffected as it is always perpendicular to the scattering vector $\boldsymbol{Q}$. Considering the *h0l* scattering plane we expect the same ratio suppression of the *c* polarized mode, but this time the *a* polarized mode nearly vanishes as the *h* com-
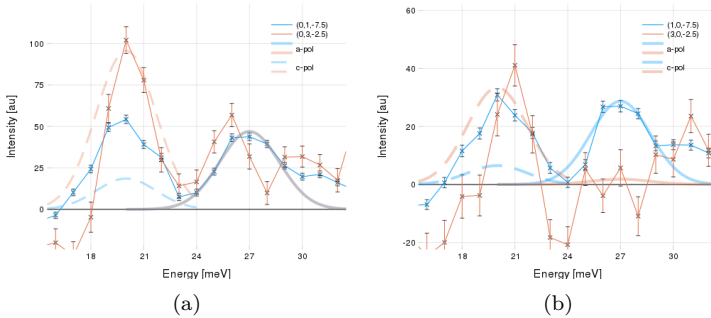
Figure 8.9: The polarization of the two spin-waves can be obtained by comparing their intensities in different Brillouin zones and correcting by the polarization factor and the twinning factor. Assuming transverse modes, the thick lines indicate the expected intensities for out-of-plane and in-plane spin-waves. The 27.5 meV feature can clearly be identified as an a polarized modes, whereas the 20 meV feature appears isotropic. Experimental data obtained at the IN8 [10, 11] spectrometer.

ponent is large compared to the l component of the scattering vector $\boldsymbol{Q}$. Comparing to the observed scattering intensities, the a polarized mode fits the behavior of the dispersive T magnon mode well. The localized mode, on the other hand, does not fit the expectations of a c polarized mode, as figure 8.9 shows. Also, an amplitude mode with polarization in b direction is not compatible as it would require almost complete suppression at $\boldsymbol{Q} = (0\ 3\ 2.5)$.

FM fluctuations   Above the structural transition we were able to observe FM fluctuations near the FM Bragg peak $\boldsymbol{Q} = (0\ 0\ 5)$ at 4 meV. This confirms the FM nature of the paramagnetic metal phase, already indicated by the Curie-Weis behavior of the magnetic moment.

SpinW Simulations

Considering the magnetism in the Ca$_{n+1}$Ru$_n$O$_{3n+1}$ series, the difference between the $n = 1$ and $n = 2$ compounds is an addi-
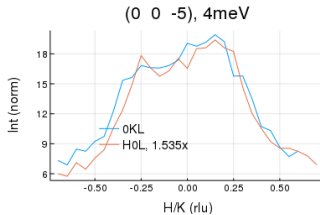
Figure 8.10: Scan of the FM fluctuations at (0 0 5) above T_N for both orientations of the array. Experimental data obtained at the IN8 [10, 11] spectrometer.

tional out-of-plane exchange coupling between the double layers of RuO_6 octahedra in the $n = 2$ compound. In a phenomenological description, the Hamiltonian is extended by an additional term that takes this out-of-plane superexchange J_c into account:

$$H = H_{\text{Ca}_2\text{RuO}_4} + J_c \sum_{\langle i,j \rangle_c} S_i S_j \tag{8.1}$$

In order to test whether this simple model is adequate, we have performed simulations with [131] from which we calculated the dispersions, as seen in figure 8.11. We set up a simulation that takes the lattice structure of $\text{Ca}_3\text{Ru}_{1.98}\text{Ti}_{0.02}\text{O}_7$ as a starting point and then compare the single-layer Hamiltonian to a bilayer Hamiltonian. While the first only allows considers in plane super-exchange interactions, the latter Hamiltonian allows additional isotropic inter-layer exchange interaction parametrized by J_c. The dispersion of the effective single layer interaction ($J_c = 0\,\text{meV}$) shows the same features as the dispersion of Ca_2RuO_4 (compare figure 8.11a with the Ca_2RuO_4 dispersion in figure 5.1).

Transverse Excitations Essentially, the additional intra-bilayer coupling J_c results in a change of the gap size and the bandwidth of the transverse in-plane spinwave. We also observe a doubling of the number of transverse modes, corresponding to excitations in-phase and out-of-phase between the bilayers. In figure fig-
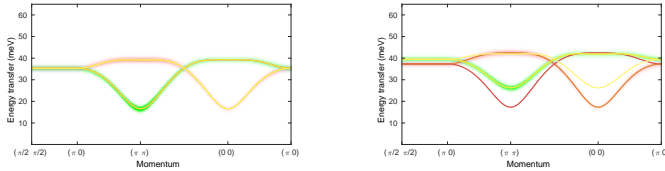
(a) *spinW simulation with* J_c $=$ 0 meV

(b) *spinW simulation with* J_c $=$ 3 meV

Figure 8.11: All simulations were performed on the structure obtained from the neutron diffraction measurements. *left*: Calculation of the spin-wave dispersion for a Hamiltonian identical to equation (5.3) that only respects in-plane superexchange interaction. *right*: Spectrum including an term that accounts for exchange interaction along the stacking direction within the bilayers. [131] simulations of AFM $Ca_3Ru_2O_7$.

ure 8.11 the modes at $l = 0$ are indicated by solid lines, whereas the shading indicated modes with $l = 2.5$.

Non-dispersive excitation localized in reciprocal space
The linear spinwave calculation is unable to capture all features of the observed dynamic magnetic response; namely the localized, non-dispersing feature in the magnon gap can not be reproduced. This feature follows the bilayer structure factor modulation along the l axis, from which we conclude that the feature is indeed intrinsic to the system.

8.4 Discussion

The metallic state of $Ca_3Ru_2O_7$ exhibits small Fermi surface pockets. By substituting Ti for Ru in $Ca_3Ru_2O_7$, the lattice is most likely deformed by Ti cations leading to a reduced bandwidth increasing the $U/\mathfrak{w}$ ratio. This, in turn, induces a Mott transition [67], that is associated with a sudden structural transition. The metallic phase favors direct exchange interactions are allowed resulting in ferromagnetic spin order. In the insulating phase only

super exchange interactions via the intermediate oxygen $2p$ orbitals are allowed, which favors an AFM ground state.

We have investigated this insulating AFM ground state and observe a lattice structure and spinwave spectrum that is similar to that of the closely related single layered compound Ca_2RuO_4. The similarities include: (1) the lattice deformations, i.e. tilt, rotation, and flattening of the RuO_6 octahedra, have almost the same values, (2) the a-polarized transverse spin-wave shows a maximum at the Γ point indicating active spin-orbit interaction coupling L_{eff} and S moments, (3) the simulation based on the phenomenological Hamiltonian only requires an additional intrabilayer coupling to reproduce the spinwave spectrum. All these properties are a strong indication that the system is in fact a pseudo-spin system that shows the excitonic soft-moment magnetism.

We investigated the MIT using high-resolution neutron diffraction measurements. We observe that the structural transition is very sharp (within $1\,K$) and that the AFM spin order is realized instantly in the distorted low temperature phase. Observing FM fluctuations above the transition we conclude that the structural changes separate the (spin) paramagnetic regime from the insulating J_{eff} regime.

In addition to the dispersing spin-wave, we observe an additional feature, localized both in reciprocal space around the magnetic ordering vector, and in energy, where it is observed as an isolated peak at $20\,meV$. A very similar excitation in Ti doped Ca_2RuO_4 has been attributed the partially polarized apical oxygen [46]. This is an unlikely scenario for the current situation, as the strong intensity would require a sizable magnetic moment and thus extreme polarization of the apical oxygen anions.

Recently, Vojta considered impurities in a singlet-triplet system[2] [164] and find these can lead to a reduction of the gap energy. In systems close to a quantum phase transitions, impurities can introduce areas characterized by *weaker* bonds, which have a decreased exchange interaction parameters. Such impurities may be introduced in $Ca_3Ru_{2-x}Ti_xO_7$ by dilute Ti substitution

---

[2]Vojta focus on dimerized quantum magnets, which formally describe a very similar scenario

levels. However, as these excitations are localized in real space, they are not able to disperse and are thus localized in reciprocal space around the magnetic zone center, where they show up as an additional excitations.

Our recent INS experiments are unable to identify all modes predicted by linear spin-wave theory. The strong distortions of the lattice lead to an increase of the number of elastic Bragg reflections, some of which are strong enough to introduce spurious features in the inelastic spectrum in triple-axis measurements. Furthermore, analysis of temperature-difference-curves are difficult as the high temperature phase is associated with different lattice parameters and lattice distortions, which result in different phonon energies. Consequently, weak magnetic signals are easily obscured. Furthermore, as in the case of the pristine Ca_2RuO_4, the bilayer structure factor and the magnetic form factor limit the available reciprocal space in which a magnetic signal can be observed.

Chapter 9

Conclusions

Transition metal oxides (TMOs) show a huge variety of physical properties, that arise from collective quantum phenomena such as magnetism and superconductivity. It is this advantage over semiconductors that makes this class of materials potentially relevant for industrial applications and can lead to new (magnetic) sensors [165], or superconductive wires. An important focus lies on the reduction of power consumption of everyday consumer electronics, which may be achieved by utilizing anisotropic transport properties of novel materials to reduce leakage currents. In order to create and possibly design materials with novel characteristics, it is imperative to understand the physics of TMOs at a fundamental level. Consequently, it is not surprising that TMOs have been at the center of scientific focus of the solid state research community for decades.

In the present work we investigate the importance of SOC in ruthenium oxides in the $4d^4$ configuration. Our INS investigations require a rather large quantity of high-quality single crystals. In the context of this thesis, excellent crystals of Ca_2RuO_4, $Ca_{2-x}Sr_xRuO_4$, $Ca_3Ru_2O_7$, and $Ca_3Ru_{2-x}Ti_xO_7$ were grown using mirror furnaces and applying the optical floating zone technique. Our experiments yielded information on the magnetic excitation spectrum of each compound, and enabled us to apply theoretical models and perform a quantitative analysis.

Role of SOC in magnetism

Using the time-of-flight INS technique, we investigated Ca_2RuO_4 and were able to obtain the complete magnetic excitation spectrum over the full magnetic Brillouin zone. The dispersion of the spin-waves indicates strong magnetic anisotropies in the system, originating from strong lattice deformations and conveyed via coupling between orbital and spin degrees of freedom. In Ca_2RuO_4 we find a complex interplay between SOC, lattice distortions, and superexchange interactions. The SOC is strong enough to couple spin and orbital angular momenta to effective total angular momenta $J_{\text{eff}} = S + L_{\text{eff}}$, which is expected to result in a singlet groundstate. The recently proposed mechanism of *excitonic magnetism* reconciles this expectation with the experimentally observed antiferromagnetic ground state in the insulating phase. Via condensation of triplet excitons the free energy of the system is minimized and the material acquires a nonzero magnetic moment. The amplitude of this soft magnetic moment depends on the population of the exciton condensate, which is *not driven by temperature* but by the effective coupling between the singlet and the triplet state, implying the existence of a quantum critical point. Quantum fluctuations of the population of the excitonic condensate allow for an amplitude mode, that is observable deep in the magnetic phase far from the onset of magnetic order. Such a behavior is not expected for conventional systems, where amplitude fluctuations are thermally driven by disordering the orientation of spin moments of fixed size; as a result, these excitations are only observable near the magnetic ordering temperature. This makes an intense amplitude mode deep in the magnetic phase a hallmark feature of the excitonic soft-moment magnetism. Fitting the dispersion relations obtained from the excitonic magnetism model to the transverse magnon branches, we find excellent agreement between calculation and data.

Using xyz polarization analysis of INS experiments we were able to observe three distinct magnetic modes at $5\,\text{K}$; namely the two transverse (Goldstone) modes as well as a longitudinal mode that carries the amplitude fluctuations (Higgs mode). Due to the vector character of the neutron's spin moment, neutrons

probe the longitudinal susceptibility of the system. In such a situation, the Higgs mode (for a two-dimensional system) usually diverges at the elastic line with ω^{-1} (*infrared singularity*) and is thus obscured by the more intense and massless Goldstone modes. In the case of Ca_2RuO_4 however, the amplitude mode as well as the transverse modes are massive due to orthorhombic lattice distortions, making it possible to study the Higgs mode's decay process into a pair of transverse Goldstone modes far from the elastic scattering channel. We thus provide clear evidence for a profound influence of the SOC in Ca_2RuO_4 and calculations show that the excitonic magnetism explains all observed features qualitatively and quantitatively.

Manipulating the energy hierarchy

In a next step, we investigated how the spin-wave spectrum evolves upon manipulation of the crystal lattice of the system. To this end we pursued two different approaches: *chemical substitution* and introducing an additional coupling between two layers of RuO_6 octahedra, changing the *dimensionality* of the spin system. The structural transition, which is concomitant to the metal-insulator Mott transition, is suppressed with increasing Sr contents. This causes the single crystals to degenerate at cryogenic temperatures. Despite this challenge we were able to obtain the dispersion of the *a* polarized magnon mode across the whole magnetic Brillouin zone. We compared the inelastic excitation spectrum of pristine Ca_2RuO_4 and $Ca_{1.9}Sr_{0.1}RuO_4$, and find a high similarity between the main features; namely a magnetic gap at the magnetic zone center and the maximum of the dispersion near the magnetic zone boundary. Fitting the experimental data with the dispersion relations calculated for the single layer compound [42, 107], we are able to indicate trends of the influence of the structural relaxations introduced through Sr substitution.

In order to study the influence of the dimensionality of the spin system, we considered the next higher member of the $Ca_{n+1}Ru_nO_{3n+1}$ Ruddlesden-Popper series, $Ca_3Ru_2O_7$. Here, an additional exchange interaction between the Ru cations of the double layer is introduced, resulting in an out-of-plane coupling along the stacking direction. Such a configuration favors metallic

behavior, and we indeed observe that $Ca_3Ru_2O_7$ does not become a good insulator for any temperature. Further differences to the single layer compound includes the spin order in the system. Instead of the G-type AFM phase, the system realizes an AFM phase where the single bilayers have a FM spin-order and are stacked antiferromagnetically separated by a CaO buffer layer.

Excitingly, $Ca_3Ru_2O_7$ becomes (Mott) insulating upon minute Ti substitution. In this insulating state, we can expect profound changes to the magnetism. Indeed, our TOF neutron scattering experiments revealed an excitation spectrum, which does not resemble the FM excitations of the undoped parent compound but the AFM spin-wave modes of Ca_2RuO_4. We have obtained a good qualitative description of the main magnon mode by applying the pseudo-spin Hamiltonian for the single layer compound with an additional term taking the exchange interaction within the double layer into account. Due to the striking similarities in the structural deformations, the spin-order, and the spin-wave excitations we conclude that the system exhibits the same soft-moment magnetism as Ca_2RuO_4. Conclusive proof, however, can only be obtained by observing the amplitude mode. This is a challenging task, as the scattering intensities are rather weak due to the magnetic moment of $1.3\mu_B$, and the lattice distortions result in a multitude of elastic Bragg peaks, that can obscure the intrinsic features of the excitation spectrum. The usual approach to separate the magnetic scattering intensity from the background by subtracting measurements below and above the magnetic ordering temperature is not applicable as well, as the structural transition at T_N causes a shift in energy of the phononic background. We thus propose further polarized inelastic neutron scattering experiments, that naturally sidestep these challenges and can provide information on the spin-wave polarization.

Besides the similarities of the excitonic spectrum, we find an additional feature in $Ca_3Ru_{2-x}Ti_xO_7$ with rather uncommon properties: Located at the magnetic zone center, a isolated and non-dispersing feature is observed at 20 meV. Exploiting the polarization factor, our INS studies indicate an isotropic behavior of this excitation. Vojta finds that bond disorder near quantum phase transitions can result in the transfer of spectral weight to lower energies [164] inside the spin-wave gap. The bond disorder

can be the result of impurities of the dilute Ti substitution in the sample material. Clustering of these chemical inhomogeneities can lead to the formation of islands in the material, characterized by reduced coupling parameters. If the number of such clusters is large enough, an additional excitation in the spin-wave gap can be realized, possibly changing the gap value, as well. Such low-energy localization tendencies are considerably stronger near quantum phase transitions [164], and are thus a valid consideration in the setting of a *excitonic magnet* such as $Ca_3Ru_{2-x}Ti_xO_7$.

Importance of the structure for the AFM state

In comparison to light TMs, the stronger SOC of metal ions in the fourth period of the periodic table makes them very susceptible to lattice distortions. Comparing the structure of ruthenates, we find a correlation between the highly distorted RuO_6 octahedra and the insulating G-type AFM phase. In particular, the similarities between our high-resolution powder diffraction data for $Ca_3Ru_{2-x}Ti_xO_7$ and the reported structural data for Ca_2RuO_4 suggest a stable regime, in which structural distortions provide a setting conductive for excitonic magnetism.

Complementary experiments and outlook

Neutron spectroscopy is, of course, not the only spectroscopic probe suited to investigate the magnetism in Ca_2RuO_4: Complementary approaches using inelastic photons scattering are *Raman* and *resonant inelastic X-Ray scattering* (RIXS) experiments. Indeed, a recent Raman experiment [45] on Ca_2RuO_4 was able to observe the two-Higgs process by directly coupling to the condensate. X-ray experiments resonant to the Ru *L*-edges yield complementary information, but are challenging from a technical perspective: the required X-ray wavelength is in an intermediate regime between hard and soft X-rays. Current developments of an intermediate x-ray energy RIXS spectrometer (IRIXS) PETRA III are being commissioned at the moment, offering exciting prospects for ruthenate compounds.

Currently, several questions are still unanswered. In particular, the influence of dilute doping of non-magnetic Ti in

$Ca_3Ru_{2-x}Ti_xO_7$ on the singlet-triplet mechanism requires further investigations. We propose polarized inelastic neutron spectroscopic experiments, which allow separation of the magnetic intensities from the nuclear signal and incoherent background and thus the mapping of all magnon modes. By performing an xyz polarization analysis the polarization of the magnon modes can be determined, which makes it possible to identify the polarization of the localized feature and might reveal an amplitude mode.

In conclusion, we have found active and profound coupling between spin and orbital degrees of freedom in the $4d^4$ ruthenates, which illustrates the importance of SOC even for compounds of moderately heavy transition metals. The possibility to tune the electronic interactions using structural deformations opens up further exciting avenues to investigate the implications of SOC in $4d$ transition metal oxides, and promises a wide range of exciting physical phenomena waiting to be explored.

Appendix A

Samples

A.1 Powder X-ray diffraction

All measurements were performed by Christine Stefani in the X-ray Service Group on Stoe X-ray diffractometers. The sample was obtained by grinding random single crystals of a single batch into a fine powder using an agate mortar and was filled into a capillary ($\varnothing$ =0.3 mm). Since Ru has low absorption and fluorescence cross sections for X-rays with λ =99.999 Å all diffractograms were taken with a Mo λ_{K1} source. The Rietveld refinement was performed using the TOPAS software suite.

A.2 Powder neutron diffraction

High resolution neutron data was taken at the SPODI [17, 18] diffractometer at the MLZ, Garching. We recorded data with two distinct wavelengths by choosing the (3 3 1) and the (5 5 1) Bragg reflection of the Ge monochromator. Here, $\lambda_{331} = 2.5354$ Å was chosen to determine the low temperature magnetic phase to provide a good resolution at low Q values (typical diffractorgram is plotted in figure A.1. The structural phase was determined using $\lambda_{551} = 1.5481$ Å.
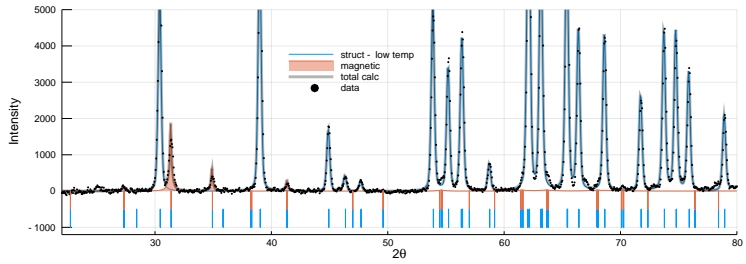
Figure A.1: Diffractogram of $Ca_3Ru_{1.98}Ti_{0.02}O_7$ using $\lambda_{331} = 2.5354\,\text{Å}$ to investigate the magnetic phase at $5\,\text{K}$.

	200K	70K	60K	50K	5K	5K Ge331
a	5.37246	5.36588	5.36595	5.36847	5.36845	5.36874
b	5.5242	5.52913	5.5295	5.59792	5.59866	5.59909
c	19.5591	19.5376	19.5359	19.3478	19.3455	19.3472
orth b-a	0.151741	0.163249	0.16355	0.229445	0.230217	0.230355
vol	580.486	579.654	579.649	581.446	581.45	581.578
RuO6 vol	10.2593	10.2506	10.2545	10.3067	10.3069	10.2959
Ru x	0.25199	0.2525	0.25222	0.25355	0.25266	0.25276
Ru y	0.7497	0.75416	0.75379	0.75071	0.75141	0.78476
Ru z	0.40111	0.40149	0.40152	0.40143	0.40151	0.40134
Ru-O(1)	1.98553	1.99286	1.99412	1.96729	1.97031	1.97599
Ru-O(2)	1.99245	1.98206	1.98179	1.96216	1.9606	1.96338
Ru-O(3)a	1.99529	1.99539	1.99825	2.025	2.01735	1.97459
Ru-O(3)b	2.01146	2.0134	2.00925	2.02232	2.02368	2.06708
Ru-O(4)a	1.98927	1.98746	1.98877	1.98544	1.99097	2.01023
Ru-O(4)b	1.98202	1.98045	1.97982	2.00538	2.00761	1.97394
Ru-O avg	1.99267	1.99194	1.992	1.9946	1.99509	1.9942
Ru-O ratio	0.997231	0.996636	0.99696	0.977702	0.977887	0.981673
Ru-O1-Ca2	155.465	155.004	154.755	153.455	153.643	154.617
Ru-O2-Ru	152.224	152.352	152.232	152.792	152.727	152.917
Ru-O3-Ru	149.74	149.884	149.806	149.471	149.435	149.469
Ru-O4-Ru	150.232	150.119	150.296	149.661	149.589	151.098
TiltO1	10.9972	11.312	11.2895	11.9678	11.8721	11.2517
TiltO2	13.888	13.8242	13.8842	13.604	13.6365	13.5416
TiltO3/4	13.9018	13.9436	13.9314	13.5995	13.6771	13.2174
Rot	11.3302	11.3854	11.3384	11.8868	11.8693	11.7354

Table A.1: $Ca_3Ru_{1.98}Ti_{0.02}O_7$: Powder Neutron Diffraction

Appendix B

Data analysis for triple axis spectrometers

B.1   UB Matrix Formalism

If the dataset is given in terms of instrument angles only the conversion is usually done using the UB matrix formalism introduced by Busing and Levy [166] and extended to arbitrarily oriented scattering planes by Lumsden, Robertson and Yethiraj [117]. In order to have the highest flexibility during our analysis and data treatment, we implemented an algorithm based on [117] into our analysis scripts using the programming language *Julia* which provide tooling to easily

- read data contained in ascii text files,
- analyze, modify, and combine datasets,
- and present the data.

The code is able to translate the instrument configuration into physical quantities relevant in a scattering experiment via the *UB matrix* formalism. Here, the orientation matrix U translates between laboratory frame and the crystal coordinate system determined by the primary and secondary Bragg peaks for alignment. The matrix B can be calculated with the sample's direct and re-

htb
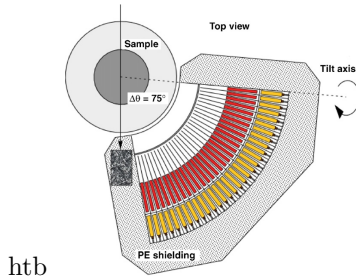
Figure B.1: Top view flatcone detector, taken from[12]

ciprocal lattice parameters (a_i, α_i and b_i, β_1, respectively) [166]:

$$B = \begin{pmatrix} b_1 & b_2 \cos \beta_3 & b_3 \cos \beta_2 \\ 0 & b_2 \sin \beta_3 & -b_3 \sin \beta_2 \cos \alpha_1 \\ 0 & 0 & a_3^- 1 \end{pmatrix} \qquad \text{(B.1)}$$

B.2   Flatcone Multi-Detector

The flatcone detector [12] is a multi-detector setup featuring 31 channels, each of which covers an angle of 1.3° within the scattering plane. Each channel has its own analyzer crystal made of $Si(_{111})$ single crystals that mostly eliminate the need for filters and are optimized for $k_f = 1.4\,\text{Å}^{-1}$ and $3.0\,\text{Å}^{-1}$, respectively. The flatcone detector can be tilted out of the horizontal plane in order to gain access to reciprocal space with an vertical component; at the same time the energy transfer is kept constant. To increase this vertical coverage, the sample stage of IN8 [10, 11] allow for a larger tilt than conventional triple axis spectrometers.

This layout requires determination of the correct 2θ angles for each channel; however, as soon as the detector and sample is tilted, this gets bit more involved.

Conventions

The ILL has unified naming conventions for the angles that define the scattering geometry of triple axis instruments. The angles associated with the three scatterers (monochromator, sample,

analyzer) and the corresponding instrument arms are numbered A1 to A6. Furthermore, the sample goniometers are characterized by GU and GL, corresponding to the inclination parallel and normal to k_i. In case of the flatcone detector, A4 is associated with the channel in the center and the inclination of the whole flatcone multi-detector is given as angle GFC. For the calculation we translate them into the quantities used in [117] (overview in table B.1) in order to be able to follow their steps.

Symbol	Description	Calculated from
k_i	initial wave vector	A1, A2, DM
k_f	final wave vector	A5, A6, DA
$\boldsymbol{k_f}$	final wave vector	k_f, GFC, A4
μ	goniometer ($\parallel \boldsymbol{k_i}$)	GU
ν	goniometer ($\perp \boldsymbol{k_i}$)	GL
s	sample rotation	A3
ω	sample offset rotation	$s = \theta + \omega$
θ	scattering angle	
χ	out-of-plane scattering angle	
ϕ	detector angle	A4, GFC
ϕ'	horizontal detector angle	
ψ	out-of-plane detector angle	

Table B.1: Overview on the different quantities and angles, and from which instrument parameters they derive. DM and DA is the *d* value for the monochromator / analyzer

Coordinate Systems

When dealing with scattering experiments there is a number of coordinate Systems involved. In some of these, the some quantities can be represented in a very simple form (for example $\boldsymbol{k_i} = (0, k_i, 0)$ in the laboratory frame and $\boldsymbol{Q_\theta} = (Q_\parallel, 0, Q_\perp)$ in the detector frame). To transform between the coordinate frames, we apply rotation matrices. All references to the reciprocal space is usually given in the crystals coordinate axis in units of reciprocal lattice units, or *Miller indices h, k,* and *l.* The *B* matrix translates that into absolute units in Å^{-1}, and the *U* matrix
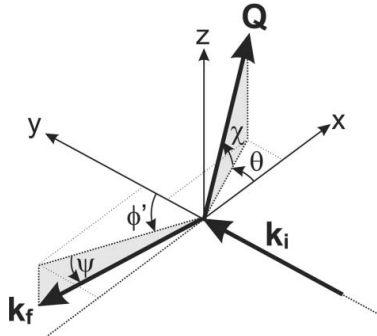
Figure B.2: Reproduced with permission of the International Union of Crystallography from [117].

System	Representation	Transformation	Units
crystal	Q	Q	r.l.u.
independent crystal	Q_c	$B\,Q$	Å^{-1}
oriented crystal	Q_ν	$UB\,Q$	Å^{-1}
detector	Q_θ	$R\,UB\,Q$	Å^{-1}
laboratory	Q_L	$\theta\,R\,UB\,Q$	Å^{-1}

Table B.2: Overview on the different coordinate frames and how to transform between them.

gives the relative orientation of the sample to the instrumental reference frame. In the detector frame can be obtained by the rotation matrix $R = \Omega_z M_y N_x$, that is a combination of of the goniometer angles μ and ν, and ω.

Out-of-plane Detector Angle χ

The layout of the flatcone detector and the recorded variable requires calculation of the out-of-plane detector angle χ. The relevant information can be found in the documentation of the MATLAB code package *Nplot* [167]

Powder correction for single crystal measurements

Depending on the crystals quality the inelastic channel might show scattering intensities corresponding to polycrystalline powder. Also, if higher order contamination is insufficiently suppressed powder like artifacts might be present, a case which might arise if filters can not used for a spectrometer configuration. Especially the flatcone detector relies on the Si analyzer crystals for elimination of higher order wavelength neutrons; however, in practice we observe powder rings caused by elastic and inelastic scattering.

For elastic scattering of powders this is usually corrected by subtracting a measurement of the sample environment only, which captures all contributions of aluminum or vanadium that might be in the beam path. If instead single crystals are used, such an approach is often unfeasible as for each instrument configuration a background scan is required, multiplying the measurement time considerably. Instead, we present a different approach: By analyzing the intensity histograms for each $|Q|$ value we can identify a background profile suitable to be used for the correction[1]. In figure B.3 we present an example, where we use the lowest 2.5 ‰ of all scattering intensity to create a background profile.
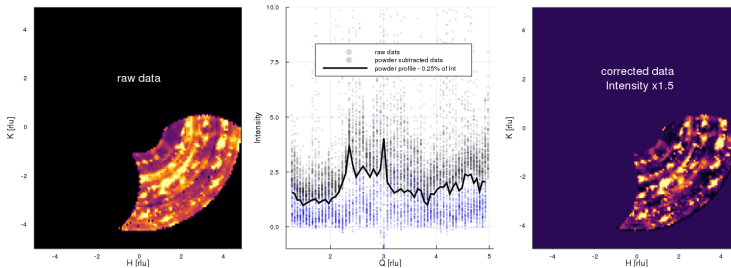
Figure B.3: Example for a background correction for data taken at IN8 [10, 11] using the flatcone detector ($Ca_3Ru_{2-x}Ti_xO_7$, 14 meV).

---

[1] This method was inspired by Paul Steffens implementation [167] for a similar algorithm: Instead of using a percentile of the lowest scattering intensities, his background profile is generated by averaging of scattering intensities with constant $|Q|$ where all signal has been removed manually.

Appendix C

Details of data analysis and further measurements

C.1   Ca₂RuO₄: xyz polarization analysis

In this study, the (h 0 l)-plane was assumed to be the scattering plane. However, the crystals were *twinned* and thus each domain needs to be considered in the analysis. The twinned domain can be considered to be identical to the main domain with the exception that a and b direction is flipped, such that the scattering plane for this domain is (0 k l)[1]. The two channels Γ_{sf}^{x} and Γ_{nsf}^{x} are sufficient to qualitatively distinguish between nuclear and magnetic scattering (see figure C.1). A comparison between the channels also allows estimation of spurious signals: by chance nuclear elastic scattering might occur with such a large intensity that some intensity spills over into the spin-flip channels. We have avoided the situation by moving slightly in h or l.

For a complete analysis of magnetic excitations and removal of the background, the remaining sf/channels Γ_{sf}^{y} and Γ_{sf}^{z} are required. While we are able to clearly distinct three modes and the qualitative difference between the in-plane and out-of-plane

---

[1]Since the orthorhombicity is very small compared to the instrumental resolution, we can work in the tetragonal setting and use (0 h l) instead of (0 k l) as the scattering plane for the second domain when dealing with small H values.
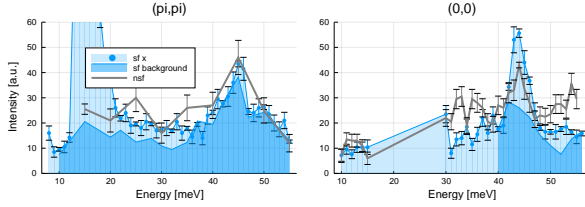
Figure C.1: Raw intensities for spin-flip (light blue) and non-spin-flip (gray) channels. The nuclear scattering is comparable to the background in the spin-flip channels (dark blue shading) and with its moderate intensity no spill-over into the spin-flip channels is expected.
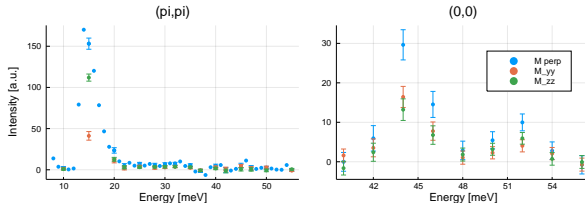
Figure C.2: here be dragons!

modes is readily visible in figure C.2, the signal is a mixture of both domains. From equation (4.11) follows:

$$\begin{pmatrix} M_\perp \\ M_{yy} \\ M_{zz} \end{pmatrix} = p_{h0l} \begin{pmatrix} M_\perp \\ M_{yy} \\ M_{zz} \end{pmatrix}_{h0l} + (1 - p_{h0l}) \begin{pmatrix} M_\perp \\ M_{yy} \\ M_{zz} \end{pmatrix}_{0hl} \tag{C.1}$$

where $p_{h\,0\,l}$ is the twinning or domain volume ratio.

Before continuing to extract the polarization character along the crystallographic directions, we need to determine the twinning ratio. To this end, the l dependence of the $15\,\mathrm{meV}$ feature at $(1\ 0\ L)$ is inspected, from which we know from orientation-factor analysis that its polarization is along the a direction (in-plane transverse mode):

$$M_{yy} = p_{h0l} \cdot F(\mathrm{Ru}^+) \cdot M_a \cdot q_c / |\boldsymbol{Q}| \tag{C.2}$$

$$M_{zz} = (1 - p_{h0l}) \cdot F(\mathrm{Ru}^+) \cdot M_a \tag{C.3}$$
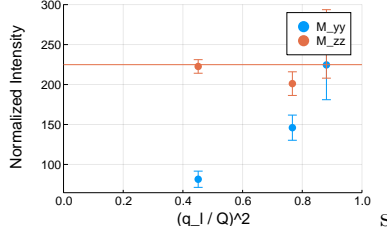
Figure C.3: Determination of the twinning ratio

Following this analysis we extracted a twinning ratio of $p_{h\,0\,l} = 0.52$ and will use the rounded value of $p_{h\,0\,l} = 0.5$ for further analysis. However, with a domain population of $p_{h\,0\,l} = 0.5$ the single moments can not be fully separated and only information about of the transversal out-of-plane moment M_c and the superposition of the moments M_a and M_b can be extracted:

$$M_a + M_b = 2M_{zz} \tag{C.4}$$

$$M_c = \frac{M_{yy} - \cos(\alpha)M_{zz}}{\sin(\alpha)} \tag{C.5}$$

In order to determine the nature of the peak, the ratio of M_y and M_z must be inspected. From the INS experiment, one finds:

$$\frac{M_y}{M_z} = \frac{10.1875}{1.375} = 7.409 \pm 1.055 \tag{C.6}$$

To calculate the orientation factor, the angle between q vector and the c axis of the crystals is calculated: This makes it possible to determine the ratio between M_y and M_z:

$$\frac{M_y}{M_z} = \frac{\cos(\alpha) \cdot (M_a + M_b) + \sin(\alpha) \cdot M_c}{M_a + M_b} \tag{C.7}$$

$$= 0.196 + M_c \cdot \frac{0.981}{M_a + M_b} \tag{C.8}$$

For the case the magnetic moments are not aligned along the c-axis, the maximum value of the ratio is $\frac{M_y}{M_z} = 1.177$ which is clearly smaller than the observed ratio, characterizing this mode as out-of-plane transversal.

123

Time-of-flight INS on Ca$_2$RuO$_4$ powder

We have performed *time-of-flight* INS on single crystals and on crystalline powder at the ARCS [1, 2] spectrometer. While single crystal measurements yield a four dimensional data-set (transferred energy, and all three components of the momentum transfer), the powder investigations (transferred energy, and scalar size of the transferred momentum) can achieve high statistics even with short counting times. Thus, powder measurements are especially useful for investigating the temperature dependence of inelastic excitations.

(a) $E_i = 100\,\mathrm{meV}$

(b) $E_i = 600\,\mathrm{meV}$
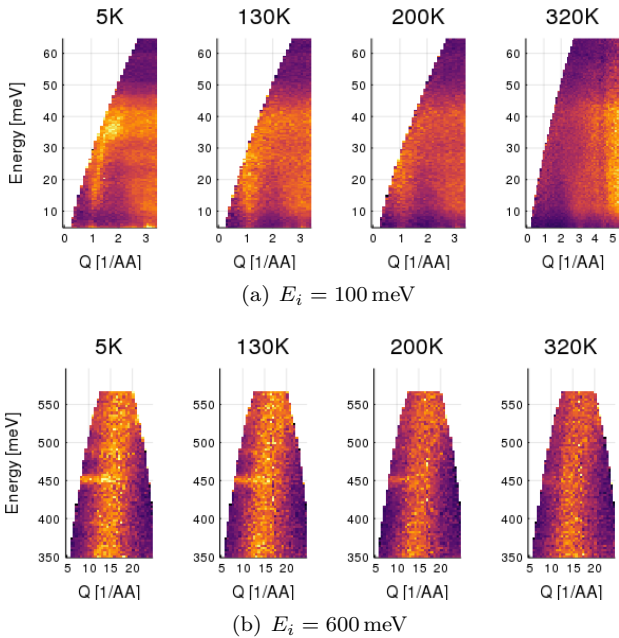
The powder sample was obtained by crushing single crystals of Ca$_2$RuO$_4$ grown with the optical floating zone method and grinding them to a homogeneous powder. We filled about 3 g in a Va tube ($\varnothing$ =1 cm), and adjusted the vertical slits to a window of 3 cm. Reference measurements of the empty part of the can were made with a opening of the vertical slits of 1 cm.

However, the statistics of this background measurements were too little to perform a correction (i.e. subtracting the scaled can measurements from the powder data). The resolution of ARCS [1, 2] is about 4 % of the incident energy. We investigated the system with several distinct incident energies ranging from 100 meV to 1300 meV, resulting in data-sets with different energy resolution (about 4 meV to 50 meV, respectively).

At low q-value we observe three clusters of features. The first is corresponds to the magnetic excitations which we already discussed earlier in section 5.1 and have energies lower than 60 meV. The two other clusters are found at higher energies of about 450 meV and 900 meV. We present an overview on the temperature dependence in appendix C.1 for three different E_i.

Let us first discuss the temperature dependence of the low energy magnon modes: The $E_i = 100$ meV data set captures the magnon dispersion nicely. We followed the dispersion through the AFM transition temperature and find that the gap remains open up to high temperatures (see figure C.4a), although its value decreases.
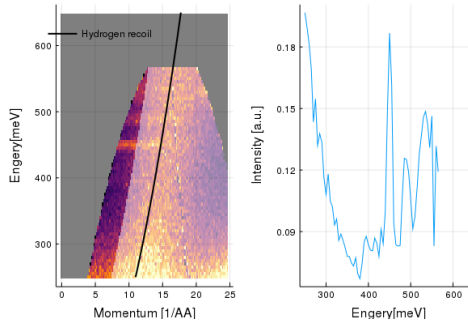
Figure C.4: High energy features are visible for medium initial neutron energies of $E_i = 600$ meV.

The data set with $E_i = 600$ meV gives the best insights for the features around 450 meV. The most striking feature is the hydrogen recoil signature, that describes the scattering of neutrons from H in the sample volume, where the H originates from residual water present in the sample powder. The data shows

two rather sharp excitations at $450\,\mathrm{meV}$ and $490\,\mathrm{meV}$. Furthermore, comparison of the $320\,\mathrm{K}$ data with the data set taken at $5\,\mathrm{K}$ may indicate an intensity distribution in the range $520\,\mathrm{meV}$ to $570\,\mathrm{meV}$. However, kinematic restrictions at low and the H-recoil process at high energies leave only a small volume to free of contamination and make the detection of a continuum difficult. By carefully masking the integrated area we were able to reliably isolate the signal, which can be seen in figure C.4. Further evidence for these modes is found in the $E_i = 800\,\mathrm{meV}$ data set.

The third cluster of low-q excitations is found at around $700\,\mathrm{meV}$ and $1000\,\mathrm{meV}$ as can be seen in figure C.9. The reliable identification of signal is difficult in this energy regime as the energy resolution is about $50\,\mathrm{meV}$ and the accessible reciprocal space is rather small. Consequently, the separation of signal and background is challenging. By restricting the window of q integration by the onset of the H-recoil signal, we are able to identify a broad intensity.
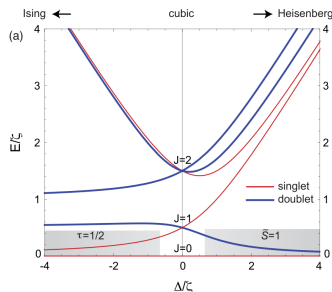
Figure C.5: Influence of the tetragonal elongation and compression of the RuO_6 octahedra on the $J_{\mathrm{eff}} = 1$ levels. Figure is taken from [168].

Comparing the energies to the expected J_{eff} state in that region, we try to map the observed excitations to the level structure displayed in figure C.5. From these calculations, we expect four separate excitations: two singlet states and two doublet states; the level splitting in the latter due to orthorhombic lattice distortions is not expected to be smaller than the instrument resolution and is not considered here. Assigning the modes to the expected excitations is problematic as we observe less features than

expected, but we can speculate that the intense and sharp feature at 450 meV corresponds to the $J_{\text{eff}} = 1$ T_z mode, and the sharp signal at 490 meV to the $J_{\text{eff}} = 2$ singlet. From this assignment we calculate the tetragonal compression to $\delta = {}^\Delta\!/_\zeta = 3.5$ (4), depending on the value used for the atomic SOC constant $\zeta = 150$ meV (130 meV).
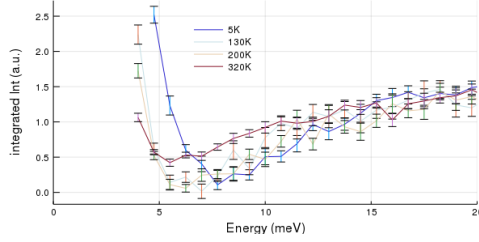
Figure C.6: Ca$_2$RuO$_4$: ToF – $E_i = 100$ meV
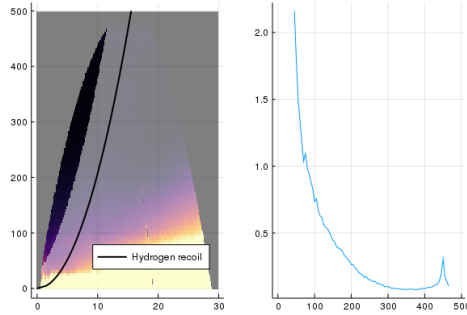
Figure C.7: Ca$_2$RuO$_4$: ToF – $E_i = 500$ meV
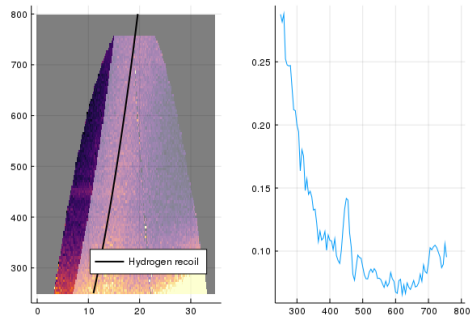
Figure C.8: Ca$_2$RuO$_4$: ToF $-$ E_i =800 meV
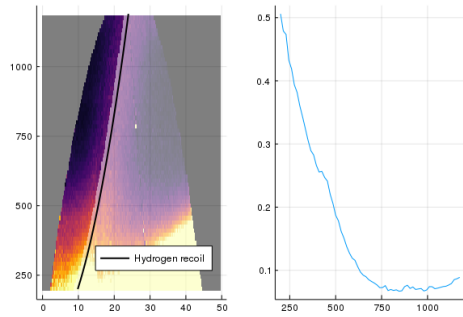
Figure C.9: Ca$_2$RuO$_4$: ToF $-$ E_i =1300 meV

List of Figures

References

[1] *ARCS: Wide Angular-Range Chopper Spectrometer* (cit. on pp. 3, 43, 51, 60–62, 67, 79–81, 124, 125). URL: https://neutrons.ornl.gov/arcs (visited on 15/01/2019).

[2] D. L. Abernathy et al. 'Design and operation of the wide angular-range chopper spectrometer ARCS at the Spallation Neutron Source'. In: *Review of Scientific Instruments* 83 (1st Jan. 2012), p. 015114 (cit. on pp. 3, 43, 51, 60–62, 67, 79–81, 124, 125). DOI: 10/fxng3v.

[3] *ALBA BOREAS* (cit. on pp. 3, 91). URL: https://www.cells.es/en/beamlines/en/beamlines/bl29-boreas (visited on 22/01/2019).

[4] A. Barla et al. 'Design and performance of BOREAS, the beamline for resonant X-ray absorption and scattering experiments at the ALBA synchrotron light source'. In: *J Synchrotron Rad* 23 (1st Nov. 2016), pp. 1507–1517 (cit. on pp. 3, 91). DOI: 10.1107/S1600577516013461.

[5] *HZB E6* (cit. on pp. 3, 50, 92, 95). URL: https://www.helmholtz-berlin.de/pubbin/igama_output?modus=einzel&sprache=en&gid=1701&typoid=39942 (visited on 15/01/2019).

[6] *PSI EIGER* (cit. on pp. 3, 87). URL: https://www.psi.ch/ (visited on 22/01/2019).

[7]   U. Stuhr et al. 'The thermal triple-axis-spectrometer EI-GER at the continuous spallation source SINQ'. In: *Nucl. Instrum. Methods Phys. Res. Sect. Accel. Spectrometers Detect. Assoc. Equip.* 853 (May 2017), pp. 16–19 (cit. on pp. 3, 87).
DOI: 10.1016/j.nima.2017.02.003.

[8]   J. Kulda et al. 'IN20 – The ILL high-flux polarised-neutron three-axis spectrometer'. In: *Appl Phys A* 74 (1st Dec. 2002), s246–s248 (cit. on pp. 3, 54, 68, 84).
DOI: 10/dqkg4s.

[9]   *ILL IN20* (cit. on pp. 3, 54, 68, 84).
URL: /users/instruments/instruments-list/in20/description/instrument-layout/ (visited on 15/01/2019).

[10]   *ILL IN8* (cit. on pp. 3, 53, 83, 84, 86, 96–100, 116, 119).
URL: /users/instruments/instruments-list/in8/description/instrument-layout/ (visited on 15/01/2019).

[11]   A. Hiess et al. 'ILL's renewed thermal three-axis spectro-meter IN8: A review of its first three years on duty'. In: *Physica B: Condensed Matter* 385-386 (15th Nov. 2006), pp. 1077–1079 (cit. on pp. 3, 53, 83, 84, 86, 96–100, 116, 119).
DOI: 10/b2sgmr.

[12]   M. Kempa et al. 'The FlatCone multianalyzer setup for ILL's three-axis spectrometers'. In: *Physica B: Condensed Matter.* Proceedings of the Eighth International Conference on Neutron Scattering 385–386, Part 2 (15th Nov. 2006). 00031, pp. 1080–1082 (cit. on pp. 3, 116).
DOI: 10.1016/j.physb.2006.05.371.

[13]   *ISIS Merlin* (cit. on pp. 4, 96).
URL: https://www.isis.stfc.ac.uk/Pages/Merlin.aspx (visited on 15/01/2019).

[14]   R. I. Bewley et al. 'MERLIN, a new high count rate spectrometer at ISIS'. In: *Physica B: Condensed Matter* 385-386 (15th Nov. 2006), pp. 1029–1031 (cit. on pp. 4, 96).
DOI: 10/fjngtn.

[15] *PUMA: Thermal three axes spectrometer* (cit. on pp. 4, 84–86, 96).
URL: http://jlsrf.org/index.php/lsf/article/view/36 (visited on 15/01/2019).

[16] O. Sobolev and J. T. Park. 'PUMA: Thermal three axes spectrometer'. In: *J. Large-Scale Res. Facil. JLSRF* 1 (19th Aug. 2015), p. 13 (cit. on pp. 4, 84–86, 96).
DOI: 10/gftfhz.

[17] *SPODI: High-resolution neutron diffractometer* (cit. on pp. 4, 50, 92, 95, 111).
URL: https://mlz-garching.de/spodi (visited on 15/01/2019).

[18] M. Hoelzel, A. Senyshyn and O. Dolotko. 'SPODI: High Resolution Powder Diffractometer'. In: *J. Large-Scale Res. Facil. JLSRF* 1 (18th Aug. 2015). bibtex{ addendum: "Copyrighted under the CC BY license.}, p. 5 (cit. on pp. 4, 50, 92, 95, 111).
DOI: 10.17815/jlsrf-1-24.

[19] F. J. Morin. 'Oxides Which Show a Metal-to-Insulator Transition at the Neel Temperature'. In: *Phys. Rev. Lett.* 3 (1st July 1959), pp. 34–36 (cit. on p. 14).
DOI: 10.1103/PhysRevLett.3.34.

[20] A. Menth and J. P. Remeika. 'Magnetic Properties of $V_{2-x}Cr_xO_3$'. In: *Phys. Rev. B* 2 (1st Nov. 1970), pp. 3756–3762 (cit. on p. 14).
DOI: 10.1103/PhysRevB.2.3756.

[21] F. Nakamura et al. 'Electric-field-induced metal maintained by current of the Mott insulator Ca_2RuO_4'. In: *Sci. Rep.* 3 (29th Aug. 2013) (cit. on p. 14).
DOI: 10/gftd97.

[22] C. S. Alexander et al. 'Observation of a Structurally-Driven Mott Transition in Single Crystal Ca_2RuO_4'. In: (Dec. 1998) (cit. on pp. 14, 28).

[23] M. N. Baibich et al. 'Giant Magnetoresistance of (001) Fe/(001)Cr Magnetic Superlattices'. In: *Phys. Rev. Lett.* 61 (21st Nov. 1988), pp. 2472–2475 (cit. on p. 14).
DOI: 10.1103/PhysRevLett.61.2472.

[24] A.-M. Haghiri-Gosnet and J.-P. Renard. 'CMR manganites: physics, thin films and devices'. In: *J. Phys. Appl. Phys.* 36 (21st Apr. 2003). 00784, R127–R150 (cit. on p. 14).
DOI: 10.1088/0022-3727/36/8/201.

[25] A. P. Ramirez. 'Colossal magnetoresistance'. In: *J. Phys. Condens. Matter* 9 (29th Sept. 1997), pp. 8171–8199 (cit. on p. 14).
DOI: 10.1088/0953-8984/9/39/005.

[26] S. Sachdev and B. Keimer. 'Quantum criticality'. In: *Phys. Today* 64 (1st Feb. 2011), p. 29 (cit. on p. 14).
DOI: 10.1063/1.3554314.

[27] J. G. Bednorz and K. A. Müller. 'Possible high T_c superconductivity in the Ba−La−Cu−O system'. In: *Z. Für Phys. B Condens. Matter* 64 (June 1986). 00000, pp. 189–193 (cit. on pp. 14, 15, 26).
DOI: 10.1007/BF01303701.

[28] B. Keimer et al. 'From quantum matter to high-temperature superconductivity in copper oxides'. In: *Nature* 518 (12th Feb. 2015), pp. 179–186 (cit. on pp. 14, 15).
DOI: 10.1038/nature14165.

[29] Y. Maeno et al. 'Superconductivity in a layered perovskite without copper'. In: *Nature* 372 (8th Dec. 1994), pp. 532–534 (cit. on pp. 15, 26).
DOI: 10/dqtw6w.

[30] J. Hubbard. 'Electron correlations in narrow energy bands'. In: *Proc. R. Soc. Lond. A* 276 (26th Nov. 1963), pp. 238–257 (cit. on p. 16).
DOI: 10.1098/rspa.1963.0204.

[31] J. Bendix, M. Brorson and C. E. Schaffer. 'Accurate empirical spin-orbit coupling parameters .zeta.nd for gaseous ndq transition metal ions. The parametrical multiplet term model'. In: *Inorg. Chem.* 32 (June 1993), pp. 2838–2849 (cit. on p. 17).
DOI: 10.1021/ic00065a010.

[32] B. J. Kim et al. 'Novel $J_{\text{eff}} = 1/2$ Mott State Induced by Relativistic Spin-Orbit Coupling in Sr_2IrO_4'. In: *Phys. Rev. Lett.* 101 (15th Aug. 2008), p. 076402 (cit. on p. 17). DOI: 10.1103/PhysRevLett.101.076402.

[33] R. J. Elliott and M. F. Thorpe. 'Orbital Effects on Exchange Interactions'. In: *J. Appl. Phys.* 39 (Feb. 1968), pp. 802–807 (cit. on pp. 17, 33, 63, 71). DOI: 10.1063/1.2163622.

[34] T. Mizokawa. 'Orbital polarization in layered t_{2g} electron systems'. In: *New J. Phys.* 6 (17th Nov. 2004), pp. 169–169 (cit. on p. 17). DOI: 10.1088/1367-2630/6/1/169.

[35] J. H. Jung et al. 'Change of electronic structure in Ca_2RuO_4 induced by orbital ordering'. In: *Phys. Rev. Lett.* 91 (31st July 2003), p. 056403 (cit. on p. 17). DOI: 10.1103/PhysRevLett.91.056403.

[36] T. Yokoya et al. 'Evidence for correlation effects in Sr_2RuO_4 from resonant and x-ray photoemission spectroscopy'. In: *Phys. Rev. B* 53 (1st Apr. 1996), pp. 8151–8154 (cit. on p. 17). DOI: 10.1103/PhysRevB.53.8151.

[37] S. N. Ruddlesden and P. Popper. 'The compound $Sr_3Ti_2O_7$ and its structure'. In: *Acta Crystallogr.* 11 (1st Jan. 1958), pp. 54–55 (cit. on p. 18). DOI: 10.1107/S0365110X58000128.

[38] H. D. Megaw. 'Crystal structure of barium titanium oxide and other double oxides of the perovskite type'. In: *Trans. Faraday Soc.* 42 (1946), A224 (cit. on p. 18). DOI: 10.1039/tf946420a224.

[39] K. Lukaszewicz. 'Struktura krystaliczna tytanianow strontu $\alpha-(SrO)_2(TiO)$ and $(SrO)_3(TiO_2)_2$'. In: *Rocz. Chem.* 33 (1959), pp. 239–242 (cit. on p. 18).

[40] S. Sugano. *Multiplets of Transition-Metal Ions in Crystals.* OCLC: 880413872. Burlington: Elsevier Science, 2012 (cit. on p. 19).

[41] S. Kunkemöller et al. 'Highly Anisotropic Magnon Dispersion in Ca_2RuO_4: Evidence for Strong Spin Orbit Coupling'. In: *Phys. Rev. Lett.* 115 (8th Dec. 2015). 00000, p. 247201 (cit. on p. 20).
      DOI: 10.1103/PhysRevLett.115.247201.

[42] A. Jain et al. 'Higgs mode and its decay in a 2D antiferromagnet'. In: *Nat. Phys.* 13 (27th Mar. 2017), pp. 633–637 (cit. on pp. 20, 63–65, 68–70, 107).
      DOI: 10.1038/nphys4077.

[43] T. Mizokawa et al. 'Spin-Orbit Coupling in the Mott Insulator Ca_2RuO_4'. In: *Phys. Rev. Lett.* 87 (July 2001) (cit. on pp. 20, 71).
      DOI: 10.1103/PhysRevLett.87.077202.

[44] S. J. Yuan et al. 'Evolution of magnetism in single-crystal $Ca_2Ru_{1-x}Ir_xO_4$ ($0 \leq x \leq 0.65$)'. In: *Phys. Rev. B* 92 (24th July 2015), p. 024425 (cit. on p. 20).
      DOI: 10.1103/PhysRevB.92.024425.

[45] S.-M. Souliou et al. 'Raman Scattering from Higgs Mode Oscillations in the 2D Antiferromagnet Ca_2RuO_4'. In: *Phys. Rev. Lett.* 119 (8th Aug. 2017). 00000 (cit. on pp. 20, 109).
      DOI: 10.1103/PhysRevLett.119.067201.

[46] S. Kunkemöller et al. 'Magnon dispersion in $Ca_2Ru_{1-x}Ti_xO_4$: Impact of spin-orbit coupling and oxygen moments'. In: *Phys. Rev. B* 95 (12th June 2017), p. 214408 (cit. on pp. 20, 102).
      DOI: 10.1103/PhysRevB.95.214408.

[47] P. Steffens et al. 'Magnetic excitations in the metallic single-layer ruthenates $Ca_{2-x}Sr_xRuO_4$ studied by inelastic neutron scattering'. In: *Phys. Rev. B* 83 (24th Feb. 2011). 00000 (cit. on p. 20).
      DOI: 10.1103/PhysRevB.83.054429.

[48] G. Cao and P. Schlottmann. '$Ca_3Ru_2O_7$: A new paradigm for spintronics'. In: *Mod. Phys. Lett. B* 22 (30th July 2008), pp. 1785–1813 (cit. on pp. 21, 35).
      DOI: 10.1142/S0217984908016480. Copyright @ 2016,

[49] G. Cao et al. 'From antiferromagnetic insulator to ferro-magnetic metal: a brief review of the layered ruthenates'. In: *Mater. Sci. Eng. B* 63 (Aug. 1999). 00000, pp. 76–82 (cit. on pp. 20, 25).
DOI: 10.1016/S0921-5107(99)00055-0.

[50] G.-Q. Liu. 'Mott transition and magnetic anisotropy in $Ca_3Ru_2O_7$'. In: *Phys. Rev. B* 84 (Dec. 2011) (cit. on p. 21).
DOI: 10.1103/PhysRevB.84.235137.

[51] G. Cao et al. 'Field-tuned collapse of an orbitally ordered and spin-polarized state: Colossal magnetoresistance in the bilayered ruthenate $Ca_3Ru_2O_7$'. In: *Phys. Rev. B* 69 (Jan. 2004), p. 014404 (cit. on pp. 21, 35).
DOI: 10.1103/PhysRevB.69.014404.

[52] D. J. Singh and S. Auluck. 'Electronic Structure and Bulk Spin-Valve Behavior in $Ca_3Ru_2O_7$'. In: *Phys. Rev. Lett.* 96 (7th Mar. 2006) (cit. on pp. 21, 35).
DOI: 10.1103/PhysRevLett.96.097203.

[53] G. Cao et al. 'Quantum oscillations, colossal magnetores-istance, and the magnetoelastic interaction in bilayered $Ca_3Ru_2O_7$'. In: *Phys. Rev. B* 67 (6th May 2003). 00000, p. 184405 (cit. on pp. 21, 35).
DOI: 10.1103/PhysRevB.67.184405.

[54] G. Cao et al. 'Tunneling magnetoresistance and quantum oscillations in bilayered $Ca_3Ru_2O_7$'. In: *Phys. Rev. B* 67 (28th Feb. 2003), p. 060406 (cit. on pp. 21, 35).
DOI: 10.1103/PhysRevB.67.060406.

[55] G. Cao et al. 'Orbitally driven behaviour: Mott transition, quantum oscillations and colossal magnetoresistance in bilayered $Ca_3Ru_2O_7$'. In: *New J. Phys.* 6 (6th Nov. 2004), pp. 159–159 (cit. on pp. 21, 35).
DOI: 10.1088/1367-2630/6/1/159.

[56] S. McCall, G. Cao and J. E. Crow. 'Impact of magnetic fields on anisotropy in $Ca_3Ru_2O_7$'. In: *Phys. Rev. B* 67 (31st Mar. 2003), p. 094427 (cit. on pp. 21, 35).
DOI: 10.1103/PhysRevB.67.094427.

[57] J. F. Karpus et al. 'Raman scattering studies of field-induced melting of the orbital-ordered state of $Ca_3Ru_2O_7$'. In: *Physica B* 359 (30th Apr. 2005), pp. 1234–1236 (cit. on p. 21).
DOI: 10.1016/j.physb.2005.01.368.

[58] C. S. Snow et al. 'Pressure-Tuned Collapse of the Mott-Like State in $Ca_{n+1}Ru_nO_{3n+1}$ ($n = 1, 2$): Raman Spectroscopic Studies'. In: *Phys. Rev. Lett.* 89 (6th Nov. 2002) (cit. on pp. 21, 35).
DOI: 10.1103/PhysRevLett.89.226401.

[59] J. F. Karpus et al. 'Spectroscopic study of the field- and pressure-induced phases of the bilayered ruthenate $Ca_3Ru_2O_7$'. In: *Phys. Rev. B Condens. Matter Mater. Phys.* 73 (2006), p. 134407 (cit. on pp. 21, 86).
DOI: 10.1103/PhysRevB.73.134407.

[60] G. Cao et al. 'Spin-charge coupling for dilute La-doped $Ca_3Ru_2O_7$'. In: *Phys. Rev. B* 62 (1st July 2000). 00000, pp. 998–1003 (cit. on p. 21).
DOI: 10.1103/PhysRevB.62.998.

[61] G. Cao et al. 'Multiple magnetic phase transitions in single-crystal $Ca_{3-x}SrxRu_2O_7$ for $0 < x < 3.0$'. In: *Phys. Rev. B* 56 (1997), p. 5387 (cit. on p. 21).

[62] Y. Yoshida et al. 'Magnetic properties and magnetic structures of $Sr_{3-x}Ca_xRu_2O_7$'. In: *J. Phys. Chem. Solids* 72 (May 2011), pp. 559–561 (cit. on p. 21).
DOI: 10.1016/j.jpcs.2010.10.024.

[63] J. Peng et al. 'Interplay between the lattice and spin degrees of freedom in $Ca_{3-x}SrxRu_2O_7$'. In: *Phys. Rev. B* 82 (15th July 2010), p. 024417 (cit. on p. 21).
DOI: 10.1103/PhysRevB.82.024417.

[64] Z. Qu et al. 'Complex electronic states in double-layered ruthenates $Ca_{3-x}SrxRu_2O_7$'. In: *Phys. Rev. B* 80 (30th Sept. 2009). 00000 (cit. on p. 21).
DOI: 10.1103/PhysRevB.80.115130.

[65]   G. Cao et al. 'Observation of Strong Spin Valve Effect in Bulk $Ca_3Ru_{2-x}Cr_xO_7$'. In: *Phys. Rev. Lett.* 100 (9th Jan. 2008). 00000 (cit. on pp. 21, 35).
DOI: 10.1103/PhysRevLett.100.016604.

[66]   M. Zhu et al. 'Field-induced metastability of the modulation wave vector in a magnetic soliton lattice'. In: *Phys. Rev. B* 95 (19th Apr. 2017), p. 134429 (cit. on p. 21).
DOI: 10.1103/PhysRevB.95.134429.

[67]   S. Tsuda et al. 'Mott transition extremely sensitive to impurities in $Ca_3Ru_2O_7$ revealed by hard x-ray photoemission studies'. In: *Phys. Rev. B* 87 (25th June 2013). 00000, p. 241107 (cit. on pp. 21, 35, 89, 90, 101).
DOI: 10.1103/PhysRevB.87.241107.

[68]   G. Khaliullin. 'Excitonic Magnetism in Van Vleck-type d^4 Mott Insulators'. In: *Phys. Rev. Lett.* 111 (5th Nov. 2013), p. 197201 (cit. on pp. 22, 33, 34, 60, 63–65, 75).
DOI: 10.1103/PhysRevLett.111.197201.

[69]   E. Dagotto. 'Complexity in Strongly Correlated Electronic Systems'. In: *Science* 309 (8th July 2005), pp. 257–262 (cit. on p. 26).
DOI: 10.1126/science.1107559.
pmid: 16002608.

[70]   M. Braden et al. 'Crystal and magnetic structure of Ca_2RuO_4: Magnetoelastic coupling and the metal-insulator transition'. In: *Phys. Rev. B* 58 (1st July 1998), pp. 847–861 (cit. on pp. 26–29, 93).
DOI: 10.1103/PhysRevB.58.847.

[71]   T. Vogt and D. Buttrey. 'Low-temperature structural behavior of Sr_2RuO_4'. In: *Phys. Rev. B* 52 (1st Oct. 1995), R9843–R9846 (cit. on pp. 26, 27).
DOI: 10.1103/PhysRevB.52.R9843.

[72]   T. M. Rice and M. Sigrist. 'Sr_2RuO_4: an electronic analogue of ^{3}He?' In: *J. Phys. Condens. Matter* 7 (1995), p. L643 (cit. on p. 27).
DOI: 10.1088/0953-8984/7/47/002.

[73] A. P. Mackenzie and Y. Maeno. 'The superconductivity of Sr_2RuO_4 and the physics of spin-triplet pairing'. In: *Rev. Mod. Phys.* 75 (1st May 2003), pp. 657–712 (cit. on p. 27). DOI: 10.1103/RevModPhys.75.657.

[74] Y. Maeno et al. 'Evaluation of Spin-Triplet Superconductivity in Sr_2RuO_4'. In: *J. Phys. Soc. Jpn.* 81 (26th Dec. 2011), p. 011009 (cit. on p. 27). DOI: 10.1143/JPSJ.81.011009.

[75] Y. Yanase and M. Ogata. 'Microscopic Identification of the D-vector in Triplet Superconductor Sr_2RuO_4'. In: *J. Phys. Soc. Jpn.* 72 (15th Mar. 2003), pp. 673–687 (cit. on p. 27). DOI: 10.1143/JPSJ.72.673.

[76] M. Haverkort et al. 'Strong Spin-Orbit Coupling Effects on the Fermi Surface of Sr_2RuO_4 and Sr_2RhO_4'. In: *Phys. Rev. Lett.* 101 (July 2008) (cit. on p. 27). DOI: 10.1103/PhysRevLett.101.026406.

[77] E. J. Rozbicki et al. 'Spin–orbit coupling and k-dependent Zeeman splitting in strontium ruthenate'. In: *J. Phys.: Condens. Matter* 23 (2011), p. 094201 (cit. on p. 27). DOI: 10.1088/0953-8984/23/9/094201.

[78] C. N. Veenstra et al. 'Spin-Orbital Entanglement and the Breakdown of Singlets and Triplets in Sr_2RuO_4 Revealed by Spin- and Angle-Resolved Photoemission Spectroscopy'. In: *Phys. Rev. Lett.* 112 (26th Mar. 2014), p. 127002 (cit. on p. 27). DOI: 10.1103/PhysRevLett.112.127002.

[79] A. P. Mackenzie et al. 'Quantum Oscillations in the Layered Perovskite Superconductor Sr_2RuO_4'. In: *Phys. Rev. Lett.* 76 (13th May 1996), pp. 3786–3789 (cit. on p. 27). DOI: 10.1103/PhysRevLett.76.3786.

[80] E. Ohmichi et al. 'Magnetoresistance of Sr_2RuO_4 under high magnetic fields parallel to the conducting plane'. In: *Phys. Rev. B* 61 (1st Mar. 2000), pp. 7101–7107 (cit. on p. 27). DOI: 10.1103/PhysRevB.61.7101.

[81] C. Bergemann et al. 'Detailed Topography of the Fermi Surface of Sr_2RuO_4'. In: *Phys. Rev. Lett.* 84 (20th Mar. 2000), pp. 2662–2665 (cit. on p. 27).
DOI: 10.1103/PhysRevLett.84.2662.

[82] A. Mackenzie et al. 'Calculation of thermodynamic and transport properties of Sr_2RuO_4 at low temperatures using known fermi surface parameters'. In: *Phys. C Supercond.* 263 (May 1996), pp. 510–515 (cit. on p. 27).
DOI: 10.1016/0921-4534(95)00770-9.

[83] Y. Yoshida et al. 'Fermi Surface Properties in Sr_2RuO_4'. In: *J. Phys. Soc. Jpn.* 68 (15th Sept. 1999), pp. 3041–3053 (cit. on p. 27).
DOI: 10.1143/JPSJ.68.3041.

[84] C. Bergemann et al. 'Normal state of the unconventional superconductor Sr_2RuO_4 in high magnetic fields'. In: *Phys. B Condens. Matter* 294-295 (Jan. 2001), pp. 371–374 (cit. on p. 27).
DOI: 10.1016/S0921-4526(00)00680-3.

[85] Y. Tokura et al. 'Filling dependence of electronic properties on the verge of metal–Mott-insulator transition in $Sr_{1-x}La_xRiO_3$'. In: *Phys. Rev. Lett.* 70 (5th Apr. 1993), pp. 2126–2129 (cit. on p. 27).
DOI: 10.1103/PhysRevLett.70.2126.

[86] A. P. Mackenzie et al. 'Extremely Strong Dependence of Superconductivity on Disorder in Sr_2RuO_4'. In: *Phys. Rev. Lett.* 80 (5th Jan. 1998), pp. 161–164 (cit. on p. 27).
DOI: 10/b562dq.

[87] S. Nakatsuji et al. 'Metal-insulator transition in $Ca_{2-x}Sr_xRuO_4$'. In: *Phys. B Condens. Matter* 259 (1999). 00000, pp. 949–950 (cit. on pp. 27, 75).

[88] S. Nakatsuji, S.-i. Ikeda and Y. Maeno. 'Ca_2RuO_4 : New Mott Insulators of Layered Ruthenate'. In: *J. Phys. Soc. Jpn.* 66 (15th July 1997), pp. 1868–1871 (cit. on pp. 27–29, 75).
DOI: 10.1143/JPSJ.66.1868.

[89] O. Friedt. 'Interplay between electronic, magnetic and structural instabilities in $Ca_{2-x}Sr_xRuO_4$: A neutron scattering study'. 00000. Paris: Universite Paris XI, Mar. 2003 (cit. on p. 27).

[90] A. V. Puchkov et al. 'Layered ruthenium oxides: from band metal to Mott insulator'. In: *Phys. Rev. Lett.* 81 (1998), p. 2747 (cit. on p. 27).
DOI: 10.1103/PhysRevLett.81.2747.

[91] Z. Fang, N. Nagaosa and K. Terakura. 'Orbital-dependent phase control in $Ca_{2-x}Sr_xRuO_4$ ($0 \leq x \leq 0.5$)'. In: *Phys. Rev. B* 69 (30th Jan. 2004), p. 045116 (cit. on pp. 28, 32, 75).
DOI: 10.1103/PhysRevB.69.045116.

[92] S. Nakatsuji and Y. Maeno. 'Switching of magnetic coupling by a structural symmetry change near the Mott transition in $Ca_{2-x}Sr_xRuO_4$'. In: *Phys. Rev. B* 62 (2000). 00000, p. 6458 (cit. on pp. 28, 75).

[93] Z. W. Li et al. 'Spin fluctuations in $Sr_{1.6}Ba_{0.4}RuO_4$: An inelastic neutron scattering study with polarization analysis'. In: *Phys. Rev. B* 95 (4th Jan. 2017). WOS:000391310500003, p. 045105 (cit. on p. 28).
DOI: 10.1103/PhysRevB.95.045105.

[94] Z. Fang and K. Terakura. 'Magnetic phase diagram of $Ca_{2-x}Sr_xRuO_4$ governed by structural distortions'. In: *Phys. Rev. B* 64 (1st July 2001). 00000 WOS:000169835700021, p. 020509 (cit. on pp. 29, 32, 75, 82).
DOI: 10.1103/PhysRevB.64.020509.

[95] O. Friedt et al. 'Structural and magnetic aspects of the metal-insulator transition in $Ca_{2-x}Sr_xRuO_4$'. In: *Phys. Rev. B* 63 (Apr. 2001). 00000 (cit. on pp. 29, 75, 76, 78, 82).
DOI: 10.1103/PhysRevB.63.174432.

[96] G. Cao et al. 'Magnetic and transport properties of single-crystal Ca_2RuO_4: Relationship to superconducting Sr_2RuO_4'. In: *Phys. Rev. B* 56 (1st Aug. 1997), R2916–R2919 (cit. on p. 29).
DOI: 10.1103/PhysRevB.56.R2916.

[97]   F. Nakamura et al. 'From Mott insulator to ferromagnetic metal: A pressure study of Ca_2RuO_4'. In: *Phys. Rev. B* 65 (23rd May 2002) (cit. on pp. 30–32).
DOI: 10.1103/PhysRevB.65.220402.

[98]   Y. Yamauchi et al. 'Pressure induced novel-phenomena in Mott insulator Ca_2RuO_4'. In: *Phys. C Supercond.* 470 (Dec. 2010), S740–S741 (cit. on p. 30).
DOI: 10.1016/j.physc.2009.12.049.

[99]   P. Steffens et al. 'High-pressure diffraction studies on Ca_2RuO_4'. In: *Phys. Rev. B* 72 (7th Sept. 2005), p. 094104 (cit. on p. 30).
DOI: 10.1103/PhysRevB.72.094104.

[100]   H. Taniguchi et al. 'Anisotropic uniaxial pressure response of the Mott insulator Ca_2RuO_4'. In: *Phys. Rev. B* 88 (12th Nov. 2013) (cit. on p. 30).
DOI: 10.1103/PhysRevB.88.205111.

[101]   R. Ishikawa et al. 'Control of the electronic states of Ca_2RuO_4 by uniaxial pressure'. In: *J. Phys. Conf. Ser.* 400 (17th Dec. 2012), p. 022036 (cit. on p. 30).
DOI: 10.1088/1742-6596/400/2/022036.

[102]   C. Dietl et al. 'Tailoring the electronic properties of Ca_2RuO_4 via epitaxial strain'. In: *Appl. Phys. Lett.* 112 (15th Jan. 2018), p. 031902 (cit. on p. 30).
DOI: 10.1063/1.5007680.

[103]   P. L. Alireza et al. 'Evidence of superconductivity on the border of quasi-2D ferromagnetism in Ca_2RuO_4 at high pressure'. In: *J. Phys. Condens. Matter* 22 (10th Feb. 2010), p. 052202 (cit. on pp. 30, 31).
DOI: 10.1088/0953-8984/22/5/052202.

[104]   S. Riccò et al. 'In-situ strain-tuning of the metal-insulator-transition of Ca_2RuO_4 in angle-resolved photoemission experiments'. In: (1st Mar. 2018). 00000 (cit. on p. 31).
arXiv: 1803.00488 [cond-mat].

[105]   J. Bertinshaw et al. 'A Unique Crystal Structure of Ca_2RuO_4 in the Current Stabilized Metallic State'. In: (17th June 2018) (cit. on p. 31).
arXiv: 1806.06455 [cond-mat].

[106] C. Sow et al. 'Current-induced strong diamagnetism in the Mott insulator Ca_2RuO_4'. In: *Science* 358 (24th Nov. 2017), pp. 1084–1087 (cit. on p. 31).
DOI: 10.1126/science.aah4297.
pmid: 29170239.

[107] A. Akbari and G. Khaliullin. 'Magnetic excitations in a spin-orbit-coupled d^4 Mott insulator on the square lattice'. In: *Phys. Rev. B* 90 (28th July 2014) (cit. on pp. 34, 60, 63–65, 69, 75, 82, 107).
DOI: 10.1103/PhysRevB.90.035137.

[108] V. Durairaj et al. 'Observation of oscillatory magnetoresistance periodic in $1/B$ and B in $Ca_3Ru_2O_7$'. In: *Phys. Rev. B* 73 (27th Feb. 2006). 00000, p. 054434 (cit. on p. 35).
DOI: 10.1103/PhysRevB.73.054434.

[109] J. F. Karpus et al. 'Field-induced orbital and magnetic phases in $Ca_3Ru_2O_7$'. In: *Phys. Rev. Lett.* 93 (15th Oct. 2004), p. 167205 (cit. on p. 35).
DOI: 10.1103/PhysRevLett.93.167205.

[110] X. N. Lin et al. 'Colossal Magnetoresistance by Avoiding a Ferromagnetic State in the Mott System $Ca_3Ru_2O_7$'. In: *Phys. Rev. Lett.* 95 (30th June 2005) (cit. on p. 35).
DOI: 10.1103/PhysRevLett.95.017203.

[111] F. Baumberger et al. 'Nested Fermi Surface and Electronic Instability in $Ca_3Ru_2O_7$'. In: *Phys. Rev. Lett.* 96 (17th Mar. 2006), p. 107601 (cit. on p. 35).
DOI: 10.1103/PhysRevLett.96.107601.

[112] X. Ke et al. 'Emergent Electronic and Magnetic State in $Ca_3Ru_2O_7$ Induced by Ti Doping'. In: *Phys. Rev. B* 84 (4th Nov. 2011). 00000 (cit. on pp. 36, 89).
DOI: 10.1103/PhysRevB.84.201102.

[113] J. Peng et al. 'Extremely large anisotropic transport caused by electronic phase separation in Ti-doped $Ca_3Ru_2O_7$'. In: *J. Phys. Appl. Phys.* 49 (2016). 00000, p. 245004 (cit. on pp. 36, 89).
DOI: 10.1088/0022-3727/49/24/245004.

[114] T. Zou et al. 'Pressure-induced electronic and magnetic phase transitions in a Mott insulator: Ti-doped $Ca_3Ru_2O_7$ bilayer ruthenate'. In: *Phys. Rev. B* 94 (27th July 2016). 00000, p. 041115 (cit. on p. 36).
DOI: 10.1103/PhysRevB.94.041115.

[115] A. Zevalkink. *Research Projects.* 23rd Mar. 2016 (cit. on p. 38).
URL: https://alexzevalkink.wordpress.com/research/ (visited on 15/01/2019).

[116] S. Nakatsuji and Y. Maeno. 'Synthesis and Single-Crystal Growth of $Ca_{2-x}Sr_xRuO_4$'. In: *Journal of Solid State Chemistry* 156.1 (Jan. 2001), pp. 26–31 (cit. on p. 40).
DOI: 10.1006/jssc.2000.8953.

[117] M. D. Lumsden, J. L. Robertson and M. Yethiraj. 'UB matrix implementation for inelastic neutron scattering experiments'. In: *J Appl Cryst, J Appl Crystallogr* 38 (1st June 2005), pp. 405–411 (cit. on pp. 46, 115, 117, 118).
DOI: 10.1107/S0021889805004875.

[118] *2014 CODATA recommended values* (cit. on p. 48).
URL: https://physics.nist.gov/cuu/Constants/ (visited on 14/11/2018).

[119] W. Soller. 'A New Precision X-ray Spectrometer'. In: *Phys. Rev.* 24 (1st Aug. 1924), pp. 158–167 (cit. on p. 50).
DOI: 10.1103/PhysRev.24.158.

[120] F. Mezei, ed. *Neutron Spin Echo.* Vol. 128. Lecture Notes in Physics. Berlin, Heidelberg: Springer Berlin Heidelberg, 1980 (cit. on p. 52).
DOI: 10.1007/3-540-10004-0.

[121] F. Mezei, C. Pappas and T. Gutberlet. *Neutron Spin Echo Spectroscopy Basics, Trends and Applications.* OCLC: 801043493. Berlin, Heidelberg: Springer-Verlag Berlin Heidelberg : Springer e-books, 2003 (cit. on p. 52).

[122] R. Golub and R. Gähler. 'A neutron resonance spin echo spectrometer for quasi-elastic and inelastic scattering'. In: *Physics Letters A* 123 (13th July 1987), pp. 43–48 (cit. on p. 52).
DOI: 10.1016/0375-9601(87)90760-2.

[123] R. Gähler and R. Golub. 'Neutron resonance spin echo, bootstrap method for increasing the effective magnetic field'. In: *J. Phys. France* 49 (1st July 1988), pp. 1195–1202 (cit. on p. 52).
DOI: 10.1051/jphys:019880049070119500.

[124] M. Krautloher et al. 'Neutron Resonance Spin Echo with Longitudinal DC Fields'. In: *Rev. Sci. Instrum.* 87 (1st Dec. 2016), p. 125110 (cit. on p. 52).
DOI: 10.1063/1.4972395.

[125] O. Schärpf and H. Capellmann. 'The XYZ-Difference Method with Polarized Neutrons and the Separation of Coherent, Spin Incoherent, and Magnetic Scattering Cross Sections in a Multidetector'. In: *Phys. Status Solidi A* 135 (1993). 00000, pp. 359–379 (cit. on p. 55).

[126] W. Schweika. 'XYZ-polarisation analysis of diffuse magnetic neutron scattering from single crystals'. In: *J. Phys. Conf. Ser.* 211 (1st Feb. 2010). 00017, p. 012026 (cit. on p. 55).
DOI: 10.1088/1742-6596/211/1/012026.

[127] O. Arnold et al. 'Mantid—Data analysis and visualization package for neutron scattering and μSR experiments'. In: *Nucl. Instrum. Methods Phys. Res. Sect. Accel. Spectrometers Detect. Assoc. Equip.* 764 (Nov. 2014), pp. 156–166 (cit. on p. 56).
DOI: 10.1016/j.nima.2014.07.029.

[128] F. Akeroyd et al. *Mantid: Manipulation and Analysis Toolkit for Instrument Data.* 2013 (cit. on p. 56).
DOI: 10.5286/SOFTWARE/MANTID.

[129] R. T. Azuah et al. 'DAVE: A Comprehensive Software Suite for the Reduction, Visualization, and Analysis of Low Energy Neutron Spectroscopic Data'. In: *J. Res.*

Natl. Inst. Stand. Technol. 114 (Nov. 2009), p. 341 (cit. on p. 56).
DOI: 10.6028/jres.114.025.

[130] R. Ewings et al. 'Horace : Software for the analysis of data from single crystal spectroscopy experiments at time-of-flight neutron instruments'. In: *Nucl. Instrum. Methods Phys. Res. Sect. Accel. Spectrometers Detect. Assoc. Equip.* 834 (Oct. 2016), pp. 132–142 (cit. on p. 56).
DOI: 10.1016/j.nima.2016.07.036.

[131] S. Tóth. *Tsdev/Spinw: Pyspinw 3.0.* 00000. 2nd Aug. 2017 (cit. on pp. 56, 100, 101).
DOI: 10.5281/zenodo.838034.

[132] J. Rodriguez-Carvajal. 'FULLPROF: a program for Rietveld refinement and pattern matching analysis'. In: *satellite meeting on powder diffraction of the XV congress of the IUCr.* Vol. 127. Toulouse, France:[sn]. 1990 (cit. on pp. 56, 57).

[133] *DIFFRAC.SUITE TOPAS - XRD Software, X-ray diffraction* (cit. on p. 56).
URL: https://www.bruker.com/products/x-ray-diffraction-and-elemental-analysis/x-ray-diffraction/xrd-software/topas.html (visited on 21/11/2018).

[134] H. M. Rietveld. 'A profile refinement method for nuclear and magnetic structures'. In: *J. Appl. Crystallogr.* 2 (2nd June 1969), pp. 65–71 (cit. on pp. 57, 93).
DOI: 10.1107/S0021889869006558.

[135] J. Rodríguez-Carvajal. 'Recent advances in magnetic structure determination by neutron powder diffraction'. In: *Phys. B Condens. Matter* 192 (Oct. 1993), pp. 55–69 (cit. on pp. 57, 93).
DOI: 10.1016/0921-4526(93)90108-I.

[136] J. Rodríguez-Carvajal. 'Recent developments of the program FULLPROF'. In: *Comm. Powder Diffr. IUCr Newsl.* 26 (2001), pp. 12–19 (cit. on p. 57).

149

R E F E R E N C E S

[137] L. B. McCusker et al. 'Rietveld refinement guidelines'. In: *J. Appl. Crystallogr.* 32 (1st Feb. 1999), pp. 36–50 (cit. on p. 57).
D O I : 10.1107/S0021889898009856.

[138] T. Sommer, M. Vojta and K. Becker. 'Magnetic properties and spin waves of bilayer magnets in a uniform field'. In: *Eur. Phys. J. B* 23 (Oct. 2001), pp. 329–339 (cit. on p. 65).
D O I : 10.1007/s100510170052.

[139] M. Matsumoto et al. 'Field- and pressure-induced magnetic quantum phase transitions in TlCuCl3 '. In: *Phys. Rev. B* 69 (25th Feb. 2004) (cit. on p. 65).
D O I : 10.1103/PhysRevB.69.054423.

[140] D. Podolsky, A. Auerbach and D. P. Arovas. 'Visibility of the amplitude (Higgs) mode in condensed matter'. In: *Phys. Rev. B* 84 (23rd Nov. 2011) (cit. on p. 70).
D O I : 10.1103/PhysRevB.84.174522.

[141] C. Rüegg et al. 'Bose-Einstein condensation of the triplet states in the magnetic insulator $TlCuCl_3$'. In: *Nature* 423 (1st May 2003), pp. 62–65 (cit. on p. 72).
D O I : 10.1038/nature01617.

[142] C. Rüegg et al. 'Quantum Magnets under Pressure: Controlling Elementary Excitations in $TlCuCl_3$'. In: *Phys. Rev. Lett.* 100 (21st May 2008) (cit. on p. 72).
D O I : 10.1103/PhysRevLett.100.205701.

[143] T. Giamarchi, C. Rüegg and O. Tchernyshyov. 'Bose-Einstein condensation in magnetic insulators'. In: *Nat. Phys.* 4 (Mar. 2008), pp. 198–204 (cit. on p. 72).
D O I : 10.1038/nphys893.

[144] S. Nakatsuji and Y. Maeno. 'Quasi-two-dimensional Mott transition system $Ca_{2-x}Sr_xRuO_4$'. In: *Phys. Rev. Lett.* 84 (20th Mar. 2000). 00000 WOS:000085924400029, pp. 2666–2669 (cit. on pp. 75, 76).
D O I : 10.1103/PhysRevLett.84.2666.

[145] V. I. Anisimov et al. 'Orbital-selective Mott-insulator transition in $Ca_{2-x}Sr_xRuO_4$'. In: *Eur. Phys. J. B* 25 (1st Jan. 2002). 00000, pp. 191–201 (cit. on p. 75). DOI: 10.1140/epjb/e20020021.

[146] J. S. Lee et al. 'Electron and Orbital Correlations in $Ca_{2-x}Sr_xRuO_4$ Probed by Optical Spectroscopy'. In: *Phys. Rev. Lett.* 89 (3rd Dec. 2002). 00000 (cit. on p. 75). DOI: 10.1103/PhysRevLett.89.257402.

[147] H. Rho et al. 'Raman scattering studies of spin, charge, and lattice dynamics in $Ca_{2-x}Sr_xRuO_4$ ($0 \leq x < 0.2$)'. In: *Phys. Rev. B* 68 (1st Sept. 2003), p. 100404 (cit. on p. 75). DOI: 10.1103/PhysRevB.68.100404.

[148] J. Jung. 'Raman scattering and optical absorption studies of an orbital ordered $Ca_{2-x}Sr_xRuO_4$'. In: *Solid State Commun.* 133 (Jan. 2005), pp. 103–107 (cit. on p. 75). DOI: 10.1016/j.ssc.2004.10.008.

[149] H. Rho et al. 'Raman scattering studies of $Ca_{2-x}Sr_xRuO_4$'. In: *Physica B: Condensed Matter* 359–361 (30th Apr. 2005), pp. 1270–1272 (cit. on p. 75). DOI: 10.1016/j.physb.2005.01.353.

[150] A. Liebsch and H. Ishida. 'Subband Filling and Mott Transition in $Ca_{2-x}Sr_xRuO_4$'. In: *Phys. Rev. Lett.* 98 (24th May 2007). 00000, p. 216403 (cit. on p. 75). DOI: 10.1103/PhysRevLett.98.216403.

[151] G.-Q. Liu. 'Spin-orbit coupling induced Mott transition in $Ca_{2-x}Sr_xRuO_4$ ($0 \leq x \leq 0.2$)'. In: *Phys. Rev. B* 84 (Dec. 2011) (cit. on p. 75). DOI: 10.1103/PhysRevB.84.235136.

[152] R. Shaheen et al. 'Atomistic computer simulation studies of Sr_2RuO_4 and Ca_2RuO_4'. In: *J. Phys. Chem. Solids* 64 (2003), pp. 237–245 (cit. on p. 76). DOI: 10.1016/S0022-3697(02)00283-4.

[153] J. P. Carlo et al. 'New magnetic phase diagram of $Ca_{2-x}Sr_xRuO_4$'. In: *Nat. Mater.* 11 (19th Feb. 2012). 00000, pp. 323–328 (cit. on p. 76). DOI: 10.1038/nmat3236.

[154]   R. D. Shannon. 'Revised effective ionic radii and systematic studies of interatomic distances in halides and chalcogenides'. In: *Acta Crystallogr. Sect. A* 32 (1st Sept. 1976), pp. 751–767 (cit. on pp. 81, 90).
DOI: 10.1107/S0567739476001551.

[155]   X. Ke et al. 'Spin-wave Excitation in the Antiferromagnetic Bilayer Ruthenate $Ca_3Ru_2O_7$'. In: *Phys. Rev. B* 84 (27th July 2011), p. 014422 (cit. on pp. 83, 85, 88).
DOI: 10.1103/PhysRevB.84.014422.

[156]   T. Chatterji et al. 'Spin waves in the quasi-2D ferromagnetic bilayer manganite $La_{1.2}Sr_{1.8}Mn_2O_7$'. In: *Phys. Rev. B* 60 (1st Sept. 1999), R6965–R6968 (cit. on p. 83).
DOI: 10.1103/PhysRevB.60.R6965.

[157]   J. Peng et al. 'From quasi-two-dimensional metal with ferromagnetic bilayers to Mott insulator with G-type antiferromagnetic order in $Ca_3(Ru_{1-x}Ti_x)_2O_7$'. In: *Phys. Rev. B* 87 (20th Feb. 2013). 00000, p. 085125 (cit. on p. 89).
DOI: 10.1103/PhysRevB.87.085125.

[158]   J. Peng et al. 'Magnetic phase separation in double layer ruthenates $Ca_3(Ru_{1-x}Ti_x)_2O_7$'. In: *Sci. Rep.* 6 (14th Jan. 2016). 00000, p. 19462 (cit. on p. 89).
DOI: 10.1038/srep19462.

[159]   J. Brand. 'Magnetismus von unkonventionellen Supraleitern am Beispiel von Ruthenat- und Eisen-Arsenid-Verbindungen'. Universität zu Köln, 2013 (cit. on pp. 90, 93).

[160]   C. R. Rotundu et al. 'Physical properties and electronic structure of a new barium titanate suboxide $Ba_{1+x}Ti_{13-x}O_{12}$ ($x = 0.11$)'. In: *APL Mater.* 3 (Apr. 2015), p. 041517 (cit. on p. 91).
DOI: 10.1063/1.4916991.   Copyrighted under the CC BY license. Changes: only characteristic response of Ti4+, Ti3+, and Ti2+ was retained.

[161]   K. Momma and F. Izumi. 'VESTA 3 for 3D visualization of crystal, volumetric and morphology data'. In: *J Appl Cryst, J Appl Crystallogr* 44 (1st Dec. 2011), pp. 1272–1276 (cit. on p. 94).
DOI: 10.1107/S0021889811038970.

[162] Y. Yoshida et al. 'Crystal and magnetic structure of Ca$_3$Ru$_2$O$_7$'. In: *Phys. Rev. B* 72 (9th Aug. 2005), p. 054412 (cit. on p. 93).
DOI: 10.1103/PhysRevB.72.054412.

[163] S. Price. 'Streuuntersuchungen an komplexen Schichtruthenaten'. Cologne: Universität zu Köln, 2008 (cit. on p. 93).

[164] M. Vojta. 'Excitation spectra of disordered dimer magnets near quantum criticality'. In: *Phys. Rev. Lett.* 111 (27th Aug. 2013) (cit. on pp. 102, 108, 109).
DOI: 10.1103/PhysRevLett.111.097202.
arXiv: 1301.4223.

[165] J. Heremans. 'Solid state magnetic field sensors and applications'. In: *J. Phys. Appl. Phys.* 26 (14th Aug. 1993), pp. 1149–1168 (cit. on p. 105).
DOI: 10.1088/0022-3727/26/8/001.

[166] W. R. Busing and H. A. Levy. 'Angle calculations for 3- and 4-circle X-ray and neutron diffractometers'. In: *Acta Crystallogr.* 22 (1967), pp. 457–464 (cit. on pp. 115, 116).
DOI: 10.1107/S0365110X67000970.

[167] *Matlab Scripts for TAS. Includes routines for Flatcone (plotmultiple etc.) and standard TAS (nplot)* (cit. on pp. 118, 119).
URL: https://github.com/nplot/nplot (visited on 30/08/2018).

[168] B. J. Kim and G. Khaliullin. 'Resonant inelastic x-ray scattering operators for t_{2g} orbital systems'. In: *Phys. Rev. B* 96 (7th Aug. 2017) (cit. on p. 126).
DOI: 10.1103/PhysRevB.96.085108.

Acknowledgments

Research such as the one presented here is only possible through excellent supervision and a dependable team of co-workers. Thus, there are many people I would like to thank for the help and support, both on a personal and professional level.

In particular, I am very grateful to Prof. Bernhard Keimer. He welcomed me into his department and gave me the opportunity to work in the amazing environment that Max Planck institutes provide, making one of my earliest wishes come true. His guidance helped me to stay on track with the project and the many experiments, while at the same time giving me a free hand to pursue my own interests. I also highly appreciated the possibility to take part in many international workshops, where I could present my research.

Next, I would like to thank all *three* of my day-to-day supervisors, in order of appearance:

- Dr. Anil Jain, who was involved in starting the project and guided me in the very first beam times.
- Dr. BJ Kim, who supported me throughout the whole project and was always available for discussion, no matter the distance. You were really inspiring with your drive to constantly explore new uncharted territory.
- and Dr. Joel Bertinshaw, with whom I spent days and nights on beamtimes—I have made a lot of good memories of exploring reciprocal space, automating scans via scripts and then having a pint in the next bar, or staying up all the night baby-sitting the instrument.

A special thanks to Dr. Reinhard Kremer for assuming the role of an external supervisor and helping out wherever he could; your

genuine interest was and is much appreciated.

Of course, many more people were crucial for the success of this project. Dr. Gihun Ryu taught me about crystal growth, and we became good friends during the long hours of optimizing the process. Dr. Giniyat Khaliullin was an excellent partner to discuss the theoretical foundations or the interpretation of the experimental data. Dr. Thomas Keller has been a mentor to me since my masters thesis, and I really appreciate him always being available for discussions. Juan Porras became a good friend, who freely shared his knowledge and was always available to discuss details or join a beamtime—even if it was not immediately connected to his own research. Furthermore, I would like to thank all members of the metal and glass workshops, X-ray diffraction service group, crystal growth group, crystal preparation group, and that helped me. In particular,

- Dr. Chengtian Lin and Dr. Masahiko Isobe who provided me with the opportunity to use the equipment of the crystal growth group, and providing great advice to improve crystal growth.
- Horst Bender, who saved the project more than once by repairing the optical furnaces—you are a life-saver!

Last but not least, I am very thankful to all instrument scientists I have encountered in my 175 days of beamtime during the last four years. We probably spent the most time with Dr. Sasha (Alexandre) Ivanov, as he was local contact for almost all inelastic measurements we conducted at the ILL. His dedication to the instruments and the neutron scattering technique in general were inspiring and really helpful during our experiments.

Since collaboration within the group and the working environment were crucial factors and I am very happy to have worked all the PhD students in my office, in our group, on the seventh floor, and in the whole institute! I have made many good friends during my time at the institute, and without your support and kindness the past four years would have been difficult. First of all, I would like to thank everyone in my office for being really good friends: Dr. Michaela Souliou, Dr. Rika Wrobel, Hun-Ho Kim, and of course Daniel Putzky.

I also appreciated the sometimes even weekly meetings of our small boardgames group—in particular the meetings of the *Evol-*

ution enthusiasts—that provided some counterweight in my work / life balance.

I also really enjoyed being a member of the exclusive club of PhD representatives. Good times, good BBQs :)

Doing sports with Luzia Germann, and all the members of the running or swimming group (well, we only were two, but hey!) kept me fit when I was at home, and I really appreciated the group spirit.

However, the past four year would have been impossible without the support of my family, especially during the ten years of my study of physics. I am thankful to my parents Yvonne and Peter, and am extremely proud of my little sister Anna. You were always on call when needed, and provided moral support at any time of day. And of course I'd like to thank Tatjana Meyer, the love of my life.

List of Publications

During Ph.D. program

[1]   A. Jain et al. 'Higgs mode and its decay in a 2D antiferromagnet'. In: *Nat. Phys.* 13 (27th Mar. 2017), pp. 633–637.
      DOI: 10.1038/nphys4077.

[2]   M. Etter et al. 'Crystal Structure Setermination of Non-stoichiometric $Ca_{4-x}RuO_{6-x}$ (x = 1.17) from X-ray Powder Diffraction Data'. In: *Powder Diffr.* 31 (Mar. 2016), pp. 59–62.
      DOI: 10.1017/S0885715615000883.

During B.Sc & M.Sc. program

[1]   M. Krautloher et al. 'Neutron Resonance Spin Echo with Longitudinal DC Fields'. In: *Rev. Sci. Instrum.* 87 (1st Dec. 2016), p. 125110.
      DOI: 10.1063/1.4972395.

[2]   J. Kindervater et al. 'Neutron Spin Echo Spectroscopy under 17 T Magnetic Field at RESEDA'. In: *EPJ Web of Conferences* 83 (2015), p. 03008.
      DOI: 10.1051/epjconf/20158303008.

[3]   A. Cattani-Scholz et al. 'A New Molecular Architecture for Molecular Electronics'. In: *Angew. Chem. Int. Ed. Engl.* special Insert from DFG 37 (2011), A11–A16.